UCLA
UCLA Electronic Theses and Dissertations

Title
Novel strategies to investigate and therapeutically modulate cancer metabolism

Permalink
https://escholarship.org/uc/item/4wc1v8s2

Author
Kim, Woosuk

Publication Date
2018

Peer reviewed|Thesis/dissertation

eScholarship.org Powered by the California Digital Library
University of California

UNIVERSITY OF CALIFORNIA

Los Angeles

Novel strategies to investigate and therapeutically modulate cancer metabolism

A dissertation submitted in partial satisfaction of the

requirements for the degree Doctor of Philosophy

in Molecular and Medical Pharmacology

by

Woosuk Kim

2018

© Copyright by

Woosuk Kim

2018

ABSTRACT OF THE DISSERTATION

Novel strategies to investigate and therapeutically modulate cancer metabolism

by

Woosuk Kim

Doctor of Philosophy in Molecular and Medical Pharmacology

University of California, Los Angeles, 2018

Professor Caius Gabriel Radu, Chair

In response to increased anabolic demands to support their survival and growth, cancer cells rewire cellular signaling and metabolic networks. While analysis of this rewiring can reveal vulnerabilities within cancers, it is becoming clear that more profound understandings of fundamental cancer biology are required for the successful therapeutic exploitation of cancer signaling and metabolism, two very complex and highly-regulated systems with multiple pathways contributing to their plasticity and robustness.

This thesis is the product of translational research efforts focused upon gaining a better understanding of fundamental aspects of cancer biology. The goals of the thesis are to 1) acquire novel insights of cancer biology to more precisely design therapeutic interventions to target cancers, more specifically pancreatic ductal adenocarcinoma (PDAC), one of most deadly cancers, and to 2) develop diagnostic tools that enable better characterization of metabolic characteristics of cancers.

Chapter 1 concerns the development of a clinically-applicable positron emission tomography (PET) probe for monitoring nucleotide metabolism at the whole-body level in a non-invasive

way. This study makes us think about biology across different scales, from molecular to whole-body levels.

In Chapter 2, the synthetic lethality screening tethered to chloroquine, an inhibitor of lysosome-dependent recycling pathways, which PDAC cells rely on to generate metabolic substrates is performed. The findings reveal that the inhibition of lysosomal recycling makes PDAC cells rely on replication stress response pathway for the survival due to impaired de novo nucleotide biosynthesis.

In chapter 3, I use multiple models of KRAS G12C mutant PDAC to profile the adaptive resistance mechanisms within cellular signaling and metabolic networks which arise from direct inhibition of mutant KRAS, the oncogenic driver of PDAC. This was followed by mapping the impacts of co-inhibition of oncogenic KRAS and the identified adaptive resistance mechanisms. Metabolomic analyses reveal metabolic vulnerabilities induced by co-inhibition of oncogenic KRAS and the adaptive resistance.

In the final chapter, I summarize ongoing projects and future directions that concern fundamental biology of PDAC metabolism.

The dissertation of Woosuk Kim is approved.

Harvey R. Herschman

Donald Barry Kohn

Michael Alan Teitell

Ting-Ting Wu

Caius Gabriel Radu, Committee Chair

University of California, Los Angeles

2018

DEDICATION

This dissertation is dedicated to my parents, Jongsoon Kim and Hyunhee Rhim, to my baby girl, Yina Kim, and to love of my life, Miyoun Song.

TABLE OF CONTENTS

LIST OF FIGURES

CHAPTER 1

CHAPTER 2

ACKNOWLEDGEMENTS

First and foremost, I would like to deeply thank my mentor, Dr. Caius G. Radu for his outstanding mentorship and continued support that he has given me for the past five years. Caius is a brilliant scientist and a very thoughtful and supportive mentor who will always do his best to help his students maximize their potential. Under his guidance, I would able to grow both as a person and a scientist and I will always be thankful for that.

I would also like to thank the members my thesis committee, Dr. Harvey R. Herschman, Dr. Donald B. Kohn, Dr. Michael A. Teitell and Dr. Ting-Ting Wu for their valuable insights, supports and the guidance that helped me greatly in conducting my dissertation research.

I thank Dr. Johannes Czernin and Dr. Timothy R. Donahue for creating a wonderful A-level team, which was a critical component of my dissertation research, and for their extremely helpful advice.

I would like to thank members of the A-level team. I thank Dr. Thuc M. Le, my post-doc mentor, for always trying to help me become a better scientist. I thank my fellow graduate students, Evan Abt, Soumya Poddar, Joe Capri for sharing this journey. I thank Anthony Cabebe and Wesley Armstrong for an amazing teamwork. I thank Dr. Shili Xu for his help and comments. I thank Ethan Rosser, Dr. Daniel Sun, Roy Pan, and Juno Van Valkenburgh for their help. I thank Larry Pang for his support in every aspect of our research for the past five years. I thank Joel Almajano for the research support. I thank Dr. Liu Wei for her help on animal experiments. I thank Nanping Wu and Luyi Li for their help on animal experiments and genetic models. In addition, I thank all current and former members of the A-level team for an amazing teamwork.

I would like to thank members of the Department of Molecular and Medical Pharmacology. I thank Dr. Michael E. Phelps for making and supporting this amazing department and creating an intellectually stimulating environment. I thank Emily Fitch for her help on international student matters.

I would like to thank all our collaborators. Especially, I thank Dr. Robert Damoiseaux for his help on high-throughput screenings and Elucidata for the help on analyzing big data.

I would like to acknowledge my funding, Genesis Fellowship from the Department of Molecular and Medical Pharmacology and Dissertation Year Fellowship from UCLA Graduate Division.

Chapter 1 is a version of a manuscript, [18F]CFA as a clinically translatable probe for PET imaging of deoxycytidine kinase activity, which was published in Proceedings of the National Academy of Sciences of the United States of America. 2016 Apr 12;113(15):4027-32.

Chapter 2 is a version of a manuscript, Lysosome inhibition sensitizes pancreatic cancer to replication stress by aspartate depletion, which is under revision in Proceedings of the National Academy of Sciences of the United States of America.

VITA

2011	Bachelor of Pharmacy, Pharmacy Chung-Ang University Seoul, Republic of Korea
2013	Master of Pharmacy, Pharmacology Chung-Ang University Seoul, Republic of Korea
2013-2018	Graduate Student Researcher Department of Molecular and Medical Pharmacology University of California, Los Angeles Los Angeles, CA, USA
2013-2016	Genesis Fellowship Awardee Department of Molecular and Medical Pharmacology University of California, Los Angeles Los Angeles, CA, USA
2017-2018	Dissertation Year Fellowship Awardee Graduate Division University of California, Los Angeles Los Angeles, CA, USA

Publications

1. Lückerath K, Stuparu AD, Wei L, **Kim W**, Radu CG, Mona CE, Calais J, Rettig M, Reiter RE, Czernin J, Slavik R, Herrmann K, Eiber M, Fendler WP. Detection Threshold and Reproducibility of 68Ga-PSMA11 PET/CT in a Mouse Model of Prostate Cancer. ***J Nucl Med***. 2018 Sep;59(9):1392-1397.

2. Kong SY, **Kim W**, Lee HR, Kim HJ. The histone demethylase KDM5A is required for the repression of astrocytogenesis and regulated by the translational machinery in neural progenitor cells. ***FASEB J***. 2018 Feb;32(2):1108-1119.

3. Le TM#, Poddar S#, Capri JR#, Abt ER, **Kim W**, Wei L, Uong NT, Cheng CM, Braas D, Nikanjam M, Rix P, Merkurjev D, Zaretsky J, Kornblum HI, Ribas A, Herschman HR, Whitelegge J, Faull KF, Donahue TR, Czernin J, Radu CG. ATR inhibition facilitates targeting of leukemia dependence on convergent nucleotide biosynthetic pathways. ***Nat Commun***. 2017 Aug 14;8(1):241. (# equal contribution)

4. Fendler WP, Stuparu AD, Evans-Axelsson S, Lückerath K, Wei L, **Kim W**, Poddar S, Said J, Radu CG, Eiber M, Czernin J, Slavik R, Herrmann K. Establishing 177Lu-PSMA-617 radioligand therapy in a syngeneic model of murine prostate cancer. ***J Nucl Med.*** 2017 May 25. pii: jnumed.117.193359.

5. Knezevic CE, Wright G, Remsing Rix LL, **Kim W**, Kuenzi BM, Luo Y, Watters JM, Koomen JM, Haura EB, Monteiro AN, Radu C, Lawrence HR, Rix U. Proteome-wide Profiling of

Clinical PARP Inhibitors Reveals Compound-Specific Secondary Targets. ***Cell Chem Biol***. 2016 Dec 22;23(12):1490-1503.

6. **Kim W**[#], Le TM[#], Wei L, Poddar S, Bazzy J, Wang X, Uong NT, Abt ER, Capri JR, Austin WR, Van Valkenburgh JS, Steele D, Gipson RM, Slavik R, Cabebe AE, Taechariyakul T, Yaghoubi SS, Lee JT, Sadeghi S, Lavie A, Faull KF, Witte ON, Donahue TR, Phelps ME, Herschman HR, Herrmann K, Czernin J, and Radu CG. [^{18}F]CFA as a clinically translatable probe for PET imaging of deoxycytidine kinase activity. ***Proc Nat Acad Sci USA***. 2016 Apr 12;113(15):4027-32. (# equal contribution)

7. Kim HJ, **Kim W**, Kong SY. Antidepressants for neuro-regeneration: from depression to Alzheimer's disease. ***Arch Pharm Res***. 2013 Nov;36(11):1279-90.

8. **Kim W**[#], Kim JH[#], Kong SY, Park MH, Sohn UD, Kim HJ. Comparison of ectopic gene expression methods in rat neural stem cells. ***Korean J Physiol Pharmacol***. 2013 Feb; 17(1):23-30. (# equal contribution)

Presentations

1. **Kim W** (Nov 17th, 2017) Coordination between pyrimidine nucleotide biosynthetic pathways. Annual retreat of the Dept. of Molecular and Medical Pharmacology at UCLA. Huntington Beach, CA, USA

2. **Kim W** (Oct 9th, 2017) Pyrimidine nucleotide metabolism in cancers. UCLA metabolism interest group monthly meeting. Los Angeles, CA, USA

3. **Kim W** (Apr 21nd, 2017) Identifying Cancer Nucleotide Metabolic Subtypes. Biweekly meeting of the Dept. of Molecular and Medical Pharmacology at UCLA, Los Angeles, CA, USA

4. **Kim W**, Le TM, Capri JR, Sun D, Abt ER, Poddar S, Morrow D, Li L, Czernin J, Donahue TR, and Radu CG (Nov 18th, 2016) Defining the roles of Pyrimidine recycling pathways in pancreatic cancer. Annual retreat of the Dept. of Molecular and Medical Pharmacology at UCLA. Huntington Beach, CA, USA

5. **Kim W** (Apr 15th, 2016) Thinking about biology across different scales: New PET assay for imaging deoxycytidine kinase activity in humans. Biweekly meeting of the Dept. of Molecular and Medical Pharmacology at UCLA, Los Angeles, CA, USA

6. **Kim W**, Le TM, Wei L, Poddar S, Bazzy J, Wang X, Uong NT, Abt ER, Capri JR, Austin WR, Van Valkenburgh JS, Steele D, Gipson RM, Slavik R, Cabebe AE, Taechariyakul T, Yaghoubi SS, Lee JT, Sadeghi S, Lavie A, Faull KF, Witte ON, Donahue TR, Phelps ME, Herschman HR, Herrmann K, Czernin J, and Radu CG (Oct 30th, 2015) [^{18}F]CFA as a clinically translatable probe for PET imaging of deoxycytidine kinase activity. Annual retreat of Dept. of Molecular and Medical Pharmacology at UCLA. Huntington Beach, CA, USA (Oct 30th) *and* annual retreat of UCLA-Caltech Engineering Immunity (EI) group. Lake Arrowhead, CA, USA (Oct 31st) ***(won best poster award)***

7. **Kim W**, Czernin J, and Radu CG (Nov 22nd, 2014) Exploiting replication stress overload to induce synthetic lethality in hepatocellular carcinoma. Annual retreat of the Dept. of Molecular and Medical Pharmacology at UCLA. Huntington Beach, CA, USA

CHAPTER 1

Development of [^{18}F]CFA as a clinically translatable probe for PET imaging of deoxycytidine kinase activity

ABSTRACT

Deoxycytidine kinase (dCK), a rate-limiting enzyme in the cytosolic deoxyribonucleoside (dN) salvage pathway, is an important therapeutic and Positron Emission Tomography (PET) imaging target in cancer. PET probes for dCK have been developed and are effective in mice, but have suboptimal specificity and sensitivity in humans. To identify a more suitable probe for clinical dCK PET imaging, we compared the selectivity of two candidate compounds, [^{18}F]CFA ([^{18}F]Clofarabine; 2-chloro-2'-deoxy-2'-[^{18}F]fluoro-9-β-D-arabinofuranosyl-adenine) and [^{18}F]F-AraG (2′-deoxy-2′-[^{18}F]fluoro-9-β-D-arabinofuranosyl-guanine), for dCK and deoxyguanosine kinase (dGK), a dCK-related mitochondrial enzyme. We demonstrate that, in the tracer concentration range used for PET imaging, [^{18}F]CFA is primarily a substrate for dCK with minimal cross-reactivity. In contrast, [^{18}F]F-AraG is a better substrate for dGK than for dCK. [^{18}F]CFA accumulation in leukemia cells correlated with dCK expression and was abrogated by treatment with a dCK inhibitor. Although [^{18}F]CFA uptake was reduced by deoxycytidine (dC) competition, this inhibition required high dC concentrations present in murine, but not human, plasma. Expression of cytidine deaminase, a dC catabolizing enzyme, in leukemia cells both in cell culture and in mice reduced the competition between dC and [^{18}F]CFA, leading to increased dCK-dependent probe accumulation. First-in-human [^{18}F]CFA PET/CT studies showed probe accumulation in tissues with high dCK expression; e.g. hematopoietic bone marrow and secondary lymphoid organs. The selectivity of [^{18}F]CFA for dCK and its favorable biodistribution in humans justify further studies to validate [^{18}F]CFA PET as a new cancer biomarker for treatment stratification and monitoring.

INTRODUCTION

Accurate DNA replication and repair require sufficient and balanced production of deoxyribonucleoside triphosphates (dNTPs) (1). Mammalian cells synthesize dNTPs by two biochemical routes: the *de novo* pathway produces dNTPs from glucose and amino acid precursors, while the nucleoside salvage pathway generates dNTPs from deoxyribonucleosides (dNs) scavenged from the extracellular milieu by the combined action of nucleoside transporters and dN kinases (**Fig. 1.1A**). The cytosolic dN kinases in mammalian cells are thymidine kinase 1 (TK1), which phosphorylates thymidine (dT) and deoxyuridine (dU), and deoxycytidine kinase (dCK), which phosphorylates deoxycytidine (dC), deoxyadenosine (dA), and deoxyguanosine (dG) (2). Although dCK has been studied extensively *in vitro*, its *in vivo* functions are not well understood. Previously, we reported impaired hematopoiesis in *dCK*$^{-/-}$ mice resulting from DNA replication stress in hematopoietic progenitors due to insufficient dCTP supply (3, 4). More recently, we showed that, in cancer cells, dCK confers resistance to inhibitors of *de novo* dCTP biosynthesis and that pharmacological co-targeting of dCK and ribonucleotide reductase, the rate-limiting enzyme in the *de novo* pathway, was well-tolerated and efficacious in animal models of acute leukemia (5, 6). dCK also plays an essential role in the activation of the nucleoside analog pro-drugs Cytarabine, Fludarabine, Gemcitabine, Decitabine, Cladribine, and Clofarabine (7) (**Fig. 1.1B**). Clinically applicable assays to measure tumor dCK activity *in vivo* would be of great value, given the variable response rates and toxicities associated with these frequently used pro-drugs (7). Collectively, the identification of dCK as a new therapeutic target in acute leukemia, the requirement for dCK in the activation of FDA-approved nucleoside analog pro-drugs, and the heterogeneous expression of dCK in cancer suggest that dCK is an important target for non-invasive biomarker PET imaging.

The first PET probe described for dCK imaging was 1-(2'-deoxy-2'-[^{18}F]fluoro-β-D-arabinofuranosyl)cytosine ([^{18}F]FAC) (8). While [^{18}F]FAC enabled PET imaging of dCK activity in mice (8-11), a subsequent study (12) questioned its clinical utility because of rapid probe

catabolism mediated by cytidine deaminase (CDA), an enzyme present at higher levels in humans than in rodents (13). CDA converts [^{18}F]FAC to [^{18}F]FAU (1-(2'-deoxy-2'-[^{18}F]fluoro-β-D-arabinofuranosyl)uracil), a metabolite that is not phosphorylated by dCK. To overcome this problem, L-enantiomer analogs of [^{18}F]FAC that resisted deamination and retained affinity for dCK were developed (14). Two of the L-enantiomer analogs, L-[^{18}F]FAC (1-(2'-deoxy-2'-[^{18}F]fluoro-β-L-arabinofuranosyl)cytosine) and L-[^{18}F]FMAC (2′-deoxy-2′-[^{18}F]fluoro-5-methyl-β-L-arabinofuranosylcytosine) were translated to the clinic (12, 15). These second generation dCK probes had better sensitivity than [^{18}F]FAC in humans as reflected by improved accumulation in the bone marrow, a tissue with high dCK activity. However, both L-FAC analogs were cross-reactive with mitochondrial thymidine kinase 2 (TK2), which, like dCK, lacks enantioselectivity and consequently phosphorylates deoxypyrimidines with both D and L-enantiomeric configurations (16). In humans, cross-reactivity with TK2 was likely responsible for the uptake of the FAC analogs into the myocardium (12), a tissue with high TK2 expression (17).

Because dCK phosphorylates both pyrimidines and purines (18), the limitations of current PET probes for dCK could be circumvented using fluorinated purine analogs. Two candidate purine PET probes for dCK have been proposed (**Fig. 1.2A**): [^{18}F]CFA ([^{18}F]Clofarabine, 2-chloro-2'-deoxy-2'-[^{18}F]fluoro-9-β-D-arabinofuranosyl-adenine) (14) and [^{18}F]F-AraG (2′-deoxy-2′-[^{18}F]fluoro-9-β-D-arabinofuranosyl-guanine) (19). Unlike FAC and its analogs, neither of these purine analogues is phosphorylated by TK2. However, both [^{18}F]CFA and [^{18}F]F-AraG may be substrates for the mitochondrial deoxyguanosine kinase (dGK, **Fig. 1.2A**) which is structurally related to both dCK and TK2 (20). Despite some overlap in substrate specificity, dCK and dGK have distinct biological functions (18, 21, 22) and expression patterns (22, 23). Therefore, to properly interpret the information provided by [^{18}F]CFA and [^{18}F]F-AraG PET scans, it is essential to delineate the roles played by dCK and dGK in the intracellular trapping of these two candidate PET probes. Here we compared the selectivity of [^{18}F]CFA and [^{18}F]F-AraG for dCK and dGK. Observed differences in kinase selectivity indicated that PET assays using these

probes are likely have distinct applications, with [^{18}F]CFA as the choice for clinical dCK imaging and [^{18}F]F-AraG as the appropriate probe for dGK imaging. We then investigated whether competition between [^{18}F]CFA and endogenous dC affected the sensitivity of [^{18}F]CFA PET imaging in the range of plasma dC concentrations found in mice, humans and other species. We also present preliminary first-in-human studies of [^{18}F]CFA biodistribution and discuss how this new tracer complements the current repertoire of PET probes for nucleotide metabolism.

MATERIALS AND METHODS

Animal Studies

These were conducted under the approval of UCLA Animal Research Committee and were performed in accordance with the guidelines from the Division of Laboratory Animal Medicine at UCLA. For tumor xenograft experiments, 2×10^6 CEM-EYFP and CEM-CDA were resuspended in 100 μL of a 50/50 (v/v) mixture of PBS and matrigel (BD Biosciences) for s.c. injections in the left and right shoulders of NSG mice.

MicroPET/CT and PET/CT Studies

MicroPET/CT experiments were conducted as previously described (14). Briefly, pre-warmed and anesthetized NSG mice were injected with indicated probes and PET and CT images were acquired using the G8 PET/CT scanner (Sofie Biosciences) 3 h after the injection of 740 kBq [^{18}F]CFA. Clinical PET/CT studies were performed under a Radioactive Drug Research Committee protocol as previously described (12). Briefly, 233.1 MBq [^{18}F]CFA was injected in the clinical subjects. For the healthy volunteer, dynamic imaging was performed immediately after the probe injection. For the paraganglioma patient, static imaging was performed 35 min after the probe injection.

Plasmids and Retrovirus Production

The pMSCV-hCDA-IRES-EYFP plasmid was described previously (35). The pMSCV-hdGK-IRES-EYFP plasmid was generated by the insertion of the human dGK coding sequence with the N-terminal mitochondrial localization sequence deleted (amino acids 1-50), into the multiple cloning site of the MSCV-IRES-EYFP plasmid as previously described (47). The pMSCV-hdCK-IRES-EYFP plasmid was generated as previously described (9). Amphotropic retroviruses were generated by transient co-transfection of the MSCV retroviral plasmid and pCL-10A1 packaging plasmid into Phoenix-Ampho packaging cells.

Cell Lines and Culture Conditions

CCRF-CEM cells were obtained from the American Type Culture Collection. CEM-R cells were a gift from Dr. Margaret Black (Washington State University). CEM and CEM-R cells were grown in RPMI-1640 medium (Corning) supplemented with 10% fetal bovine serum (FBS, Omega Scientific) and 2 mM L-glutamine (Life Technologies). For radioactive probe uptake assays, RPMI-1640 medium supplemented with 10% dialyzed FBS (Life Technologies) was used to minimize artifacts caused by deoxyribonucleosides present in regular FBS. To generate CEM-R-ΔdGK, CEM-R-dCK and CEM-CDA lines, parental cells underwent spinfection with the respective amphotropic retroviruses and were then sorted by flow cytometry to isolate pure populations of transduced cells.

Immunoblotting

This was performed as previously described (4) using the following primary antibodies: anti-dCK (described in reference (39)), anti-dGK (Sigma-Aldrich, HPA034766), anti-Actin (Sigma-Aldrich) and anti-CDA (Sigma-Aldrich, SAB1300716) with the following secondary antibodies: anti-rabbit IgG, HRP-linked (Cell Signaling Technology, 7074), and anti-mouse IgG, HRP-linked (Cell Signaling Technology, 7076). Chemiluminescent substrates (ThermoFisher Scientific, 34077 and 34095) and autoradiography film (Denville) were used for detection.

Radioactive Probe Uptake Assays

These were conducted as previously described (47). Briefly, 5 x 10^5 CEM and CEM-R isogenic cells were resuspended in 1 mL of media/well in 12-well plates. After 1 h, cells were incubated with the indicated amounts of radioactive probes for an additional hour. Cells were then harvested and washed twice with ice-cold PBS. Radioactivity was measured using a beta-counter (Perkin Elmer) for [^{3}H]-labeled probes, and a gamma-counter (Packard) for [^{18}F]-labeled probes. All [^{3}H]-labeled probes used were purchased from Moravek Biochemicals.

Radiochemical Synthesis of [^{18}F]-labeled Probes

The syntheses of [^{18}F]CFA, [^{18}F]F-AraG, and [^{18}F]FDG were performed as previously described (14, 19, 53).

LC-MS/MS-MRM

Stock solutions (10 mM) of ^{13}C,^{15}N- ($^{13}C_{10}$,$^{15}N_5$-dA; $^{13}C_{10}$,$^{15}N_5$-dG; $^{13}C_9$,$^{15}N_3$-dC and $^{13}C_{10}$,$^{15}N_2$-dT, Cambridge Isotope Laboratories) and ^{15}N-labeled ($^{15}N_5$-dA, $^{15}N_5$-dG, $^{15}N_3$-dC and $^{15}N_2$-dT, Cambridge Isotope Laboratories) dNs were prepared individually in dimethyl sulfoxide (DMSO), and stored at -20ºC. Aliquots of the stock solutions of the ^{13}C,^{15}N- and ^{15}N-labeled dNs were separately pooled and diluted in methanol. Human plasma samples were obtained from Sigma-Aldrich and from healthy donors. Non-human primate (NHP) plasma samples were gifts from Dr. Andrew Pierce (AstraZeneca). Whole blood samples from rodents were obtained by retro-orbital sinus bleed using hematocrit capillary tubes and were immediately centrifuged (2,000 *g*, 15 min,) to isolate the plasma supernatant. To 20 µL of culture medium or plasma, a solution of ^{15}N-labeled internal standards (IS) was added (60 µL, 20 nM of ^{15}N-labeled dNs in methanol/DMSO, 100/0.0002, v/v). The mixture was vigorously mixed (30 s) and centrifuged (15,000 *g*, 10 min, 4ºC), then 60 µL of the supernatants was transferred into clean vials for LC-MS/MS-MRM analysis. With each batch of biological samples a series of calibration standards were prepared by diluting the 10 mM solutions of ^{13}C,^{15}N-labeled dNs in either media or plasma from pooled untreated mice to give concentrations in the 10 nM - 10 µM range. To 20 µL of each of these samples the same amount of IS was added. The calibration standards were processed simultaneously with and identically to the biological samples. Twenty µL of each sample, equivalent to 5 µL plasma or media, was injected onto a porous graphitic carbon column (Hypercarb, Thermo-Scientific, 2.1 × 100 mm, 5 µm) equilibrated in water/acetonitrile/formic acid, 95/5/0.2, and eluted (200 µL/min) with an increasing concentration of solvent B (acetonitrile/water/formic acid, 90/10/0.2, vol/vol/vol: % B/min/µL per min; 0/0/200, 0/5/200, 15/10/200, 15/20/200, 40/21/200, 50/25/200, 100/26/700, 100/30/700, 0/31/700, 0/34/700,

0/35/200). The effluent from the column was directed to an electrospray ion source (Agilent Jet Stream) connected to a triple quadrupole mass spectrometer (Agilent 6460) operating in the positive ion MRM mode. The intensity of ion transitions for the various isotopomers were recorded using previously optimized conditions (parent m/z (MH^+)fragment m/z were: dA, 252.1136.1; $^{15}N_5$-dA, 257.1141.1; $^{13}C_{10}$,$^{15}N_5$-dA, 267.1146.1; dG, 268.1152.1; $^{15}N_5$-dG, 273.1157.1; $^{13}C_{10}$,$^{15}N_5$-dG, 283.1162.1; dC, 228.1112.1; $^{15}N_3$-dC, 231.1115.1; $^{13}C_9$,$^{15}N_3$-dC, 240.1119.1; dT,243.1127.1; $^{15}N_2$-dT, 245.1129.1; and $^{13}C_{10}$,$^{15}N_2$-dT, 255.1134.1). Peak areas at the corresponding retention times were recorded using instrument manufacturer-supplied software. Data from the calibration standards were used to construct calibration curves for each dN (ordinate, peak area $^{13}C_{10}$,$^{15}N_5$ dN/peak area of the corresponding IS; abscissa, molarity of $^{13}C_{10}$,$^{15}N_5$ dN). The molarity of each unlabeled dN in each sample was calculated, after normalization to the corresponding internal standard, by interpolation from the corresponding calibration curve.

Statistical Analyses

Data are presented as means ± SD. Statistical significance is determined by two-tailed t-test. P values below 0.05 were considered significant.

RESULTS

Differential selectivity of [^{18}F]CFA and [^{18}F]F-AraG for dCK and dGK

To determine the selectivity of [^{18}F]CFA and [^{18}F]F-AraG for dCK and dGK, CEM-R leukemia cells, which do not express dCK (24) but contain endogenous dGK (**Fig. 1.2B**), were re-constituted with human dCK (CEM-R-dCK, **Fig. 1.2B**). To enable an additional comparison between [^{18}F]CFA and [^{18}F]F-AraG in the absence of any confounding aspects related to potential differences in the access of these two probes to mitochondrial-located dGK, we also generated CEM-R cells that express a truncated form of human dGK (CEM-R-ΔdGK) which lacks the N-terminal mitochondrial sorting signal (**Fig. 1.2B**). CEM-R cells expressing enhanced yellow fluorescent protein (CEM-R-EYFP) completed the isogenic panel (**Fig. 1.2B**). Radioactive uptake assays using tracer amounts (10-100 nM) of [^{3}H]-labeled endogenous substrates, deoxycytidine ([^{3}H]dC) and deoxyguanosine ([^{3}H]dG), were used to validate the isogenic lines. [^{3}H]dC accumulation was 237 ± 17 fold higher in CEM-R-dCK cells compared to CEM-R-EYFP and CEM-R-ΔdGK cells (**Fig. 1.2C**). DI-82, a specific dCK inhibitor (25), abrogated [^{3}H]dC accumulation in CEM-R-dCK cells (**Fig. 1.2C**). CEM-R-ΔdGK cells retained 6.62 ± 0.49 fold more [^{3}H]dG compared to CEM-R-EYFP cells (**Fig. 1.2D**), thereby confirming the functionality of the truncated dGK construct. [^{3}H]dG also accumulated in CEM-R-dCK cells (2.01 ± 0.19 fold increase relative to CEM-R-EYFP cells, **Fig. 1.2D**), consistent with the ability of dCK to phosphorylate both pyrimidine and purine substrates (2, 18). The isogenic CEM-R panel was then used to compare the accumulation of tracer amounts (50-100 pM) of [^{18}F]CFA and [^{18}F]F-AraG. [^{18}F]CFA accumulation in CEM-R-EYFP cells was indistinguishable from background levels (**Fig. 1.2E**). While ΔdGK overexpression resulted in a minor increase (2.97 ± 0.09 fold) in [^{18}F]CFA accumulation, a much larger (79 ± 2 fold) increase in probe uptake was observed in the CEM-R-dCK cells (**Fig. 1.2E**). DI-82 abrogated [^{18}F]CFA accumulation in CEM-R-dCK cells (**Fig. 1.2E**), thereby confirming the specificity of this probe for dCK. Overall, [^{18}F]CFA accumulation in the isogenic CEM-R panel closely resembled that of [^{3}H]dC (**Fig. 1.2C**). In contrast, [^{18}F]F-AraG accumulation (**Fig. 1.2F**) closely resembled that of [^{3}H]dG (**Fig.**

1.2D). In summary, in the subnanomolar concentration range relevant for PET imaging, [^{18}F]CFA is primarily a substrate for dCK with minimal cross-reactivity for dGK, while [^{18}F]F-AraG is primarily a substrate for dGK with dCK playing a lesser role. [^{18}F]CFA accumulation was sensitive to variations in dCK expression (**Fig. 1.2G,H**), further supporting the utility of this probe for imaging dCK activity.

[^{18}F]CFA accumulation is inhibited by deoxycytidine (dC) at concentrations present in murine and rat plasma, but not in human or non-human primate (NHP) plasma

Competition between probes and endogenous metabolites often reduces the sensitivity of PET assays; e.g., [^{18}F]FDG (2-deoxy-2-[^{18}F]fluoro-D-glucose) competes with endogenous glucose (26) and [^{18}F]FLT (3'-[^{18}F]fluoro-3'-deoxythymidine) competes with endogenous thymidine (dT) (27, 28). As shown in **Fig. 1.3A**, [^{3}H]CFA accumulation is also inhibited in a dose dependent manner by dC, the physiological substrate of dCK, with an IC_{50} value of 181 ± 56 nM (**Fig. 1.3A**). Deoxyadenosine (dA) and deoxyguanosine (dG), which are also dCK substrates (18), also inhibited [^{3}H]CFA accumulation (**Fig. 1.4**). The high IC_{50} values observed for dA and dG (75 μM and 33 μM, respectively, **Fig. 1.4**) likely reflect the rapid catabolism of these purine dNs by adenosine deaminase (ADA) and purine nucleoside phosphorylase (PNP); both are expressed at high levels in lymphoid cells (29, 30).

To determine whether the competition between CFA and dC observed in cell culture could also occur *in vivo*, plasma dC levels in humans, non-human primates (NHPs), mice and rats were measured by combined liquid chromatography tandem mass spectrometry in the multiple reaction-monitoring mode (LC-MS/MS-MRM) (**Fig. 1.3B**). C57BL/6 mice and rats plasma dC concentrations are in the high nanomolar to low micromolar range, which, according to our cell culture data, are sufficient to inhibit CFA uptake. In marked contrast, plasma dC concentrations are 2-3 orders of magnitude lower in humans and NHPs than in mice and rats, and are well-below the levels that can inhibit CFA uptake. A similar pattern was observed for dT in our study

(**Fig. 1.3C**), in agreement with previous reports (31, 32). In contrast to dC and dT, plasma concentrations of dA and dG did not differ significantly in the examined species (**Fig. 1.3D,E**). Mouse plasma dN levels were not affected by 24 h fasting (**Fig. 1.3F**), arguing against an exogenous origin for these nucleosides. Instead, the observed differences are likely the result of different catabolic rates of endogenously produced dC and dT in rodents *vs.* primates. To test this hypothesis, stable isotope labeled dC ([U-$^{13}C_9$,$^{15}N_3$]dC) was incubated for 1 h in human and mouse plasma samples with or without tetrahydrouridine (THU), a specific cytidine deaminase (CDA) inhibitor (33). CDA catalyzes the first step in dC catabolism by converting dC to deoxyuridine (dU). LC-MS/MS-MRM analyses of labeled dC and dU demonstrated that dC was catabolized more rapidly in human than in murine plasma (**Fig. 1.3G**, *top and bottom panels*). Moreover, the CDA inhibitor THU blocked dC deamination in human plasma (*middle panels*).

To further investigate how CDA expression influences CFA accumulation, CEM cells engineered to express CDA (CEM-CDA) or EYFP (CEM-EYFP, negative control) (**Fig. 1.5A**) were incubated with cell culture medium containing 5 μM [U-$^{13}C_9$,$^{15}N_3$]dC. The medium was sampled at the times shown to measure the CDA-mediated catabolism of labeled dC. A ~32 fold decrease in the amount of [U-$^{13}C_9$,$^{15}N_3$]dC was observed after a 6 h incubation with CEM-CDA cells, but not with the CDA negative cells (**Fig. 1.5B**). Consequently, [^{3}H]CFA added for 1 h after the 6 h incubation period was retained only in the CEM-CDA cells. [^{3}H]CFA accumulation by the CEM-CDA cells was dCK-dependent, as indicated by the effect of the dCK inhibitor DI-82 (**Fig. 1.5C**). To model these cell culture findings *in vivo*, NOD SCID IL-2 receptor gamma chain KO (NSG) mice underwent subcutaneous bilateral implantation with either CEM-EYFP or CEM-CDA cells in both flanks. Mice bearing bilateral tumors were imaged serially by PET/CT, using either [^{18}F]CFA or [^{18}F]FDG, at the indicated times (**Fig. 1.6A**). Plasma dC concentrations decreased with time in mice with CEM-CDA tumors but not in mice with CEM-EYFP tumors (**Fig. 1.6B**), likely reflecting the leakage of tumor CDA in plasma. Consistent with the cell culture data (**Fig. 1.5C**), mice bearing CEM-CDA tumors, which had reduced plasma dC levels, accumulated

significantly more [^{18}F]CFA than mice bearing CEM-EYFP tumors, as indicated by day 17 PET scans (**Fig. 1.6C,D**). [^{18}F]FDG PET scans performed on day 18 revealed similar metabolic activity in both CDA and EYFP tumors (**Fig. 1.6C,E**). On day 19, mice were treated with DI-82 followed by a second [^{18}F]CFA PET scan which confirmed that tumor probe accumulation was dCK dependent (**Fig. 1.6C,D**). Collectively, these data indicate that (*i*) competition with endogenous dC reduces the sensitivity of [^{18}F]CFA PET imaging in species with high levels of plasma dC concentration such as mice and rats, (*ii*) CDA activity is an important determinant of [^{18}F]CFA accumulation in tumors, by reducing the levels of competing endogenous dC, and (*iii*) tumor [^{18}F]CFA accumulation *in vivo* requires dCK activity.

First-in-human [^{18}F]CFA biodistribution studies

Since dC competes with CFA for cellular uptake (**Fig. 1.3A**) and because plasma dC levels are 2-3 orders of magnitude lower in humans than in mice (**Fig. 1.3B**), we hypothesized that the biodistribution of [^{18}F]CFA will be more favorable in humans than in mice. Indeed, unlike the negative scans in mice (14), [^{18}F]CFA PET/CT scans in healthy volunteers revealed significant probe accumulation in dCK positive tissues (bone marrow, liver and spleen, **Fig. 1.7A**). [^{18}F]CFA also accumulated in the axillary lymph nodes (*arrows*) of healthy volunteers (*left*: coronal, *right*: transverse image, **Fig. 1.7A**). Label accumulation in the kidneys and bladder was indicative of urinary clearance. [^{18}F]CFA and [^{18}F]FDG PET/CT scans of a paraganglioma patient showed label accumulation in a skull bone tumor lesion but not in a lumbar vertebra bone lesion (**Fig. 1.7B**), reflecting inter-lesion heterogeneity in [^{18}F]CFA uptake. We were initially surprised that the [^{18}F]CFA accumulation observed throughout the spinal column in healthy volunteers (**Fig. 1.7A**) was not detected in the paraganglioma patient in whom the lumbar segment of the spinal column was negative for [^{18}F]CFA accumulation (**Fig. 1.7C**). A subsequent examination of the clinical history of this patient revealed that the [^{18}F]CFA negative lumbar spine region corresponds anatomically to the part of the vertebral column that was previously (9 months prior to the scan) irradiated to target a tumor lesion at this location. This serendipitous finding

suggested that [^{18}F]CFA bone accumulation in humans likely reflects dCK-dependent probe uptake by bone marrow cells, rather than probe defluorination. Further supporting this interpretation, CFA defluorination was not detected in metabolic stability studies of CFA administered at pharmacological doses in humans (34).

DISCUSSION

We show that [^{18}F]CFA is a highly specific substrate/probe for dCK with minimal cross-reactivity with dGK. [^{18}F]CFA accumulation in leukemia cells was competitively inhibited in a concentration-dependent manner by dC, the physiological dCK substrate. Evidence is provided that plasma dC levels vary significantly across species and that these variations correspond to striking differences in [^{18}F]CFA biodistribution between mice and humans. Accordingly, the [^{18}F]CFA PET assay is more sensitive in humans than in mice, due to reduced competition between the probe and endogenous dC. [^{18}F]CFA accumulation in leukemia cells was dCK-dependent and probe accumulation was sensitive to variations in dCK expression. In this context, a large variation in dCK expression and activity was observed in a panel of lymphoma cell lines (35). Similar variations in dCK expression likely occur in other cancers. dCK mRNA levels also increase upon T cell activation (8). Additional levels of dCK regulation involve post-translational mechanisms. For example, phosphorylation of dCK at Ser-74 increases dCK activity (36). The DNA-damage response kinase Ataxia-telangiectasia mutated (ATM) has been proposed to catalyze this dCK phosphorylation (37-39). If the observed sensitivity of [^{18}F]CFA PET to variations in dCK activity is confirmed by larger clinical studies, this new non-invasive, real time PET assay may provide a useful biomarker for various therapies that trigger T cell activation, induce DNA damage (39), or rely on dCK-dependent nucleoside analog pro-drugs. In particular, [^{18}F]CFA may be useful as a pharmacokinetic PET stratification biomarker for its corresponding drug Clofarabine (Clolar®, Genzyme) (40). Furthermore, as dCK inhibitors (5, 6, 25) advance towards clinical trials, [^{18}F]CFA PET could provide a companion pharmacodynamic biomarker to help optimize dosing and scheduling regimes.

Given the susceptibility of [^{18}F]CFA uptake to competition by endogenous nucleosides, the use of [^{18}F]CFA in patients with elevated plasma dN levels may result in false negative scans. Such conditions include the tumor lysis syndrome that follows chemotherapy in hematological malignancies (41), genetic defects in the purine nucleoside catabolizing enzymes adenosine

deaminase (ADA) and purine nucleoside phosphorylase (PNP) (42, 43), and treatment of certain leukemias with ADA and PNP inhibitors (44, 45). In addition to plasma dN levels, which should be determined in each patient scanned with [^{18}F]CFA, the interpretation of [^{18}F]CFA PET scans should also take into account factors other than dCK that could modulate probe accumulation. Both concentrative and equilibrative nucleoside transporters, as well as ATP-binding cassette (ABC) transporters, could all modulate [^{18}F]CFA accumulation in tumors (36, 46).

In summary, this work supports the evaluation of [^{18}F]CFA in larger clinical studies as a companion biomarker for multiple therapeutic approaches. Moreover, [^{18}F]CFA complements the toolbox of nucleoside analog PET probes for imaging dN kinases (**Fig. 1.8**). Given the diverse biological functions and the therapeutic relevance of cytosolic and mitochondrial dN kinases, the availability of a toolbox of PET imaging probes to non-invasively measure the activity of these enzymes could enable a wide range of preclinical and clinical applications.

FIGURES

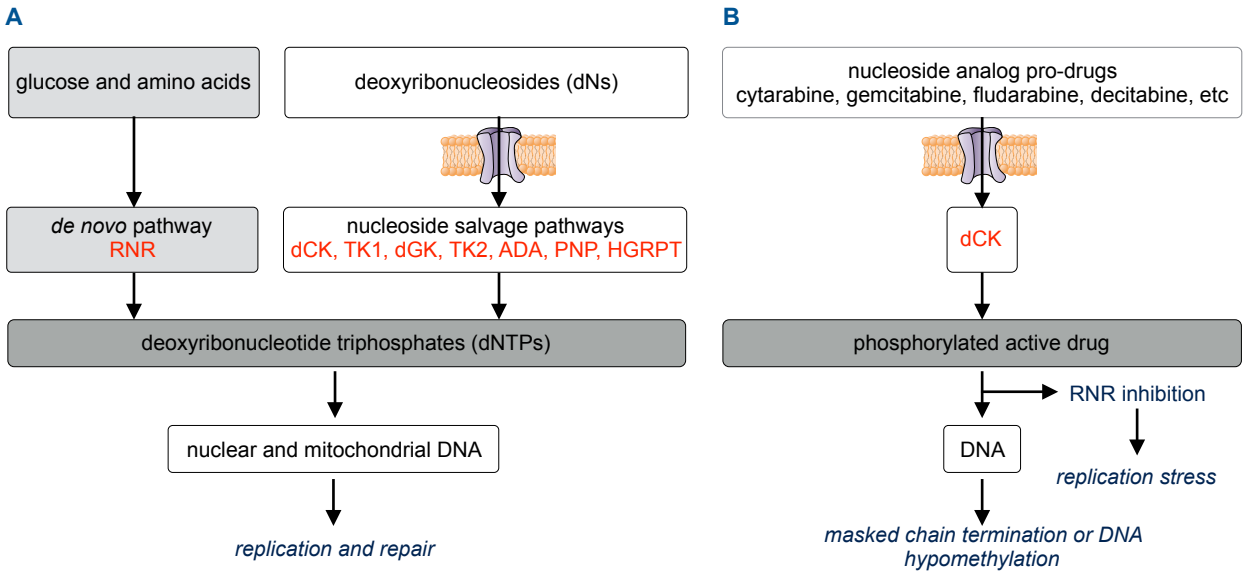

Fig. 1.1. Schematic overview of de novo and salvage dNTP biosynthetic pathways and the mechanism of action of dCK-dependent nucleoside analog prodrugs. (**A**) dNTPs are synthesized by the de novo pathway starting from glucose and amino acids, and by nucleoside salvage pathways starting with preformed deoxyribonucleosides (dNs). ADA, adenosine deaminase; dCK, deoxycytidine kinase; dGK, deoxyguanosine kinase; HGPRT, hypoxanthine-guanine phosphoribosyltransferase; PNP, purine nucleoside phosphorylase; RNR, ribonucleotide reductase; TK1, thymidine kinase 1; TK2, thymidine kinase 2. (**B**) Indicated nucleoside analog prodrugs are phosphorylated by dCK to their monophosphate forms and trapped inside the cells by dCK. Subsequent phosphorylation steps generate the active di- and triphosphate forms that induce anti-tumor effects via the indicated mechanisms.

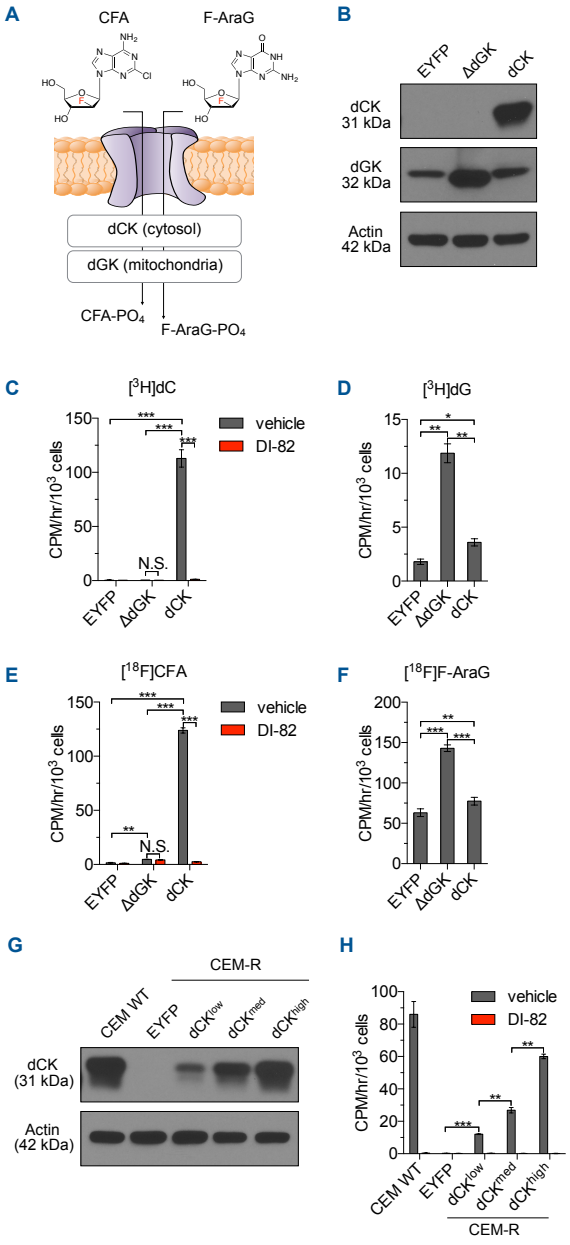
A
CFA
F-AraG
dCK (cytosol)
dGK (mitochondria)
CFA-PO4
F-AraG-PO4
B
EYFP
ΔdGK
dCK
dCK
31 kDa
dGK
32 kDa
Actin
42 kDa
C
[3H]dC
vehicle
DI-82
CPM/hr/10^3 cells
N.S.
EYFP
ΔdGK
dCK
D
[3H]dG
E
[18F]CFA
F
[18F]F-AraG
G
CEM-R
CEM WT
EYFP
dCKlow
dCKmed
dCKhigh
dCK
(31 kDa)
Actin
(42 kDa)
H
vehicle
DI-82
CPM/hr/10^3 cells
CEM WT
EYFP
dCKlow
dCKmed
dCKhigh
CEM-R

Fig. 1.2. [^{18}F]CFA accumulation is primarily dCK-dependent whereas [^{18}F]F-AraG uptake primarily reflects dGK activity. (**A**) Potential mechanisms for accumulation of CFA and F-AraG in cells. (**B**) Western blot analysis of dCK and dGK expression in dCK-deficient CEM-R cells engineered to express EYFP (negative control), or dCK, or truncated human dGK (ΔdGK) lacking the mitochondrial sorting N-terminal sequence. (**C**) [^{3}H]dC (18.5 kBq), (**D**) [^{3}H]dG (18.5 kBq), (**E**) [^{18}F]CFA (18.5 kBq), and (**F**) [^{18}F]F-AraG (18.5 kBq) uptake assays using the isogenic panel of cells shown in B. [^{3}H]dC and [^{18}F]CFA uptake assays were performed in the presence or absence of DI-82 (1 μM), a small molecule inhibitor of dCK (**C and E**). N.S., nonsignificant; *P < 0.05; **P < 0.01; ***P < 0.001. (**G**) Western blot analysis of dCK expression in CEM WT cells and in CEM-R cells engineered to express EYFP or low, medium, and high dCK levels. (**H**) [^{3}H]CFA (18.5 kBq) uptake, ± DI-82 (1 μM), in the isogenic panel of CEM-R cell lines shown in A. **P < 0.01; ***P < 0.001. All results are representative of three independent experiments (n = 3 for each experiment).

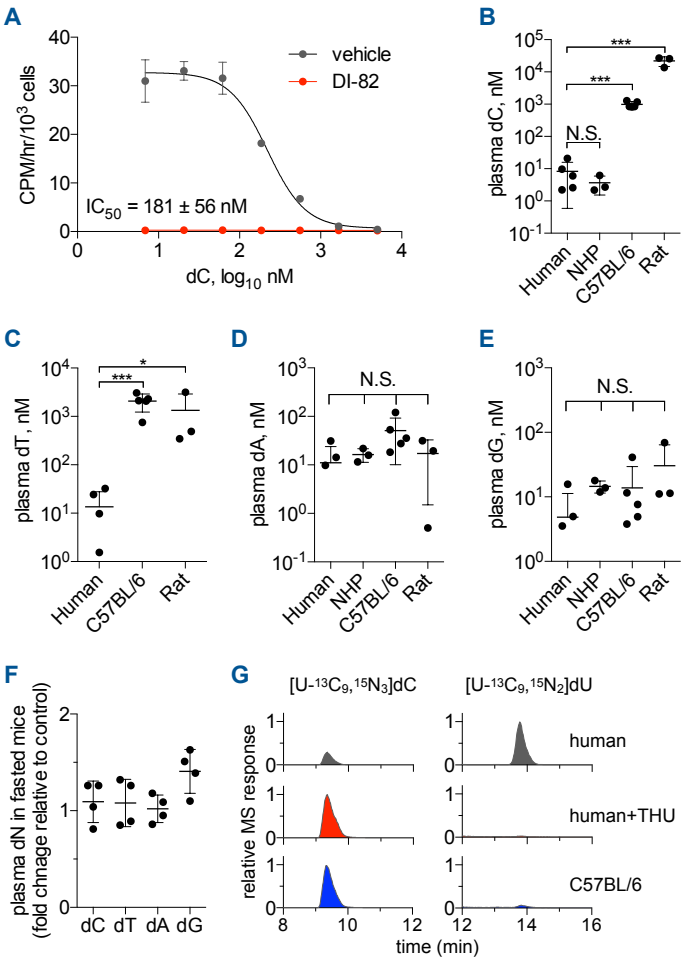
A
CPM/hr/10^3 cells
vehicle
DI-82
IC50 = 181 ± 56 nM
dC, log10 nM
B
plasma dC, nM
***
***
N.S.
Human
NHP
C57BL/6
Rat
C
plasma dT, nM
*
***
Human
C57BL/6
Rat
D
plasma dA, nM
N.S.
Human
NHP
C57BL/6
Rat
E
plasma dG, nM
N.S.
Human
NHP
C57BL/6
Rat
F
plasma dN in fasted mice
(fold chnage relative to control)
dC dT dA dG
G
[U-13C9,15N3]dC
[U-13C9,15N2]dU
relative MS response
human
human+THU
C57BL/6
time (min)

Fig. 1.3. The endogenous dCK substrate dC competes with [^{3}H]CFA uptake at concentrations found in rodent plasma but not in human or NHP plasma. (**A**) Extracellular dC competes with CFA uptake. [^{3}H]CFA (9.25 kBq) uptake for 1 h in CEM WT cells in the presence of varying concentrations of dC ± DI-82 (1 μM). n = 3 per group. (**B**) Plasma dC, (**C**) dT, (**D**) dA, and (**E**) dG concentrations for indicated species. The dT concentration in the NHP plasma was below the lowest limit of detection for the assay (10 nM). n = 5 subjects per group for human and C57BL/6 murine plasma; n = 3 subjects per group for NHP and rat plasma. (**F**) Mice were fasted for 24 h before plasma collection. Plasma dN concentrations were measured by LC-MS/MS-MRM and were normalized to those of the control unstarved group. n = 4 mice per group. N.S., nonsignificant; *P < 0.05; ***P < 0.001. (**G**) [U-$^{13}C_9$,$^{15}N_3$]dC (5 μM) is more rapidly deaminated to [$^{13}C_9$,$^{15}N_2$]dU upon 60-min incubation with human plasma (Top) than mouse plasma (Bottom). The deamination of dC was blocked by treating human plasma samples with 100 μM THU, a specific CDA inhibitor (Middle).

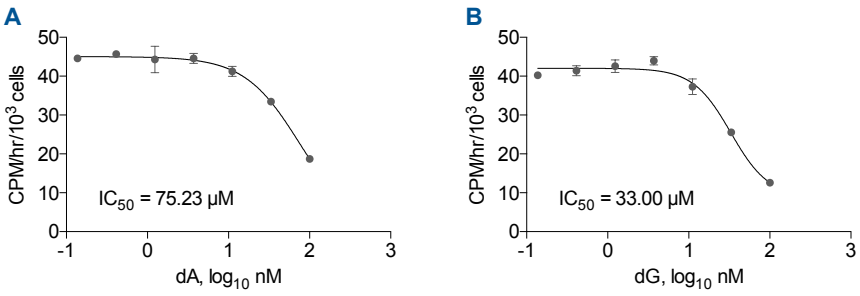

Fig. 1.4. The endogenous dCK substrates dA and dG compete with [^{3}H]CFA uptake.

[^{3}H]CFA (9.25 kBq) uptake for 1 h in CEM WT cells in the presence of varying concentrations of (**A**) dA and (**B**) dG. n = 3 triplicates.

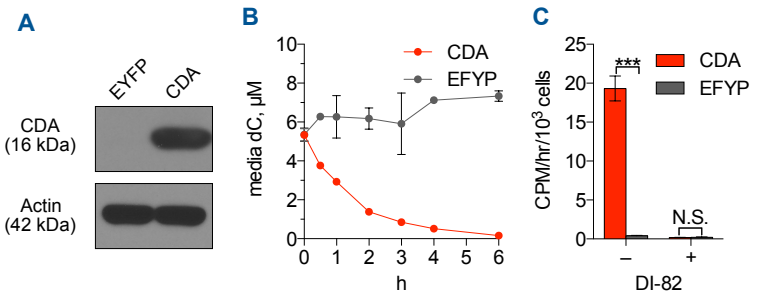

Fig. 1.5. Increased CDA expression reduces dC levels and increases [^{3}H]CFA accumulation by CEM leukemia cells. (**A**) Western Blot for CDA expression in CEM cells engineered to express EYFP or CDA. (**B**) LC-MS/MS-MRM measurements of dC levels in culture supernatants from these cells incubated for the indicated times with 5 μM [U-$^{13}C_9$,$^{15}N_3$]dC. n = 3. (**C**) [^{3}H]CFA (9.25 kBq) uptake (over 1 h) in the isogenic panel described in A, after 6 h of incubation in medium supplemented with dC (5 μM) ± DI-82 (1 μM). N.S., nonsignificant; ***P < 0.001. Results are representative of three independent experiments (n = 3 for each group).

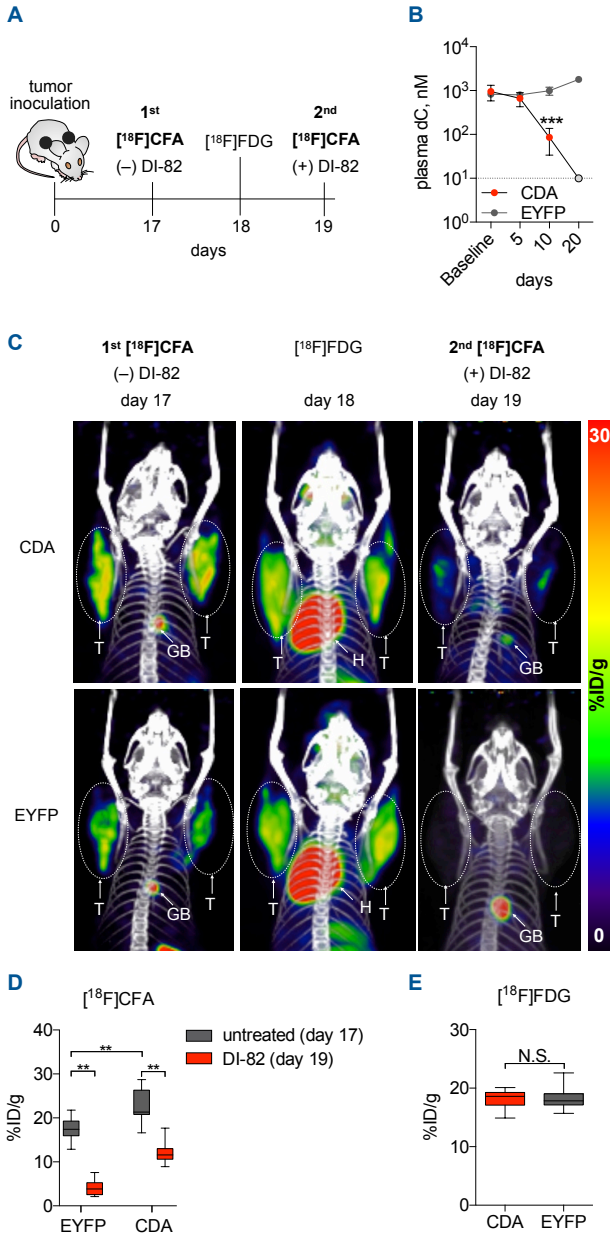
A
tumor inoculation
1st [18F]CFA (–) DI-82
[18F]FDG
2nd [18F]CFA (+) DI-82
0
17
18
19
days
B
plasma dC, nM
***
CDA
EYFP
Baseline
5
10
20
days
C
1st [18F]CFA (–) DI-82 day 17
[18F]FDG day 18
2nd [18F]CFA (+) DI-82 day 19
CDA
EYFP
T
GB
H
30
%ID/g
0
D
[18F]CFA
untreated (day 17)
DI-82 (day 19)
%ID/g
EYFP
CDA
E
[18F]FDG
N.S.
%ID/g
CDA
EYFP

Fig. 1.6. Increased CDA expression in tumor xenografts is sufficient to reduce plasma dC levels in mice and to increase dCK-dependent tumor [^{18}F]CFA accumulation. (**A**) Experimental design and timeline. (**B**) Plasma dC levels in tumor-bearing mice were measured at the indicated times. On day 20 post-tumor inoculation, plasma dC concentration in the NSG mice injected with CEM-CDA cells was below 10 nM (gray circle), which corresponds to the lowest limit of detection of the LC-MS/MS-MRM assay. ***P < 0.001; n = 5 mice per group. (**C**) Representative PET/CT scans of a mouse that was serially imaged with [^{18}F]CFA (day 17), with [^{18}F]FDG (day 18), and then again with [^{18}F]CFA on day 19, 2 h after treatment with DI-82 (50 mg/kg in 50% PEG/Tris, pH 7.4, by i.p. injection). GB, gallbladder; H, heart; %ID/g, percentage injected dose per gram; T, tumor. (**D and E**) Quantification of [^{18}F]CFA and [^{18}F]FDG PET/CT scans from C. N.S., nonsignificant; **P < 0.01; n = 5 mice per group.

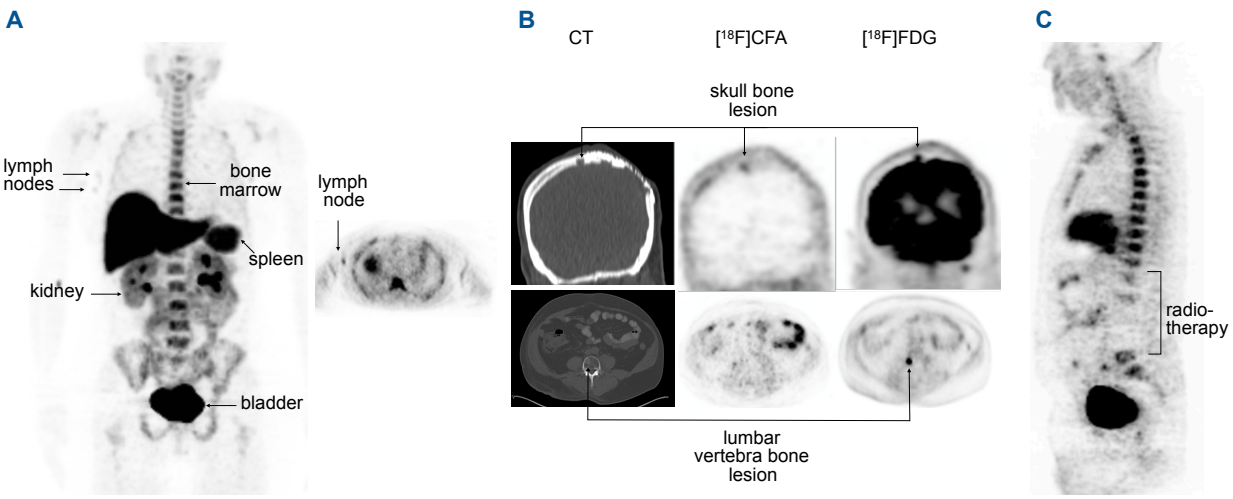

Fig. 1.7. [^{18}F]CFA PET CT images in humans. (**A**) Images of [^{18}F]CFA biodistribution in a healthy volunteer. Maximum intensity 2D projection whole body image (Left) and cross-sectional tomographic image (Right) of the axilla indicating probe accumulation in the lymph nodes. (**B**) [^{18}F]CFA PET/CT and [^{18}F]FDG PET/CT images of a paraganglioma patient showing variability in [^{18}F]CFA accumulation between the skull lesion and the vertebra lesion. (**C**) Whole body [^{18}F]CFA image of the same patient as in B, showing reduced probe accumulation in previously irradiated lumbar spine region.

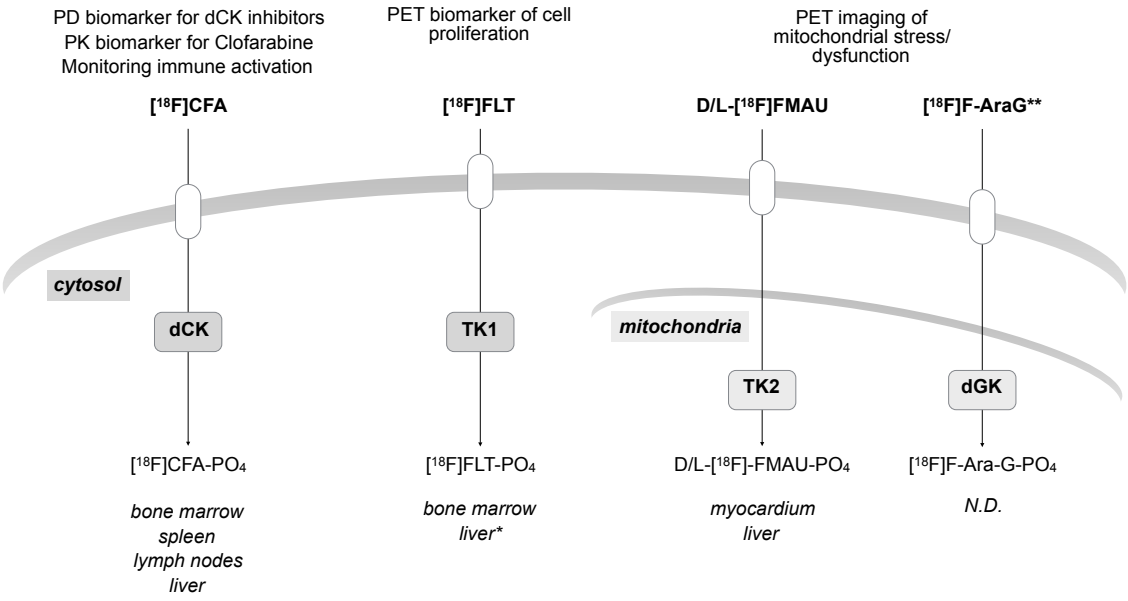

Fig. 1.8. The current toolbox of PET probes for nucleotide metabolism. Proposed matching of PET probes with deoxyribonucleoside salvage kinases. [^{18}F]FLT, 3′-[^{18}F]fluoro-3′ deoxythymidine (48); L-[^{18}F]FMAU, 2′-deoxy-2′-[^{18}F]fluoro-5-methyl-1-β-L-arabinofuranosyluracil (47, 49); D-[^{18}F]FMAU, 2′-deoxy-2′-[^{18}F]fluoro-5-methyl-1-β-D-arabinofuranosyluracil (50, 51). Potential applications for these probes, as well as anatomical sites of preferential accumulation in healthy volunteers, are indicated. *, [^{18}F]FLT accumulation in the liver reflects probe glucuronidation (52). N.D., not determined; PD, pharmacodynamic; PK, pharmacokinetic. **, [^{18}F]F-AraG uptake may also reflect dCK activity.

REFERENCES

1. Reichard P (1988) Interactions between deoxyribonucleotide and DNA synthesis. *Annu Rev Biochem* 57:349–374.
2. Sabini E, Hazra S, Ort S, Konrad M, Lavie A (2008) Structural basis for substrate promiscuity of dCK. *J Mol Biol* 378(3):607–621.
3. Toy G *et al.* (2010) Requirement for deoxycytidine kinase in T and B lymphocyte development. *Proc Natl Acad Sci U S A* 107:5551–5556.
4. Austin WR *et al.* (2012) Nucleoside salvage pathway kinases regulate hematopoiesis by linking nucleotide metabolism with replication stress. *J Exp Med* 209:2215–2228.
5. Murphy JM *et al.* (2013) Development of new deoxycytidine kinase inhibitors and noninvasive in vivo evaluation using positron emission tomography. *J Med Chem* 56:6696–6708.
6. Nathanson DA *et al.* (2014) Co-targeting of convergent nucleotide biosynthetic pathways for leukemia eradication. *J Exp Med* 211:473–486.
7. Jordheim L, Galmarini CM, Dumontet C (2003) Drug resistance to cytotoxic nucleoside analogues. *Curr Drug Targets* 4:443–460.
8. Radu CG *et al.* (2008) Molecular imaging of lymphoid organs and immune activation by positron emission tomography with a new [18F]-labeled 2'-deoxycytidine analog. *Nat Med* 14:783–788.
9. Laing RE *et al.* (2009) Noninvasive prediction of tumor responses to gemcitabine using positron emission tomography. *Proc Natl Acad Sci U S A* 106:2847–2852.
10. Brewer S *et al.* (2010) Epithelial uptake of [18F]1-(2'-deoxy-2'-arabinofuranosyl) cytosine indicates intestinal inflammation in mice. *Gastroenterology* 138:1266–1275.
11. Nair-Gill E *et al.* (2010) PET probes for distinct metabolic pathways have different cell specificities during immune responses in mice. *J Clin Invest* 120:2005–2015.

12. Schwarzenberg J *et al.* (2011) Human biodistribution and radiation dosimetry of novel PET probes targeting the deoxyribonucleoside salvage pathway. *Eur J Nucl Med Mol Imaging* 38(4):711–721.
13. Ho DH (1973) Distribution of kinase and deaminase of 1-beta-D-arabinofuranosylcytosine in tissues of man and mouse. *Cancer Res* 33:2816–2820.
14. Shu CJ *et al.* (2010) Novel PET probes specific for deoxycytidine kinase. *J Nucl Med* 51:1092–1098.
15. Mosessian S *et al.* (2014) INDs for PET molecular imaging probes-approach by an academic institution. *Mol Imaging Biol* 16:441–448.
16. Verri A, Priori G, Spadari S, Tondelli L, Focher F (1997) Relaxed enantioselectivity of human mitochondrial thymidine kinase and chemotherapeutic uses of L-nucleoside analogues. *Biochem J* 328:317–320.
17. Kamath VG, Hsiung CH, Lizenby ZJ, McKee EE (2015) Heart mitochondrial TTP synthesis and the compartmentalization of TMP. *J Biol Chem* 290:2034–2041.
18. Arnér ES, Eriksson S (1995) Mammalian deoxyribonucleoside kinases. *Pharmacol Ther* 67(2):155–186.
19. Namavari M *et al.* (2011) Synthesis of 2'-deoxy-2'-[18F]fluoro-9-β-D-arabinofuranosylguanine: a novel agent for imaging T-cell activation with PET. *Mol Imaging Biol* 13:812–818.
20. Jüllig M, Eriksson S (2000) Mitochondrial and submitochondrial localization of human deoxyguanosine kinase. *Eur J Biochem* 267:5466–5472.
21. Gower WRJ, Carr MC, Ives DH (1979) Deoxyguanosine kinase. Distinct molecular forms in mitochondria and cytosol. *J Biol Chem* 254:2180–2183.
22. Eriksson S *et al.* (1994) Properties and levels of deoxynucleoside kinases in normal and tumor cells; implications for chemotherapy. *Adv Enzyme Regul* 34:13–25.

23. Lotfi K *et al.* (2006) The pattern of deoxycytidine- and deoxyguanosine kinase activity in relation to messenger RNA expression in blood cells from untreated patients with B-cell chronic lymphocytic leukemia. *Biochem Pharmacol* 71:882–890.
24. Owens JK, Shewach DS, Ullman B, Mitchell BS (1992) Resistance to 1-beta-D-arabinofuranosylcytosine in human T-lymphoblasts mediated by mutations within the deoxycytidine kinase gene. *Cancer Res* 52:2389–2393.
25. Nomme J *et al.* (2014) Structure-guided development of deoxycytidine kinase inhibitors with nanomolar affinity and improved metabolic stability. *J Med Chem* 57:9480–9494.
26. Dandekar M, Tseng JR, Gambhir SS (2007) Reproducibility of 18F-FDG microPET studies in mouse tumor xenografts. *J Nucl Med* 48:602–607.
27. Tseng JR *et al.* (2005) Reproducibility of 3'-deoxy-3'-(18)F-fluorothymidine microPET studies in tumor xenografts in mice. *J Nucl Med* 46:1851–1857.
28. Plotnik DA, Emerick LE, Krohn KA, Unadkat JD, Schwartz JL (2010) Different modes of transport for 3H-thymidine, 3H-FLT, and 3H-FMAU in proliferating and nonproliferating human tumor cells. *J Nucl Med* 51:1464–1471.
29. Adams A, Harkness RA (1976) Adenosine deaminase activity in thymus and other human tissues. *Clin Exp Immunol* 26:647–649.
30. Markert ML (1991) Purine nucleoside phosphorylase deficiency. *Immunodefic Rev* 3:45–81.
31. Nottebrock H, Then R (1977) Thymidine concentrations in serum and urine of different animal species and man. *Biochem Pharmacol* 26:2175–2179.
32. van Waarde A *et al.* (2004) Selectivity of 18F-FLT and 18F-FDG for differentiating tumor from inflammation in a rodent model. *J Nucl Med* 45(4):695–700.
33. Cooper GM, Greer S (1973) The effect of inhibition of cytidine deaminase by tetrahydrouridine on the utilization of deoxycytidine and 5-bromodeoxycytidine for deoxyribonucleic acid synthesis. *Mol Pharmacol* 9:698–703.

34. Zhenchuk A, Lotfi K, Juliusson G, Albertioni F (2009) Mechanisms of anti-cancer action and pharmacology of clofarabine. *Biochem Pharmacol* 78:1351–1359.
35. Lee JT, Campbell DO, Satyamurthy N, Czernin J, Radu CG (2012) Stratification of nucleoside analog chemotherapy using 1-(2'-deoxy-2'-18F-fluoro-β-D-arabinofuranosyl)cytosine and 1-(2'-deoxy-2'-18F-fluoro-β-L-arabinofuranosyl)-5-methylcytosine PET. *J Nucl Med* 53:275–280.
36. King KM *et al.* (2006) A comparison of the transportability, and its role in cytotoxicity, of clofarabine, cladribine, and fludarabine by recombinant human nucleoside transporters produced in three model expression systems. *Mol Pharmacol* 69(1):346–353.
37. Matsuoka S *et al.* (2007) ATM and ATR substrate analysis reveals extensive protein networks responsive to DNA damage. *Science* 316:1160–1166.
38. Yang C *et al.* (2012) Deoxycytidine kinase regulates the G2/M checkpoint through interaction with cyclin-dependent kinase 1 in response to DNA damage. *Nucleic Acids Res* 40:9621–9632.
39. Bunimovich YL *et al.* (2014) Deoxycytidine kinase augments ATM-Mediated DNA repair and contributes to radiation resistance. *PLoS One* 9:e104125.
40. Pui CH, Jeha S, Kirkpatrick P (2005) Clofarabine. *Nat Rev Drug Discov* 4(5):369–370.
41. Cohen JD, Strock DJ, Teik JE, Katz TB, Marcel PD (1997) Deoxycytidine in human plasma: potential for protecting leukemic cells during chemotherapy. *Cancer Lett* 116:167–175.
42. Osborne WR *et al.* (1977) Purine nucleoside phosphorylase deficiency. Evidence for molecular heterogeneity in two families with enzyme-deficient members. *J Clin Invest* 60:741–746.
43. Hirschhorn R, Roegner V, Rubinstein A, Papageorgiou P (1980) Plasma deoxyadenosine, adenosine, and erythrocyte deoxyATP are elevated at birth in an adenosine deaminase-deficient child. *J Clin Invest* 65:768–771.

44. Venner PM *et al.* (1981) Levels of 2'-deoxycoformycin, adenosine, and deoxyadenosine in patients with acute lymphoblastic leukemia. *Cancer Res* 41:4508–4511.

45. Mitchell BS, Edwards NL, Koller CA (1983) Deoxyribonucleoside triphosphate accumulation by leukemic cells. *Blood* 62:419–424.

46. Fukuda Y, Schuetz JD (2012) ABC transporters and their role in nucleoside and nucleotide drug resistance. *Biochem Pharmacol* 83:1073–1083.

47. Campbell DO *et al.* (2012) Structure-guided engineering of human thymidine kinase 2 as a positron emission tomography reporter gene for enhanced phosphorylation of non-natural thymidine analog reporter probe. *J Biol Chem* 287(1):446–454.

48. Shields AF *et al.* (1998) Imaging proliferation in vivo with [F-18]FLT and positron emission tomography. *Nat Med* 4:1334–1336.

49. Mukhopadhyay U, Pal A, Gelovani JG, Bornmann W, Alauddin MM (2007) Radiosynthesis of 2'-deoxy-2'-[18F]-fluoro-5-methyl-1-beta-L-arabinofuranosyluracil ([18F]-L-FMAU) for PET. *Appl Radiat Isot* 65:941–946.

50. Alauddin MM, Shahinian A, Gordon EM, Conti PS (2002) Evaluation of 2'-deoxy-2'-flouro-5-methyl-1-beta-D-arabinofuranosyluracil as a potential gene imaging agent for HSV-tk expression in vivo. *Mol Imaging* 1:74–81.

51. Tehrani OS, Douglas KA, Lawhorn-Crews JM, Shields AF (2008) Tracking cellular stress with labeled FMAU reflects changes in mitochondrial TK2. *Eur J Nucl Med Mol Imaging* 35:1480–1488.

52. Shields AF (2003) PET imaging with 18F-FLT and thymidine analogs: promise and pitfalls. *J Nucl Med* 44:1432–1434.

53. Hamacher K, Coenen HH, Stocklin G (1986) Efficient stereospecific synthesis of no-carrier-added 2-[18F]-fluoro-2-deoxy-D-glucose using aminopolyether supported nucleophilic substitution. *J Nucl Med* 27:235–238.

CHAPTER 2

Lysosome inhibition sensitizes pancreatic cancer to replication stress by aspartate depletion

ABSTRACT

Functional lysosomes are required for autophagy and macropinocytosis, the intra- and extracellular scavenging pathways cancer cells engage for nutrient acquisition. Pancreatic ductal adenocarcinoma (PDAC) tumors exhibit high basal lysosomal activity, and genetic or pharmacologic inhibition of lysosome function suppresses PDAC cell proliferation and tumor growth. However, the codependencies induced by lysosomal inhibition in PDAC have not been systematically explored. Here, we performed a comprehensive pharmacological inhibition screen of the protein kinome and found that replication stress response inhibitors were synthetically lethal with chloroquine (CQ) in PDAC cells. CQ treatment reduced *de novo* nucleotide biosynthesis and induced replication stress. We found that CQ treatment caused mitochondrial dysfunction and depletion of aspartate, an essential precursor for *de novo* nucleotide synthesis, as an underlying mechanism. Supplementation with aspartate partially rescued the phenotypes induced by CQ. The synergy of CQ and the replication stress response inhibitor VE-822 was comprehensively validated in both two-dimensional and three-dimensional cultures of PDAC cell lines, in heterotypic spheroid culture with cancer-associated fibroblasts, and in *in vivo* xenograft and syngeneic PDAC mouse models. These results indicate a codependency on functional lysosomes and an intact replication stress response pathway in PDAC, and support the translational potential of the combination of CQ and replication stress response inhibitors.

INTRODUCTION

Pancreatic ductal adenocarcinoma (PDAC) is the fourth leading cause of cancer-related death in the United States and its incidence is steadily increasing (1). PDAC carries a 5-year survival of less than 10%, as it is often diagnosed at a late stage and is widely refractory to available therapies. This lack of effective treatment options suggests an incomplete understanding of the biologic complexity of PDAC and its mechanisms of therapeutic resistance.

PDAC tumors are characteristically hypoperfused, resulting in poor nutrient delivery (2). To exist in this hostile microenvironment, PDAC tumor cells increase reliance on intracellular and extracellular scavenging pathways to acquire the substrates required to sustain tumor growth. Autophagy, a highly conserved self-degradative mechanism employed to recycle damaged cytosolic proteins and organelles, and macropinocytosis, the process by which cells uptake bulk extracellular material, are upregulated in PDAC (3-6). As the final step of both autophagy and macropinocytosis, the autophagic and endocytic cargo fuse with the lysosome, where macromolecules are degraded by pH-dependent enzymes and substrates for metabolism are released (3, 4, 7). Genetic or pharmacologic inhibition of these scavenging pathways suppresses PDAC tumor growth and prolongs survival in animal models (4, 6, 8). Additionally, engaging autophagic programs confers resistance to chemoradiation in PDAC cells (9-11) and high levels of autophagy markers have been correlated with worse survival in resected PDAC patients (12).

The study of lysosomal function is often focused on proteolysis, which degrades misfolded proteins and damaged organelles, and recycles amino acids for protein anabolism and redox and energy homeostasis (13, 14). However, lysosomal degradation pathways also play a critical role in lipid (15-17) and nucleic acid metabolism. Delivered to lysosomes in bulk autophagic or endocytic vesicles, or directly imported via dedicated transporters , the recycling of nucleic acid species by lysosomes maintains genomic integrity and regulates immune sensing of pathogen or aberrant self DNA and RNA (18). Recent work indicates lysosomes also supply metabolic substrates to maintain intracellular nucleotide pools in cancer cells (14).

DNA replication and cancer cell proliferation require a sufficient supply of nucleotides. Two convergent pathways exist for nucleotide synthesis: (i) the *de novo* pathway, which synthesizes nucleotides from glucose and amino acid precursors, and (ii) the nucleoside salvage pathway, which recycles nucleosides (19, 20). Co-targeting these convergent nucleotide biosynthetic pathways has been shown to effectively inhibit cancer progression (21, 22). In response to nucleotide insufficiency, cells engage the replication stress response pathway, a signaling cascade mediated by ataxia telangiectasia and Rad3-related protein (ATR) and its downstream effectors, the checkpoint kinases CHEK1 and WEE1. Activation of this pathway coordinates cell cycle checkpoint activation, replication fork stabilization, restoration of nucleotide pools, and ultimately firing of new replication origins. We have previously shown that the ATR inhibitor VE-822, which is currently in Phase I/II clinical trials for multiple cancer types, sensitizes cancer cells to the inhibition of nucleotide biosynthesis (23).

Extensively used in human patients for decades for various indications, chloroquine (CQ) and its derivatives de-acidify lysosomes, thus inhibiting autophagy and macropinocytosis (24). These agents have been investigated in multiple cancers, but have thus far shown limited efficacy in PDAC as monotherapy or in combination with standard of care therapies (25-27). In this study, we performed an unbiased kinome inhibition screen to identify previously unexplored vulnerabilities of CQ-treated PDAC cells and found the replication stress pathway to be the most prominent codependency. We validated the synthetic lethality of CQ and the replication stress response inhibitor VE-822 in multiple *in vitro* and *in vivo* PDAC models. Mechanistically, we found that lysosome inhibition led to mitochondrial dysfunction and decreased intracellular aspartate, resulting in decreased *de novo* nucleotide synthesis, thereby inducing replication stress.

MATERIALS AND METHODS

Cell culture

MiaPaca2, CFPAC1, Panc03.27 and Panc1 cells were purchased from the American Type Culture Collection (ATCC). DANG, L3.6pl, YAPC and MiaPaca2-GFP cells were provided by Dr. David Dawson (UCLA). KPC cells were provided by Dr. Guido Eibl (UCLA). Primary human cancer-associated fibroblasts were isolated from surgical pancreatic cancer specimens by a previously described outgrowth method under an institutional review board approved protocol (51) and characterized by wild-type KRAS status and α-smooth muscle actin positivity as previously described (52). The primary PDAC model XWR200 was developed from a PDAC patient at UCLA. Primary PDAC models A2.1 and A13A were provided by Dr. Christine A. Iacobuzio-Donahue at Memorial Sloan Kettering Cancer Center. All cells used for experiments were between passages 3 and 20 and maintained in antibiotic free DMEM+10% FBS, at 37ºC in 5% CO_2. Cells were routinely authenticated and checked for *Mycoplasma* contamination using MycoAlert kit (Lonza).

Antibodies

pCHEK1 (#2348), CHEK1 (#2360), LC3B (#3868), and GAPDH (#5174) were from Cell Signaling Technology.

Drugs

Chloroquine diphosphate salt (Sigma) was suspended in deionized water. The following drugs were suspended in DMSO: VE822, VE821, CHIR-124, AZD6638, AZD7762, LY, PF (Selleckchem).

Small molecule kinome library screen

A library of 430 protein kinase inhibitors (SelleckChem Cat. L1200) was arrayed in polypropylene 384-well plates at 200x concentrations covering a 7-point concentration range

(corresponding to 1x concentrations: 5μM, 1.65μM, 550nM, 185nM, 61.5nM, 20.6nM, 6.85nM). 25μl per well of growth media with or without 40μM CQ supplementation (for a final concentration of 20μM) was plated in opaque-white 384-well plates using a BioTek multidrop liquid handler. Protein kinase inhibitors were added by 250nL pin-tool transfer (BioMek FX, Beckman-Coulter) and inhibitor/media mixtures were incubated at room temperature for 30m. 25μL of a 40,000 cells/mL MiaPaca2 suspension (for 1000 cells / well) was subsequently added to each well. After 72h, 50μL of CellTiter-Glo reagent diluted 1:4 in PBS was added to each well and luminescence readings were performed using a Wallac plate reader (Perkin Elmer). Each condition was assayed in duplicate (n=2) and % proliferation values were calculated by normalizing experimental wells to plate negative controls and averaging replicate values. Composite CQ synergy scores for each test compound were defined as the sum of the Bliss Additivity Score (% proliferation inhibition observed - % proliferation inhibition expected) between CQ and individual protein kinase inhibitor concentrations across the 7-point concentration range. Z factor scores for individual assay plates were calculated using eight positive and eight negative control wells on each plate as previously described (53). All plates gave a Z factor > 0.5.

Proliferation assay

Cells were plated in 96-well plates (2,000 cells/well). Drugs or DMSO vehicle control were added 24h after plating. After 72h incubation, ATP content was measured using CellTiter-Glo reagent and analyzed by SpectraMax luminometer (Molecular Devices).

pH2A.X assay

Cells were harvested, fixed, permeabilized with cytofix/cytoperm (BD biosciences, #554722) for 15m on ice, prior to staining with a phospho-Histone H2A.X (Ser139) antibody conjugated to fluorochrome FITC (EMD Millipore, #05- 636, 1:800 dilutions in perm/wash) for 20m in the dark

at room temperature. Subsequently, cells were washed and stained with 0.5mL of DAPI (Invitrogen, #D1306) for DNA content before data acquisition by flow cytometry.

5-ethynyl2-deoxyuridine (EdU) cell cycle profiling

MiaPaca2 cells were plated at 0.3 x 10^6 cells/mL, pulsed with 10μM EdU (Invitrogen) for 2h, washed twice with PBS, and released in fresh media containing 5μM deoxyribonucleosides. Cells were collected 4h following release in fresh media, and then fixed with 4% paraformaldehyde and permeabilized using saponin perm/wash reagent (Invitrogen), and then stained with azide-Alexa Fluor 647 by Click reaction (Invitrogen; Click-iT EdU Flow cytometry kit, #C10634). The total DNA content was assessed by staining with FxCycle-Violet (Invitrogen, #F10347) at 1 μg/mL final concentration. Flow cytometry data were acquired on five-laser LSRII cytometers (BD), and analyzed using FlowJo software (Tree Star). The cell cycle durations were calculated using equations for multiple time-point measurements according to previously published methods (Terry and White, 2006).

Seahorse respirometry assay

Respirometry assays were performed as described (54). MiaPaca2 cells were plated into an XF96 microplate at a density of 15,000 cells per well. CQ was either injected during the respirometry assay or added to the cell culture 24 hours prior to the measurement. The mitochondrial stress test conditions included injection of 2 μM oligomycin, 0.9 μM FCCP, 2 μM antimycin A and rotenone. Oxygen consumption rates were normalized to cellular protein content per well.

Mitochondrial membrane potential measurements

$\Delta\psi_m$ was measured by quantifying the average fluorescence intensity of cells stained with the combination of MTG and TMRE before and after indicated treatments, as described in detail (55).

Western blotting

Cells were lysed in cold RIPA lysis buffer with protease and phosphatase inhibitors (Thermo Scientific). Protein extracts were resolved on SDS-PAGE and then electrotransferred to Immun-Blot PVDF membrane (Bio-Rad, Hercules, CA, USA). After blocking, membranes were probed with the indicated primary antibodies at 4˚C overnight, and then with horseradish peroxidase-conjugated secondary antibody at room temperature for 1h. Blots were developed using Pierce ECL Substrate (Thermo Scientific, Rockford, IL) and imaged on the LI-COR Oddessy imaging system.

[^{14}C]Asp uptake assay

[^{14}C]Asp uptake assay was performed as described (39). MiaPaca2 cells were pretreated with 20 μM CQ for 24 or 48 h prior to the incubation with 0.1 μCi of [^{14}C]Asp.

Intracellular metabolite extraction and LC-MS analysis

Metabolite measurements were performed according to previously described protocols (56). Briefly, after 48h exposure to treatment, cells were washed with ice-cold 150mM ammonium acetate, and scraped in 1mL ice-cold 80% methanol, with an internal standard mixture of 17 isotope-labeled amino acids (100nM each, Cambridge Isotope Laboratories MSK-A2-1.2). After vigorous vortexing, the samples were centrifuged at 12,000rpm. Supernatants were transferred into glass vials and the metabolites dried under vacuum. Metabolites were resuspended in 50μl 70% acetonitrile (ACN), and 5μl was used for mass spectrometer-based analysis, performed on a Q Exactive (Thermo Scientific) instrument, with polarity-switching (+3.50 kV/-3.50 kV) in full scan mode. Separation was achieved using A) 5mM NH_4AcO (pH 9.9) and B) ACN. The gradient started with 15% A) going to 90% A) over 18m, followed by an isocratic step for 9m and reversal to the initial 15% A) for 7m. Metabolites were quantified with TraceFinder 3.3 using accurate mass measurements (≤ 3ppm), as well as retention times and fragmentation patterns

of purchased compounds. Data analysis was performed by Elucidata (Cambridge, MA and New Delhi, India).

Sample preparation for LC-MS/MS-MRM analysis of nucleotides pools and incorporation of labeled nucleotides into newly replicated DNA and RNA

Cells were cultured in DMEM without glucose or glutamine + 10% dialyzed FBS (Gibco) and 4mM glutamine (Gibco) containing [U-$^{13}C_6$]glucose (Sigma-Aldrich, 389374) at 1g/L. Prior to sample collection, labeled media was aspirated and cells washed, then collected by trypsinization. Cells were pelleted then lysed with 10µL of 10% trifluoroacetic acid with internal standards (1µM [$^{15}N_3$]dCMP and [$^{15}N_3$]dCTP, Silantes # 122303802 and # 120303802, respectively) vortexed for 30s, and incubated on ice for 10m. 40µL of 1M ammonium acetate, pH=10, with the same internal standard added and the samples vortexed again for 30s, and centrifuged to remove insoluble cellular material. The supernatants (~40µL) were transferred into HPLC injector vials. Stock solutions (10 mM) of rCTP, rATP, rGTP rUTP, dCTP, dATP, dGTP, and dTTP (Sigma Aldrich) used to generate reference standards, and were processed prior to dNTP as metrics of LC-MS/MS-MRM signal and proportionally compared to previous runs to account for signal variation.

Genomic DNA was extracted using the Quick-gDNA MiniPrep kit (Zymo Research, D3021) and hydrolyzed to nucleosides using the DNA Degradase Plus kit (Zymo Research, E2021). RNA was isolated using Clontech Nucleospin II RNA Kit (#740955). In the final step of DNA and RNA extraction, 50µL of water was used to elute DNA or RNA into 1.5mL microcentrifuge tubes. A nuclease solution (5µL; 10X buffer/DNA Degradase Plus™/water, 2.5/1/1.5, v/v/v) was added to 20µL of the eluted genomic DNA or RNA in an HPLC injector vial.

Targeted LC-MS/MS-MRM assays

For free nucleotide analysis, a modified version of the previously reported method (57) was used in which each dNTP lysate sample (15µL) was injected directly onto the Hypercarb column equilibrated in solvent A (5mM hexylamine and 0.5% diethylamine, v/v, pH 10.0) and eluted (200 µL/min) with an increasing concentration of solvent B (acetonitrile/water, 50/50, v/v) at the following min/%B/flow rates (µL/min): 0/5/200, 20/100/200, 20.50/100/600, 22.50/100/600, 23/5/600, 25/5/600, 25.5/5/200, 28/5/200. The effluent from the column was directed to the Agilent Jet Stream ion source connected to the triple quadrupole mass spectrometer (Agilent 6460) operating in the multiple reaction monitoring (MRM) mode using previously optimized settings. The peak areas for each nucleosides and nucleotides (precursor→fragment ion transitions) at predetermined retention times were recorded using software supplied by the instrument manufacturer (Agilent MassHunter).

For RNA and DNA analyses, an aliquot of the hydrolyzed sample (15 µL) was injected onto a porous graphitic carbon column (Thermo Fisher Scientific Hypercarb, 100 x 2.1mm, 5µm particle size) equilibrated in solvent A (water 0.1% formic acid, v/v) and eluted (200 µL/min) with an increasing concentration of solvent B (acetonitrile 0.1% formic acid, v/v) using min/%B/flow rates (µL/min) as follows: 0/0/700, 3.5/70/700, 4.5/70/700, 5/0/700, 7/0/7.

Quantification of LC-MS/MS-MRM data

The areas for nucleotide measurements were obtained from extracted ion chromatograms of MRM ion transitions. These measurements were normalized from the spiked internal standards ([15N3]dCMP and [15N3]dCTP). Nucleotide data was normalized to cell number and is displayed as relative amount per cell compared to untreated. For DNA and RNA, the areas for the hydrolyzed labeled nucleosides were obtained from extracted ion chromatograms of MRM ion transitions, and normalized to total ion current at that retention time.

***In vitro* tumor cell-fibroblast 3D co-culture**

$1x10^3$ MiaPaca-GFP cells were plated in U-bottom black-walled 96-well plates (Corning). After 48h, $8x10^3$ primary fibroblasts were added (day 0). 72h later spheroids were formed and treatment was initiated. Daily fluorescence readings were taken using a blue optical kit (Ex 490nm/Em 510-570nm) on a Modulus II Microplate Multimode Reader. Images were taken using a CX41 Inverted Microscope with a DP26 Digital Camera (Olympus).

Animal studies

All animal studies were approved by the UCLA Animal Research Committee (ARC). 4-6 week-old male NSG mice were injected subcutaneously on bilateral flanks with 1 million MiaPaca2 or Miapaca2/SLC1A3 cells. 6-10 week-old C57Bl/6 female mice were injected subcutaneously on bilateral flanks with $5x10^5$ KPC cells. When tumors reached 50-100mm^3 (~7d post-inoculation), treatment was initiated. CQ was suspended in distilled water. VE-822 was suspended in vitamin E TPGS. Both drugs were delivered p.o. at 60 mg/kg 3x per week for two weeks. Syngeneic mice with KPC tumors were sacrificed when tumor volume reached 400 mm^3, because ulcer started showing up on the surface of skin around tumors of 400 mm^3.

Statistical analysis

Data are presented as means ± SD with indicated biological replicates. Comparisons of two groups were calculated using indicated unpaired or paired two-tailed Student's t-test and P values less than 0.05 were considered significant. All statistical analyses were performed in Graphpad Prism 6.0.

RESULTS

Small-molecule kinase inhibitor screen identifies the replication stress pathway as a codependency of impaired lysosome function

A small-molecule kinase inhibitor screen identified the replication stress response-ATR/CHEK1 pathway as the most prominent codependency of CQ-treated MiaPaca2 cells (**Fig. 2.1A**). All eight ATR and CHEK1 inhibitors included in the library scored positively in the screen (data not shown). The synergy between CQ and the eight replication stress response inhibitors was validated in a secondary assay (**Fig. S2.1A**). Among these replication stress response inhibitors, ATR inhibitor VE-822 (also known as VX-970 or Berzosertib) was selected for further analysis due to its translational potential; VE-822 has been shown to have favorable pharmacodynamics and tolerability in animal models (23, 28).The synergy between CQ and VE-822 was confirmed by the combination index (CI) (**Fig. S2.1B**) and in a panel of PDAC cell lines (MiaPaca2, DANG, Panc03.27, CFPAC1) in both 2D monolayer and 3D spheroid culture (**Fig. 2.1B**). The synthetic lethality of the combination of CQ and VE-822 was further supported by the synergistic induction of pH2.AX, a marker of DNA damage (**Fig. 2.1C**). In addition, the synergistic effect of CQ and VE-822 was observed in the majority of human PDAC cell lines and primary PDAC cultures (XWR200, A13A, and A2.1) (**Fig. 2.1D**).

Lysosome inhibition induces replication stress in PDAC lines

We hypothesized that the observed synergy between CQ and replication stress response inhibitors occurred because lysosomal inhibition increased replication stress in PDAC tumor cells. To investigate this, MiaPaca2 cells were treated with CQ and monitored for phosphorylation of CHEK1 at serine 345, an established marker of replication stress response pathway activation. We observed pCHEK1 induction by 8 h after CQ exposure, which continued to increase up to 32 h. Concurrently, accumulation of LC3B was noted to occur in a time-dependent manner, confirming CQ inhibition of maturation of autophagolysosomes (**Fig. 2.2A**). Increasing pCHEK1 induction was also noted with increasing doses of CQ (**Fig. 2.2B**). These

findings were consistent across a panel of PDAC lines, including DANG, Panc0327, YAPC, L3.6pl, and CFPAC-1 (**Fig. 2.2C**). Similar to CQ, other lysosome inhibitors, including ammonium chloride (NH_4Cl, a weak base that prevents lysosome acidification) and Baflomycin A1 (BafA1, a vacuolar H^+-ATPase inhibitor that increases lysosome pH) induced pCHEK1 expression (**Fig. 2.2D**), indicating replication stress response pathway activation is an on-target effect of lysosome inhibition. These lysosomal inhibitors also synergistically inhibited PDAC cell growth when combined with VE-822 (**Fig. S2.2A**). An EdU pulse-chase assay to profile cell cycle kinetics was used as an orthogonal approach to examine replication stress, which occurs at stalled replication forks and, thus, is associated with prolongation of cell cycle S-phase. Consistent with pCHEK1 induction, CQ treatment significantly prolonged S-phase duration and resulted in fewer labeled cells re-entering the G1 phase of the cell cycle (G1*) (**Fig. 2.2E**; **Fig. S2.2B**).

Lysosome inhibition impairs *de novo* nucleotide biosynthesis

Insufficiency of essential replication factors, including replication machinery and, notably, deoxyribonucleotides (dNTPs), is a well-established cause of stalled replication forks and replication stress (29-31). To investigate the effect of CQ on dNTP availability for DNA replication and repair, we used a previously described targeted LC-MS/MS-MRM method to measure heavy-isotope labeled nucleotides, in the form of both free metabolites and hydrolyzed nucleic acids species (DNA/RNA), from cells cultured with [$^{13}C_6$]glucose (23). This method determines the contribution of nucleotides to free dNTP and rNTP pools, and their incorporation into newly synthesized RNA and DNA. CQ treatment significantly decreased all four labeled dNTP pools (dCTP, TTP, dATP, and dGTP) in MiaPaca2, Panc0327 and Panc1 cells (**Fig. 2.3A**), and was associated with a decrease in the % labeling of DNA across all four bases (**Fig. 2.3B**). CQ appeared to selectively inhibit *de novo* dNTP biosynthesis, as unlabeled dNTP pools remained unaffected, or increased, in CQ-treated cells (**Fig. S2.3**). We and others have previously shown that *de novo* produced dNTPs are more readily incorporated into DNA than

those produced by the salvage pathway (unlabeled dNTPs) (21, 32), suggesting that it is the decrease specifically in *de novo* dNTP biosynthesis that causes replication stress in CQ-treated PDAC cells.

To further investigate the source of the defect in *de novo* dNTP synthesis, we assessed the impact of CQ on *de novo* synthesized ribonucleotide pools. Impaired *de novo* dNTP biosynthesis may be caused by a shortage of substrates for nucleotide synthesis (e.g. glucose, amino acids), or by ribonucleotide reductase (RNR) inhibition, preventing RNR reduction of ribonucleotide diphosphates (NDPs) to deoxyribonucleotide diphosphates (dNDPs), the rate-limiting step in *de novo* dNTP production. MiaPaca2 cells cultured with [$^{13}C_6$]glucose ± CQ were analyzed for labeled free NTP pools and their incorporation into RNA. We observed no consistent, significant changes in free NTP pools with CQ treatment, but a decrease in labeled RNA (**Fig. 2.3C and D**), suggesting an overall decrease in *de novo* nucleotide synthesis. Collectively, these results indicate CQ treatment results in impairment of *de novo* synthesis of both dNTPs and NTPs, rather than a defect in conversion to ribo- to dexoxyribonucleotides by RNR.

Lysosome inhibition depletes aspartate, a critical substrate for *de novo* nucleotide biosynthesis

In *de novo* nucleotide biosynthesis, the amino acid precursors aspartate (Asp), glutamine (Gln), glycine (Gly) and serine (Ser) are utilized for purine biosynthesis, while only Asp and Gln are required for the synthesis of pyrimidine ribonucleotides. CQ treatment significantly decreased intracellular Asp levels, while increasing Gln, Gly and Ser levels (**Fig. 2.4A**). As non-Gln amino acids are important sources of carbon and nitrogen biomass in cancer cells (33), we further profiled changes in all amino acids to assess if CQ treatment resulted in a global decrease in non-Gln amino acids, and thus a general decrease in carbon and nitrogen sources. Other than Asp, alanine (Ala) was the only amino acid that exhibited a significant, but smaller, decrease

with CQ treatment (**Fig. 2.4A**). The reduction of Asp was confirmed using an orthogonal Asp assay in MiaPaCa2 and Panc03.27 cells (**Fig. S2.4A**). In addition, CQ treatment increased cellular demand for Asp (**Fig. 2.4B**). These results suggest that Asp is the major amino acid affected by CQ treatment in PDAC cells and that Asp is the limiting substrate for *de novo* nucleotide biosynthesis in the setting of lysosomal inhibition.

We then performed rescue experiments with Asp supplementation to implicate aspartate deficiency as a cause of CQ-induced nucleotide insufficiency and replication stress. Addition of exogenous Asp rescues intracellular Asp levels (**Fig. S2.4B**) and partially restored the decrease in DNA labeling observed with CQ treatment in all four nucleobases (**Fig. 2.4C**) and prevented CQ-induced replication stress, as indicated by lack of phosphorylation of CHEK1 (**Fig. 2.4D**). Asp supplementation also partially rescued CQ- and NH_4Cl-induced growth inhibition in a dose-dependent manner in PDAC cells (**Fig. 2.4E**, **Fig. S2.4C and D**), and partially rescued CQ-induced DNA damage (**Fig. S2.4E**). The growth rescuing effect of Asp exceed those of dNTP substrates (*de novo* substrates: glutamine, serine, glycine- and salvage substrates: rNs and dNs), and other amino acids (**Fig. 2.4F and G**).

Mitochondrial dysfunction contributes to reduction in aspartate levels. We hypothesized that CQ caused mitochondrial dysfunction, decreased electronic transportation chain (ETC) activity, and therefore inhibited Asp biosynthesis (34). To test this hypothesis, we examined mitochondrial membrane potential, a marker of mitochondrial dysfunction (35), in PDAC cells treated with CQ. Chronic but not acute treatment with CQ increased mitochondrial membrane potential (**Fig. 2.5A**), indicating mitochondrial dysfunction (35). In addition, CQ reduced mitochondrial ETC activity (**Fig. 2.5B**), an important function of mitochondria to enable Asp synthesis (34). Pyruvate supplement, which supports Asp synthesis when ETC activity is reduced (35), partially rescued CQ-induced Asp depletion (**Fig. 2.5C**) and inhibition of PDAC cell proliferation (**Fig. 2.5D**).

Lysosome inhibition synergizes with replication stress response inhibitors in complex, organotypic *in vitro* models, and *in vivo*

PDAC tumors are characterized by a dense stroma, primarily comprised by fibroblasts and extracellular matrix (36). These cancer-associated fibroblasts (CAFs) support cancer cell proliferation, migration and invasion, and confer resistance to radiation and chemotherapeutics (37, 38). Therefore, we used a 3D organotypic MiaPaca2/CAF coculture model to assess the efficacy of the CQ/VE822 combination in stroma-rich PDAC tumors. In contrast to monoculture, the growth of the established cocultured spheroids were not affected by VE-822 as a single agent. However, CQ treatment resulted in similar growth inhibition in these cocultures as in 2D monoculture, and the combination showed substantial synergy (**Fig. 2.6A and B**).

In *in vivo* PDAC model, the combination of CQ and VE-822 significantly and synergistically slowed the growth of xenograft MiaPaca2 tumors (**Fig. 2.6C**), whereas overexpression of the Asp transporter SLC1A3 (39) rescued the growth inhibition by CQ and VE-822 (**Fig. S2.5A and B**). The CQ/VE-822 combination significantly reduced the frequency of proliferation marker Ki67-positive cells, and increased the frequencies of DNA damage marker pH2A.X-positive cells and apoptosis marker cleaved Caspase3- and cleaved PARP-positive cells in xenograft MiaPaca2 tumors (**Fig. 2.6D**). Similar to our observations in human PDAC cells, CQ and VE-822 are synergistic in inhibiting the proliferation of cultured murine PDAC KPC cells (**Fig. S2.6A**), which was partially rescued by Asp supplementation (**Fig. S2.6B**). In the *in vivo* syngeneic KPC PDAC tumor model, the combination of CQ and VE-822 significantly slowed tumor growth (**Fig. 2.6E**), and induced DNA damage in syngeneic tumors (**Fig. 2.6F**). Both single and combination therapies were well-tolerated, as indicated by body weight measurement. These results suggest the combination of CQ and VE-822 may represent a promising therapeutic strategy in PDAC.

DISCUSSION

PDAC tumors rely heavily on intracellular and extracellular nutrient scavenging to sustain growth and proliferation. Disabling these pathways with inhibitors of lysosome function has been effective in preclinical models (4), but this strategy has shown limited efficacy in clinical trials (26). A better understanding of how tumor cells respond to lysosomal inhibitors may be required to leverage these agents as potential PDAC therapeutics. Here, we show that pharmacologic inhibition of lysosomal function in PDAC cells depletes intracellular Asp required for *de novo* nucleotide biosynthesis. This results in deoxyribonucleotide insufficiency and an increased reliance on the replication stress response pathway. Further, combination treatment with CQ and a replication stress response inhibitor is synthetically lethal in complex *in vitro* and *in vivo* PDAC models.

Other investigators have shown that deletion of essential autophagy genes decreases nucleotide pools in *Ras*-driven cancers(14). Guo et al. found that nutrient deprivation increases catabolism of ribonucleotides to generate ribose phosphate to maintain energy charge, thereby increasing the reliance on autophagy-generated glutamine for nucleotide biosynthesis. Lung cancer cells deficient of ATG7, an essential regulator of autophagosome assembly, were less efficient at glutamine recycling and exhibited more pronounced ribonucleotide depletion than their autophagy-proficient counterparts under starvation conditions (14). Similarly, Perera et al. found silencing TFE genes, transcription factors regulating lysosomal biogenesis (40), decreased intracellular glutamine and the pyrimidine nucleoside cytidine (3). However, the role of lysosomal function in maintaining deoxyribonucleotide pools to sustain DNA replication and mitigate replication stress in PDAC has not been systematically investigated.

Our data support a model in which CQ treatment critically depletes intracellular Asp in PDAC cells, restricting *de novo* dNTP synthesis. Previous reports addressing how lysosome or autophagy inhibition influences intracellular Asp levels are conflicting. Guo et al. showed that

ATG7-null mouse lung cancer cells exhibited impaired ability to recycle Asp, but, surprisingly, found higher concentrations of Asp in these cells compared to isogeneic ATG7-positive cells. Starvation decreased Asp levels, but to similar levels in both autophagy-proficient and -deficient lines, while Gln was selectively decreased in ATG7-null cells. Viability of autophagy-deficient cells was rescued with Gln, but not Asp, supplementation (14). This contrasts our findings in which Asp, but not Gln, was decreased following lysosomal inhibition and growth inhibition by CQ was most efficiently rescued with Asp supplementation. Zhang et al. found autophagy-proficient and -deficient cells had equivalent concentrations of intracellular Asp which decreased to similar degrees with Gln deprivation (41). The differences in these observations may be due to the unique Gln metabolism pathway in PDAC. Whereas most cells use GLUD1 to convert Gln-derived Glu into α-ketoglutarate in the mitochondria to fuel the TCA cycle, PDAC cells rely on a distinct pathway in which Gln-derived Asp is transported into the cytoplasm, where it can be converted into oxaloacetate by GOT1 (42). In addition, Zhang et al. found the concentration of most amino acids in autophagy-deficient cells increased under starvation conditions due to increased amino acid uptake resulting from upregulation of cell surface transporters (41). Given we observed an increase in the majority of amino acids following CQ treatment, a similar mechanism may occur following lysosomal inhibition. Others have shown that acute pharmacologic lysosomal inhibition with H+V-ATPase inhibitors does not significantly change whole cell levels of Asp, and other non-essential amino acids including Gln, but increases their lysosomal concentrations. This was attributed to decreased efflux of amino acids through lysosomal pH-dependent transporters (43). Collectively, these observations suggest cellular responses to genetic inhibition of autophagy may not phenocopy those of pharmacologic lysosomal inhibition, and that the role of lysosome function in amino acid pool maintenance may be cell- and environment context-specific.

While further investigation is required to determine the mechanism by which lysosomal inhibition decreases Asp levels in PDAC cells, impaired mitochondrial function may contribute to this

effect. Previous work described the importance of mitochondrial respiration in maintaining Asp levels in rapidly proliferating cells (44). Impairment of the electron transport chain (ETC) was shown to decrease availability of electron acceptors required for *de novo* Asp synthesis, decreasing intracellular Asp and purine nucleotide levels, while only modestly affecting Gln levels. Supplementation with Asp, but not Gln was able to restore nucleotide pools and rescue cell proliferation in the setting of ETC inhibition (44). Lysosomal inhibition reduces mitophagy, the specialized autophagy of mitochondria, resulting in an accumulation of dysfunctional mitochondria. Thus, CQ may decrease Asp, and subsequently nucleotide pools, in PDAC cells by impairing mitochondrial function. In line with this, both CQ and bafilomycin A have been shown to impair mitochondrial respiration by affecting mitochondrial quality (45).

The anti-proliferative effects of decreased dNTP availability can be potentiated with inhibitors of the replication stress response pathway. Accordingly, combining replication stress response inhibitors with “traditional” nucleotide antimetabolites, such as hydroxyurea and gemcitabine, has been a promising strategy in cancer therapy (46-48). Similarly, here we show that lysosomal inhibition synergistically impairs PDAC cell proliferation when combined with a replication stress response inhibitor. Previous work identified a synergistic interaction between CQ and inhibitors of CHEK1 in inhibiting growth of colon and osteosarcoma cancer cells (49). However, rather than CQ causing nucleotide insufficiency, the synergy was attributed to the fact that genetic autophagy inhibition has been shown to enhance proteosomal degradation of CHEK1, decreasing protein levels (50), and thereby increasing potency of CHEK1 inhibitors. In our models, pharmacologic lysosome inhibition did not decrease total CHEK1 protein levels, suggesting CQ-induced dNTP pool depletion, leading to increased replication stress, is the primary mechanism underlying this synergy. Importantly, the combination of CQ and ATR inhibition was effective in inhibiting tumor growth of complex *in vitro* models, including 3D heterotypic tumor cell-cancer-associated fibroblast organotypic spheroids, and in syngeneic mouse models. This synthetic lethality indicates a codependency of PDAC cells on functional

lysosomes and an intact replication stress response pathway. Our findings suggest the addition of replication stress response inhibitors could improve the efficacy of lysosomal inhibitors in PDAC and represents a rationally-designed drug combination in this notoriously treatment-resistant disease.

FIGURES

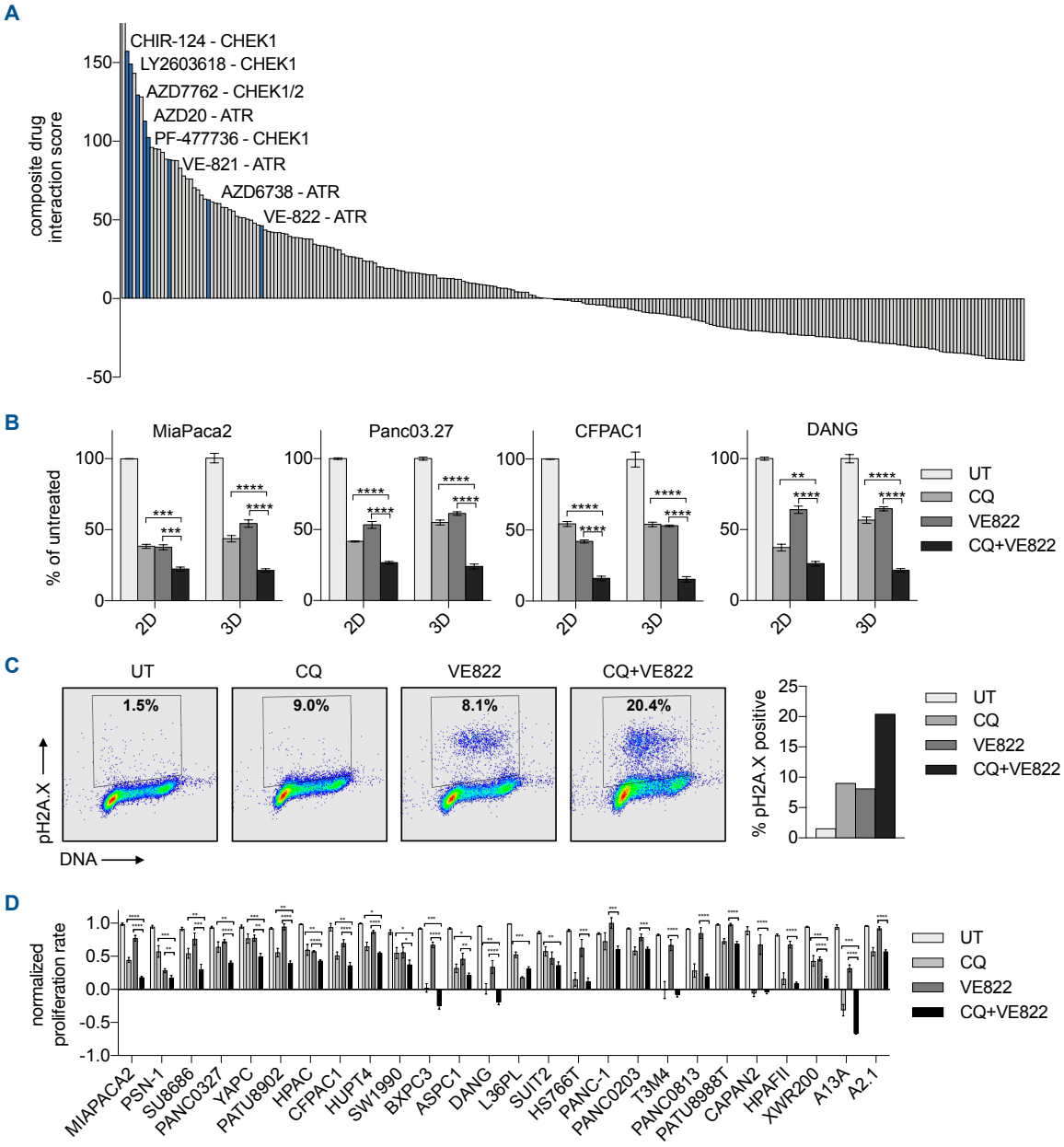
A
composite drug interaction score
CHIR-124 - CHEK1
LY2603618 - CHEK1
AZD7762 - CHEK1/2
AZD20 - ATR
PF-477736 - CHEK1
VE-821 - ATR
AZD6738 - ATR
VE-822 - ATR
B
% of untreated
MiaPaca2
Panc03.27
CFPAC1
DANG
2D
3D
UT
CQ
VE822
CQ+VE822
C
UT
CQ
VE822
CQ+VE822
1.5%
9.0%
8.1%
20.4%
pH2A.X
DNA
% pH2A.X positive
D
normalized proliferation rate
MIAPACA2
PSN-1
SU8686
PANC0327
YAPC
PATU8902
HPAC
CFPAC1
HUPT4
SW1990
BXPC3
ASPC1
DANG
L36PL
SUIT2
HS766T
PANC-1
PANC0203
T3M4
PANC0813
PATU8988T
CAPAN2
HPAFII
XWR200
A13A
A2.1

Fig. 2.1. Replication stress response inhibitors synergize with CQ to inhibit PDAC cell growth. (**A**) Composite drug interaction score of 430 small molecule kinase inhibitors with CQ screened for growth inhibition in MiaPaca2 cells (n=2). (**B**) Viability of a panel of PDAC cells in 2D and 3D culture ± CQ ± VE822 for 72h (n=3); (**C**) Flow cytometry analyses of DNA content and DNA damage marker pH2A.X in MiaPaca2 cells treated ± CQ ± VE822 for 24 h (n=2). (**D**) The anti-proliferation effect of CQ/VE822 combination in a panel of human PDAC cell lines and primary PDAC cultures (XWR200, A13A, and A2.1). | CQ: 20 μM; VE822: 500 nM; ** p<0.01, *** p<0.001, **** p<0.0001.

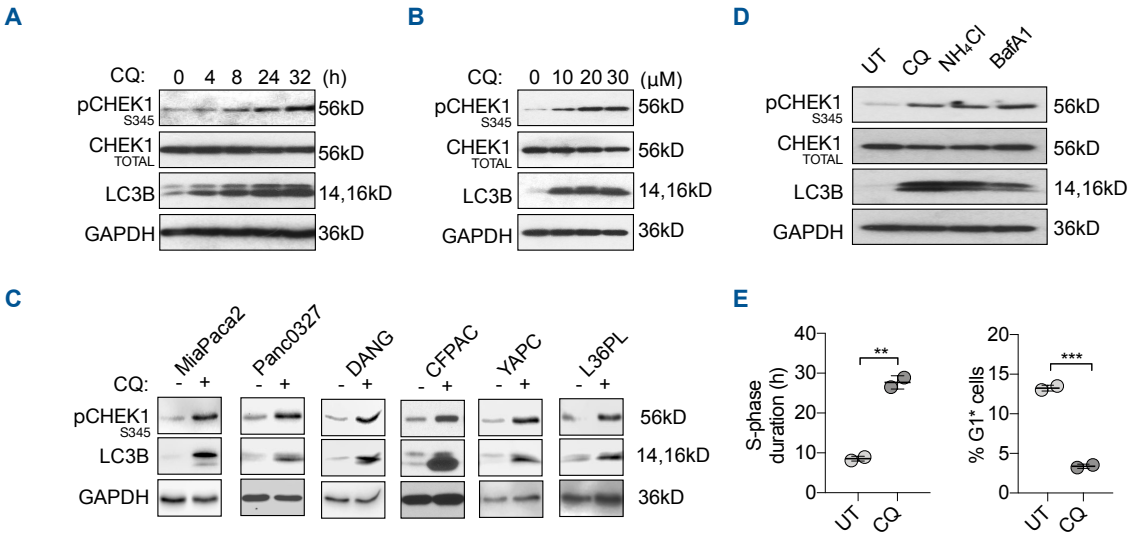

Fig. 2.2. Lysosomal inhibitors induce replication stress in PDAC cells. (**A**) Time course effects of 20 μM CQ on replication stress marker pCHEK1-S345 and on autophagy marker LC3B in MiaPaca2 cells. (**B**) Dose response effects of 24 h CQ treatment on pCHEK1-S345 and LC3B in MiaPaca2 cells. (**C**) Effect of 20 μM CQ treatment for 24 h on pCHEK1-S345 and LC3B in a panel of PDAC cell lines. (**D**) Effects of 24 h treatment with lysosome inhibitors on pCHEK1-S345 and LC3B in MiaPaca2. (**E**) Measurements of S phase duration and G1 cells % by EdU pulse-chase flow cytometry analysis. MiaPaca2 cells were pulsed for 2 h with EdU followed by release into CQ media for 4 h (n=2) | All immunoblots are representative of at least 2 independent experiments. CQ: 20μM unless otherwise indicated; NH_4Cl: 10mM; BafA1: 10 nM; ** p<0.01, *** p<0.001.

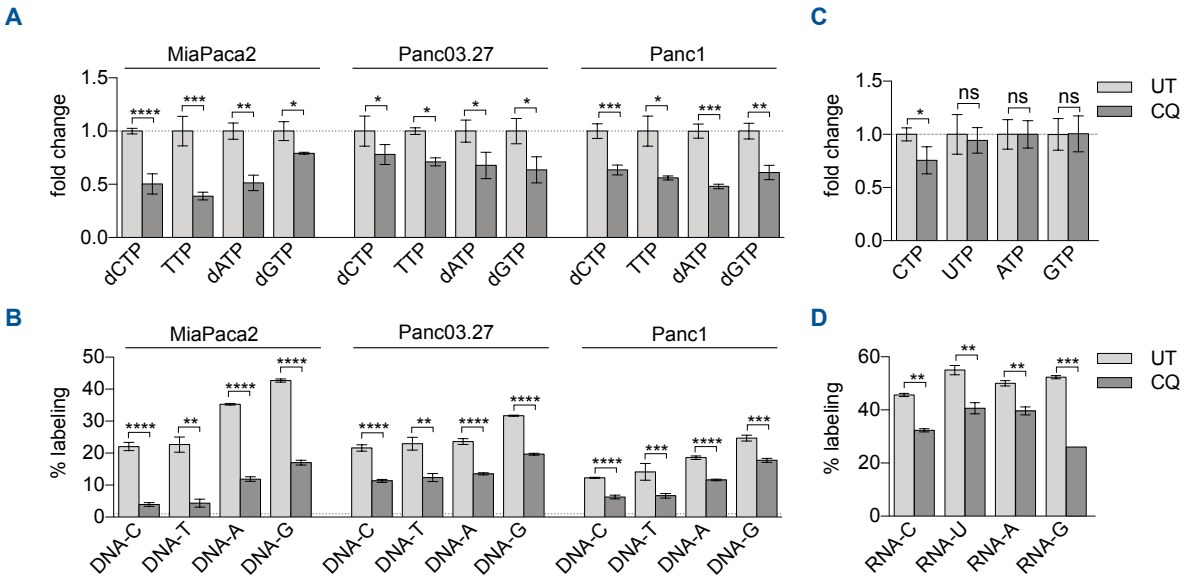

Fig. 2.3. CQ treatment impairs *de novo* nucleotide biosynthesis. LC-MS/MS-MRM analysis of: (**A**) relative levels of [$^{13}C_6$]glucose-labeled dNTPs and (**B**) % [$^{13}C_6$]glucose labeling of DNA in MiaPaca2, Panc.03.27, and Panc1 cells ± CQ (n=3); (**C**) Relative levels of [$^{13}C_6$]glucose-labeled NTPs and (**D**) % [$^{13}C_6$]glucose labeling of RNA in MiaPaca2 (n=3) | CQ: 20 μM; 24 h treatment; * p<0.05, ** p<0.01, *** p<0.001, **** p<0.0001.

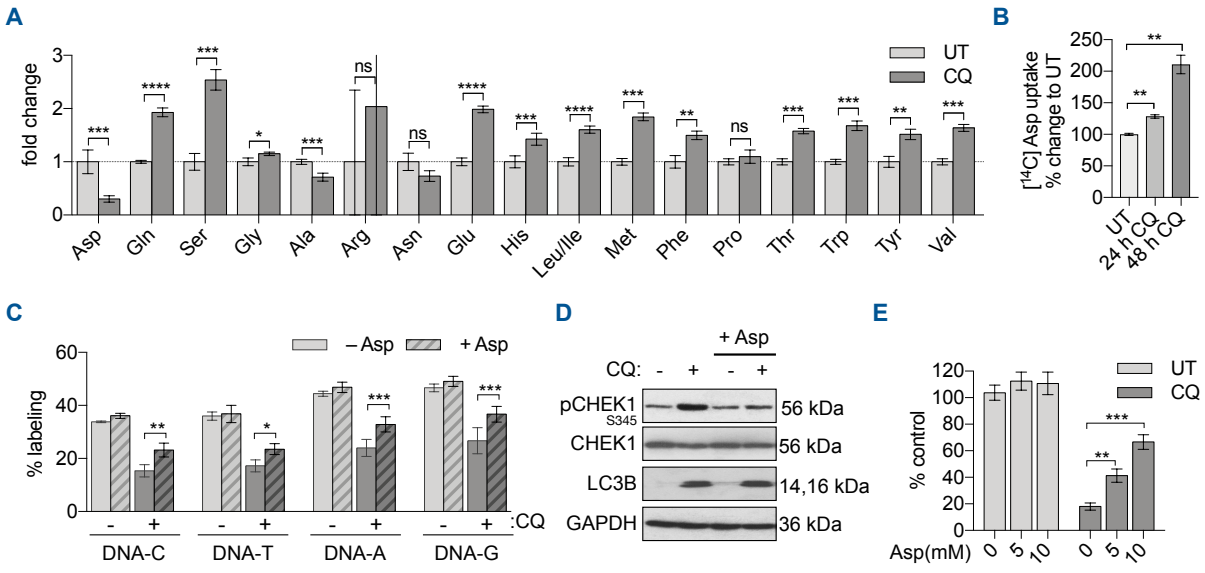

Fig. 2.4. Intracellular Asp depletion by CQ impairs *de novo* nucleotide biosynthesis, induces replication stress response, and inhibits PDAC cell proliferation. (**A**) Relative amino acid levels measured by LC-MS in MiaPaca2 cells ± CQ for 48 h (n=3). (**B**) CQ treatment for 24 h and 48 h increased [^{14}C]Asp uptake by MiaPaca2 cells. (**C**) [$^{13}C_6$]glucose-labeled DNA measured by LC-MS/MS-MRM in MiaPaca2 cells treated ± CQ ± Asp supplementation for 72 h (n=3). (**D**) pCHEK1-S345 and LC3B levels in MiaPaca2 cells ± CQ ± Asp supplementation for 24 h. (**E**) Viability of MiaPaca2 cells ± CQ ± Asp supplementation for 72 h (n=3) | CQ: 20μM; 24 h; Asp: 10 mM. * p<0.05, ** p<0.01, *** p<0.001, **** p<0.0001.

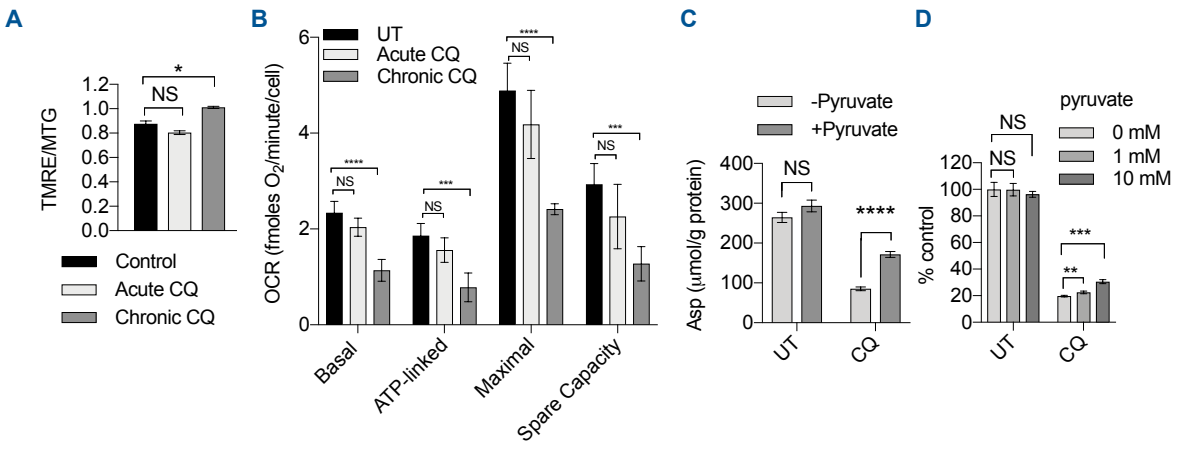

Fig. 2.5. CQ causes mitochondrial dysfunction. (**A**) Chronic CQ treatment induces mitochondrial membrane potential heterogeneity. Mitochondrial membrane potential in MiaPaca2 cells was measured after 2 h (acute) or 24 h (chronic) treatment with CQ. (**B**) Chronic CQ treatment reduced mitochondrial respiration. Mitochondrial respiration in MiaPaca2 cells was measured after 2 h (acute) or 24 h (chronic) treatment with CQ. (**C**) Pyruvate (1 mM) supplementation rescued CQ-induced Asp reduction in MiaPaca2 cells. (**D**) Pyruvate supplementation partially rescued CQ-induced proliferation inhibition in MiaPaca2 cells. | CQ: 20 μM. * p<0.05, ** p<0.01, *** p<0.001, **** p<0.0001. NS, not significant.

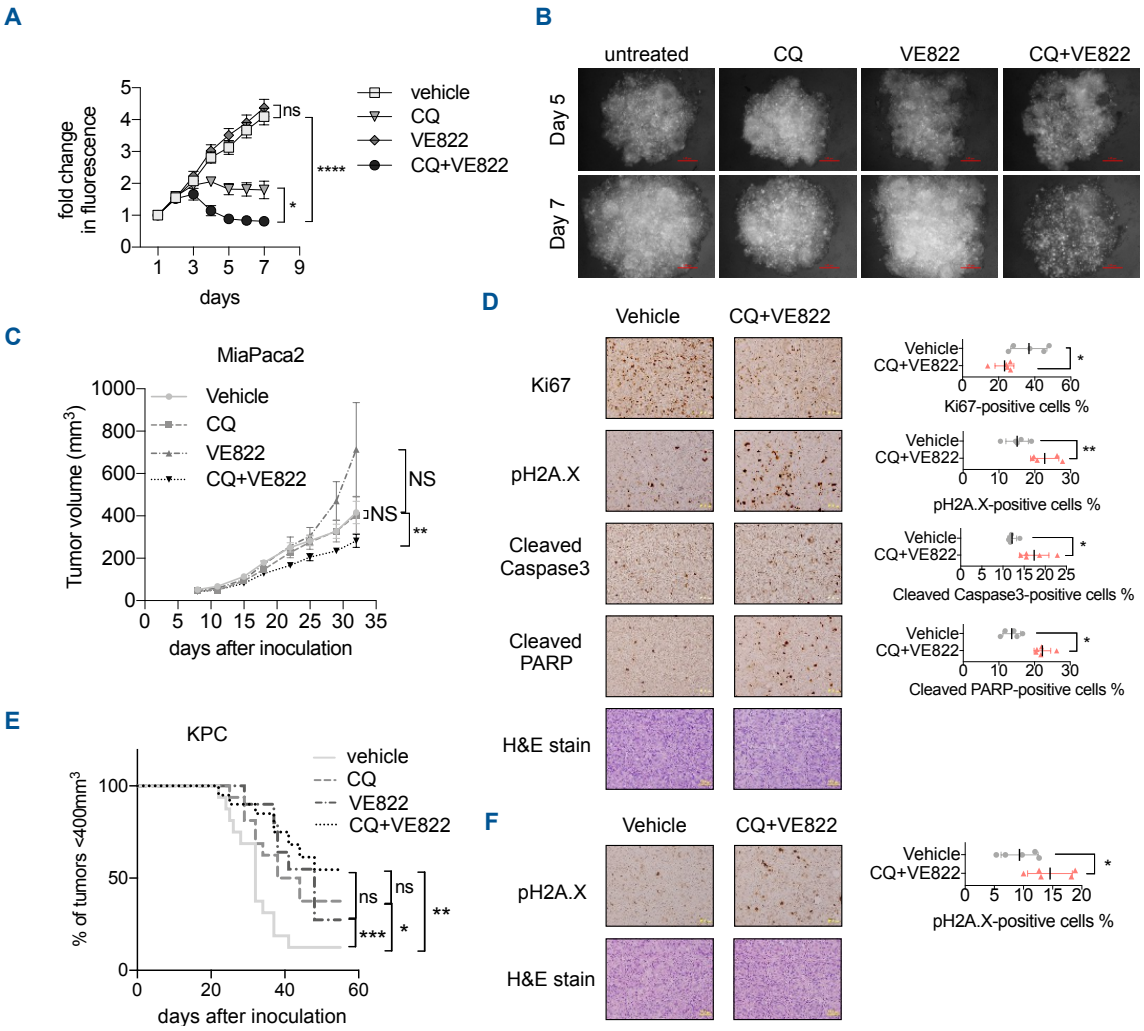

Fig. 2.6. CQ and replication stress response inhibitors synergistically inhibit tumor cell growth in organotypic *in vitro* and *in vivo* PDAC models. (**A**) Viability of MiaPaca2-GFP cells in CAF coculture ± CQ ± VE822 (n=3) (**B**) Representative fluorescence images of (**A**). (**C**) Xenograft MiaPaca2 tumor growth ± CQ ± VE822. (**D**) IHC staining of indicated markers in MiaPaca2 xenograft tumors after 5-day vehicle or CQ/VE-822 treatments. (**E**) Kaplan-Meier curves of tumors in syngeneic murine KPC mouse models ± CQ ± VE822. (**F**) IHC staining of pH2A.X in KPC syngeneic tumors with 5-day vehicle or CQ/VE-822 treatments. * p<0.05, ** p<0.01, *** p<0.001.

A

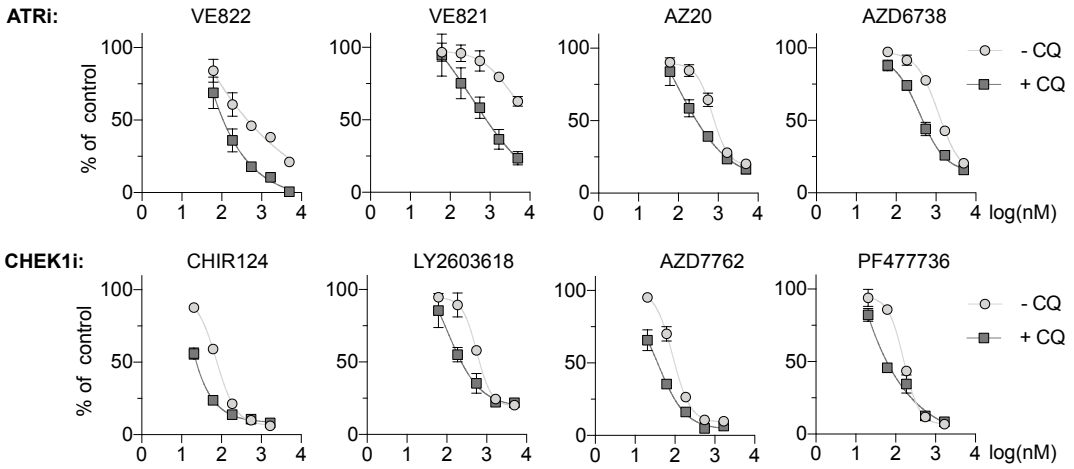

B

fa	0.5	0.75	0.9	0.95
CI (CQ & VE-822)	0.962	0.808	0.682	0.609

Fig. S2.1. Synergy between CQ and replication stress response inhibitors. (**A**) Viability of MiaPaca2 cells ± CQ ± indicated replication stress response inhibitors at 72 h. + CQ curves are normalized to CQ only treatment (n=3); CQ: 20μM. (**B**) Combination index (CI) between CQ and VE822 in inhibiting MiaPaca2 cell proliferation indicates synergy (CI < 1). CI was calculated at fraction affected (fa) of 0.5, 0.75, 0.9 and 0.95 using the Chou-Talalay method and Combosyn (www.combosyn.com). fa, fraction affected.

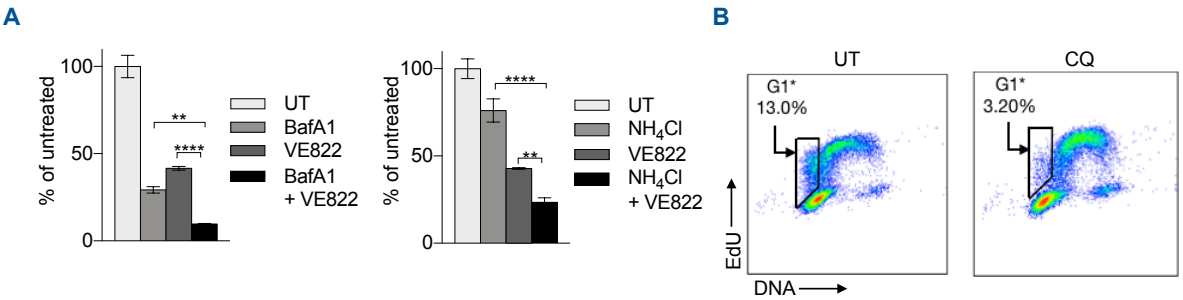

Fig. S2.2. Orthogonal assays confirm synergy between lysosome inhibition and replication stress response inhibitors and demonstrate CQ induces replication stress. (**A**) Viability of MiaPaca2 cells treated ± NH_4Cl or BafA1 ± VE822 for 72 h (n=3). (**B**) Flow cytometry plots of MiaPaca2 cells pulsed for 2 h with EdU followed by release into CQ media for 4 h (n=2). | NH_4Cl: 10 mM; BafA1: 10nM; CQ: 20 μM, ** p<0.01, **** p<0.0001.

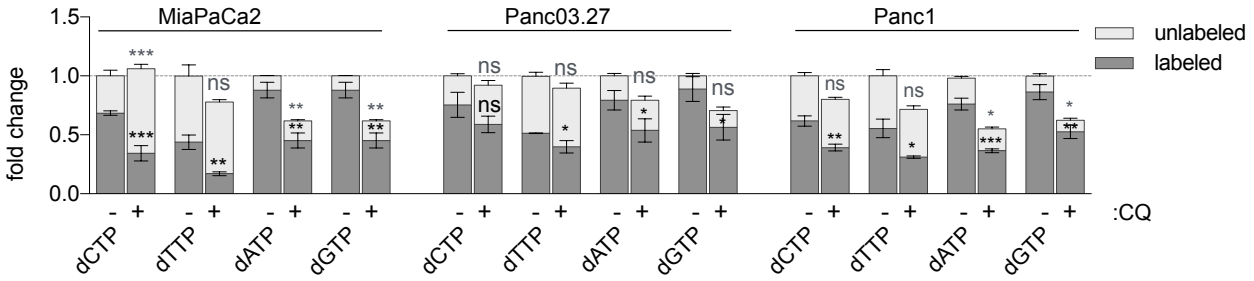

Fig. S2.3. CQ treatment impairs *de novo* nucleotide biosynthesis. LC-MS/MS-MRM analysis of relative levels of unlabeled and [$^{13}C_6$]glucose-labeled dNTPs in MiaPaca2, Panc. 03.27, and Panc1 cells ± CQ (n=3). Statistical significance was determined between -CQ and +CQ samples. | CQ: 20 μM; 24 h.

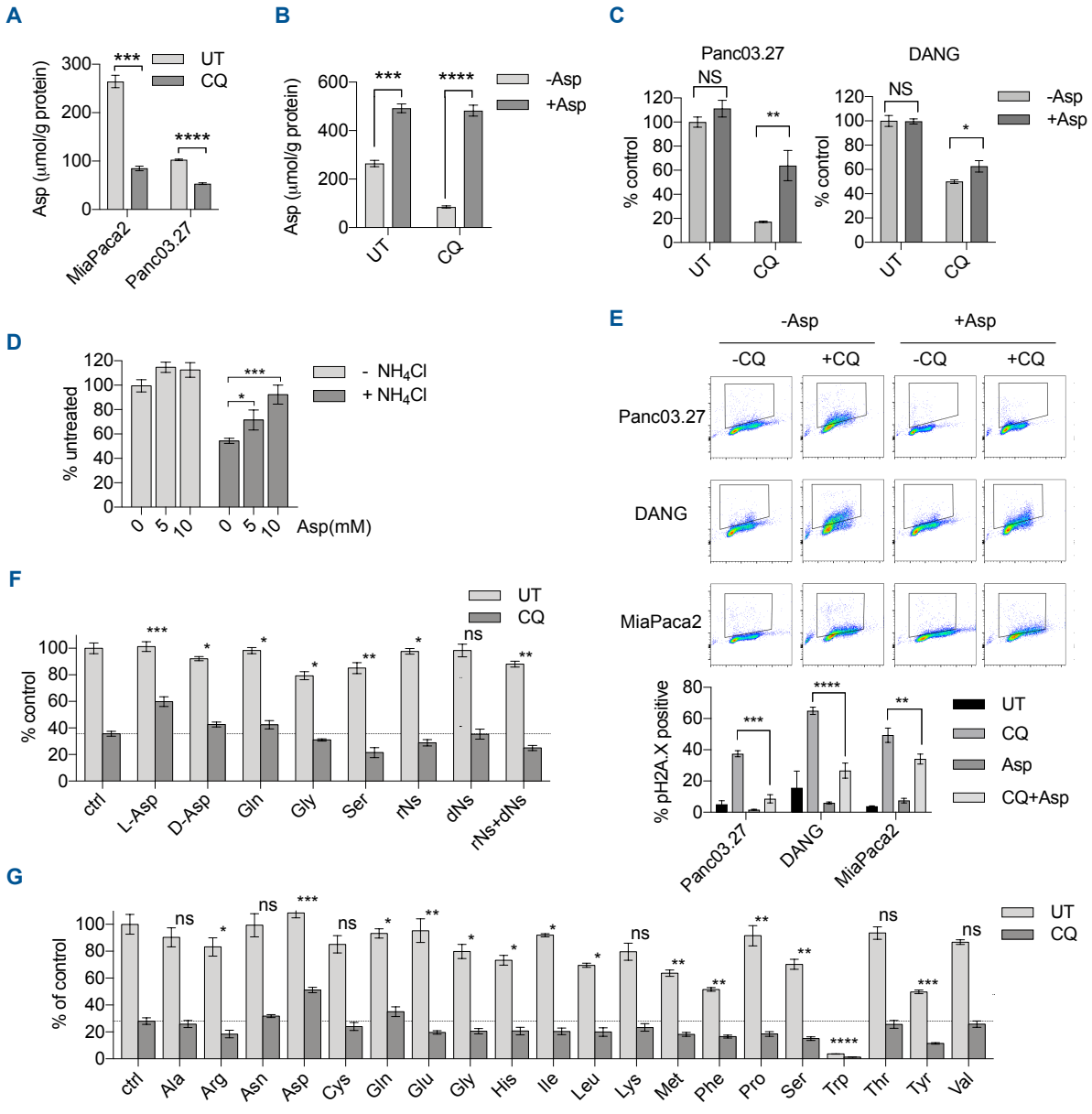
A
Asp (µmol/g protein)
UT
CQ
MiaPaca2
Panc03.27
B
Asp (µmol/g protein)
-Asp
+Asp
UT
CQ
C
Panc03.27
DANG
NS
% control
-Asp
+Asp
D
% untreated
- NH4Cl
+ NH4Cl
Asp(mM)
E
-Asp
+Asp
-CQ
+CQ
Panc03.27
DANG
MiaPaca2
% pH2A.X positive
UT
CQ
Asp
CQ+Asp
F
% control
UT
CQ
ctrl
L-Asp
D-Asp
Gln
Gly
Ser
rNs
dNs
rNs+dNs
G
% of control
UT
CQ
ctrl
Ala
Arg
Asn
Asp
Cys
Gln
Glu
Gly
His
Ile
Leu
Lys
Met
Phe
Pro
Ser
Trp
Thr
Tyr
Val

Fig. S2.4. CQ-induced proliferation inhibition and DNA damage in PDAC cells are rescued by Asp supplementation. (**A**) Cellular Asp levels in PDAC cells were reduced by CQ. (**B**) Asp supplementation rescued MiaPaca2 cellular Asp levels reduced by CQ. (**C**) Asp supplementation rescued PDAC cell proliferation. (**D**) Proliferation of MiaPaca2 cells inhibited by NH_4Cl was rescued by Asp supplementation. (**E**) pH2AX profiling indicating CQ-induced DNA damage in PDAC cells was rescued by Asp supplementation. (**F**) Effects of nucleotide substrate supplementations on CQ inhibited MiaPaca2 cell proliferation after 72 h treatment (n=3). (**G**) Effects of amino acid supplementations on CQ inhibited MiaPaca2 cell proliferation after 72 h treatment (n=3). | NH_4Cl: 10 mM; CQ: 20 μM; all amino acids: 10 mM; rNs: 30 μM rC, rU, rA, rG; dNs: 10 μM dC, dT, dA, dG. * $p<0.05$, ** $p<0.01$, *** $p<0.001$, **** $p<0.0001$.

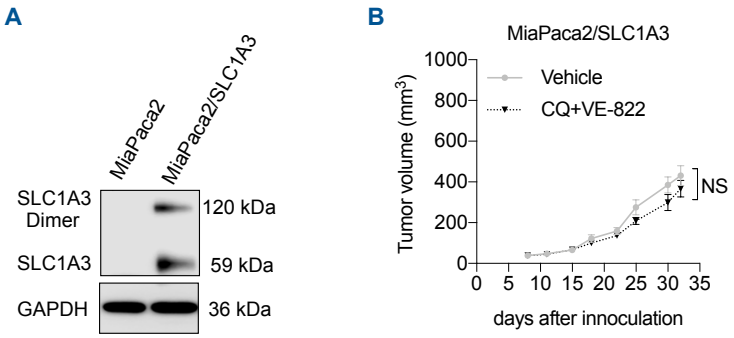

Fig. S2.5. Overexpression of Asp transporter SLC1A3 rescues xenograft MiaPaca2 tumor growth from the synergistic inhibition by CQ and VE822. (**A**) Overexpression of SLC1A3 in MiaPaca2 cells. (**B**) Overexpression of SLC1A3 rescued MiaPaca2 xenograft tumor growth with CQ/VE822 combination treatment. Treatment schedule is the same as described for Figure 6c. Both CQ and VE822 were given orally at 60 mg/kg.

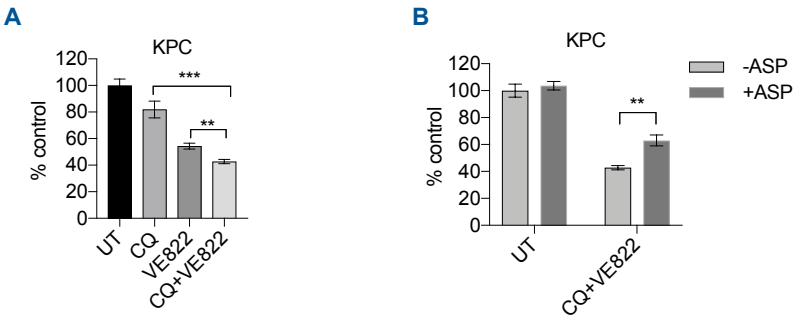

Fig. S2.6. CQ and VE822 synergistically impair murine PDAC cell growth *in vitro*. (**A**) Viability of murine PDAC KPC cells ± CQ ± VE822 for 72h (n=3). (**B**) Viability of KPC cells ± CQ/ VE822 ± aspartate supplementation for 72 h (n=3) | CQ: 20μM; VE822: 150 nM; ** p<0.01, *** p<0.001.

REFERENCES

1. Siegel RL, Miller KD, & Jemal A (2017) Cancer Statistics, 2017. *CA Cancer J Clin* 67(1): 7-30.
2. Provenzano PP*, et al.* (2012) Enzymatic targeting of the stroma ablates physical barriers to treatment of pancreatic ductal adenocarcinoma. *Cancer Cell* 21(3):418-429.
3. Perera RM*, et al.* (2015) Transcriptional control of autophagy-lysosome function drives pancreatic cancer metabolism. *Nature* 524(7565):361-365.
4. Yang S*, et al.* (2011) Pancreatic cancers require autophagy for tumor growth. *Genes Dev* 25(7):717-729.
5. Kamphorst JJ*, et al.* (2015) Human pancreatic cancer tumors are nutrient poor and tumor cells actively scavenge extracellular protein. *Cancer Res* 75(3):544-553.
6. Commisso C*, et al.* (2013) Macropinocytosis of protein is an amino acid supply route in Ras-transformed cells. *Nature* 497(7451):633-637.
7. Davidson SM & Vander Heiden MG (2017) Critical Functions of the Lysosome in Cancer Biology. *Annu Rev Pharmacol Toxicol* 57:481-507.
8. Rosenfeldt MT*, et al.* (2013) p53 status determines the role of autophagy in pancreatic tumour development. *Nature* 504(7479):296-300.
9. Mukubou H, Tsujimura T, Sasaki R, & Ku Y (2010) The role of autophagy in the treatment of pancreatic cancer with gemcitabine and ionizing radiation. *Int J Oncol* 37(4):821-828.
10. Donadelli M*, et al.* (2011) Gemcitabine/cannabinoid combination triggers autophagy in pancreatic cancer cells through a ROS-mediated mechanism. *Cell Death Dis* 2:e152.
11. Fu Z*, et al.* (2018) CQ sensitizes human pancreatic cancer cells to gemcitabine through the lysosomal apoptotic pathway via reactive oxygen species. *Mol Oncol* 12(4):529-544.
12. Fujii S*, et al.* (2008) Autophagy is activated in pancreatic cancer cells and correlates with poor patient outcome. *Cancer Sci* 99(9):1813-1819.

13. Strohecker AM & White E (2014) Autophagy promotes BrafV600E-driven lung tumorigenesis by preserving mitochondrial metabolism. *Autophagy* 10(2):384-385.

14. Guo JY*, et al.* (2016) Autophagy provides metabolic substrates to maintain energy charge and nucleotide pools in Ras-driven lung cancer cells. *Genes Dev* 30(15): 1704-1717.

15. Singh R*, et al.* (2009) Autophagy regulates lipid metabolism. *Nature* 458(7242): 1131-1135.

16. Hamer I, Van Beersel G, Arnould T, & Jadot M (2012) Lipids and lysosomes. *Curr Drug Metab* 13(10):1371-1387.

17. Kamphorst JJ*, et al.* (2013) Hypoxic and Ras-transformed cells support growth by scavenging unsaturated fatty acids from lysophospholipids. *Proc Natl Acad Sci U S A* 110(22):8882-8887.

18. Fujiwara Y, Wada K, & Kabuta T (2017) Lysosomal degradation of intracellular nucleic acids-multiple autophagic pathways. *J Biochem* 161(2):145-154.

19. Weber G*, et al.* (1991) Regulation of de novo and salvage pathways in chemotherapy. *Adv Enzyme Regul* 31:45-67.

20. Aird KM & Zhang R (2015) Nucleotide metabolism, oncogene-induced senescence and cancer. *Cancer Lett* 356(2 Pt A):204-210.

21. Nathanson DA*, et al.* (2014) Co-targeting of convergent nucleotide biosynthetic pathways for leukemia eradication. *J Exp Med* 211(3):473-486.

22. Laks DR*, et al.* (2016) Inhibition of Nucleotide Synthesis Targets Brain Tumor Stem Cells in a Subset of Glioblastoma. *Mol Cancer Ther* 15(6):1271-1278.

23. Le TM*, et al.* (2017) ATR inhibition facilitates targeting of leukemia dependence on convergent nucleotide biosynthetic pathways. *Nat Commun* 8(1):241.

24. Livesey KM, Tang D, Zeh HJ, & Lotze MT (2009) Autophagy inhibition in combination cancer treatment. *Curr Opin Investig Drugs* 10(12):1269-1279.

25. Piao S & Amaravadi RK (2016) Targeting the lysosome in cancer. *Ann N Y Acad Sci* 1371(1):45-54.

26. Wolpin BM*, et al.* (2014) Phase II and pharmacodynamic study of autophagy inhibition using hydroxychloroquine in patients with metastatic pancreatic adenocarcinoma. *Oncologist* 19(6):637-638.

27. Boone BA*, et al.* (2015) Safety and Biologic Response of Pre-operative Autophagy Inhibition in Combination with Gemcitabine in Patients with Pancreatic Adenocarcinoma. *Ann Surg Oncol* 22(13):4402-4410.

28. Fokas E*, et al.* (2012) Targeting ATR in vivo using the novel inhibitor VE-822 results in selective sensitization of pancreatic tumors to radiation. *Cell Death Dis* 3:e441.

29. Zeman MK & Cimprich KA (2014) Causes and consequences of replication stress. *Nat Cell Biol* 16(1):2-9.

30. Poli J*, et al.* (2012) dNTP pools determine fork progression and origin usage under replication stress. *EMBO J* 31(4):883-894.

31. Bester AC*, et al.* (2011) Nucleotide deficiency promotes genomic instability in early stages of cancer development. *Cell* 145(3):435-446.

32. Xu YZ, Huang P, & Plunkett W (1995) Functional compartmentation of dCTP pools. Preferential utilization of salvaged deoxycytidine for DNA repair in human lymphoblasts. *J Biol Chem* 270(2):631-637.

33. Hosios AM*, et al.* (2016) Amino Acids Rather than Glucose Account for the Majority of Cell Mass in Proliferating Mammalian Cells. *Dev Cell* 36(5):540-549.

34. Birsoy K*, et al.* (2015) An Essential Role of the Mitochondrial Electron Transport Chain in Cell Proliferation Is to Enable Aspartate Synthesis. *Cell* 162(3):540-551.

35. Leal AM, de Queiroz JD, de Medeiros SR, Lima TK, & Agnez-Lima LF (2015) Violacein induces cell death by triggering mitochondrial membrane hyperpolarization in vitro. *BMC Microbiol* 15:115.

36. Feig C*, et al.* (2012) The pancreas cancer microenvironment. *Clin Cancer Res* 18(16): 4266-4276.

37. Vonlaufen A*, et al.* (2008) Pancreatic stellate cells: partners in crime with pancreatic cancer cells. *Cancer Res* 68(7):2085-2093.

38. Toste PA*, et al.* (2016) Chemotherapy-Induced Inflammatory Gene Signature and Protumorigenic Phenotype in Pancreatic CAFs via Stress-Associated MAPK. *Mol Cancer Res* 14(5):437-447.

39. Garcia-Bermudez J*, et al.* (2018) Aspartate is a limiting metabolite for cancer cell proliferation under hypoxia and in tumours. *Nat Cell Biol* 20(7):775-781.

40. Raben N & Puertollano R (2016) TFEB and TFE3: Linking Lysosomes to Cellular Adaptation to Stress. *Annu Rev Cell Dev Biol* 32:255-278.

41. Zhang N*, et al.* (2018) Increased Amino Acid Uptake Supports Autophagy-Deficient Cell Survival upon Glutamine Deprivation. *Cell Rep* 23(10):3006-3020.

42. Son J*, et al.* (2013) Glutamine supports pancreatic cancer growth through a KRAS-regulated metabolic pathway. *Nature* 496(7443):101-105.

43. Abu-Remaileh M*, et al.* (2017) Lysosomal metabolomics reveals V-ATPase- and mTOR-dependent regulation of amino acid efflux from lysosomes. *Science* 358(6364):807-813.

44. Sullivan LB*, et al.* (2015) Supporting Aspartate Biosynthesis Is an Essential Function of Respiration in Proliferating Cells. *Cell* 162(3):552-563.

45. Redmann M*, et al.* (2017) Inhibition of autophagy with bafilomycin and chloroquine decreases mitochondrial quality and bioenergetic function in primary neurons. *Redox Biol* 11:73-81.

46. Xiao Y*, et al.* (2013) Identification of preferred chemotherapeutics for combining with a CHK1 inhibitor. *Mol Cancer Ther* 12(11):2285-2295.

47. Dobbelstein M & Sorensen CS (2015) Exploiting replicative stress to treat cancer. *Nat Rev Drug Discov* 14(6):405-423.

48. Zhang J, Dai Q, Park D, & Deng X (2016) Targeting DNA replication stress for cancer therapy. *Genes (Basel)* 7(8).

49. Massey AJ (2017) Modification of tumour cell metabolism modulates sensitivity to Chk1 inhibitor-induced DNA damage. *Sci Rep* 7:40778.

50. Liu EY*, et al.* (2015) Loss of autophagy causes a synthetic lethal deficiency in DNA repair. *Proc Natl Acad Sci U S A* 112(3):773-778.

51. Bachem MG*, et al.* (2005) Pancreatic carcinoma cells induce fibrosis by stimulating proliferation and matrix synthesis of stellate cells. *Gastroenterology* 128(4):907-921.

52. Kadera BE*, et al.* (2013) MicroRNA-21 in pancreatic ductal adenocarcinoma tumor-associated fibroblasts promotes metastasis. *PLoS One* 8(8):e71978.

53. Zhang JH, Chung TD, & Oldenburg KR (1999) A Simple Statistical Parameter for Use in Evaluation and Validation of High Throughput Screening Assays. *J Biomol Screen* 4(2): 67-73.

54. Xu S*, et al.* (2018) A precision therapeutic strategy for hexokinase 1-null, hexokinase 2-positive cancers. *Cancer Metab* 6:7.

55. Wikstrom JD*, et al.* (2007) beta-Cell mitochondria exhibit membrane potential heterogeneity that can be altered by stimulatory or toxic fuel levels. *Diabetes* 56(10): 2569-2578.

56. Krall AS, Xu S, Graeber TG, Braas D, & Christofk HR (2016) Asparagine promotes cancer cell proliferation through use as an amino acid exchange factor. *Nat Commun* 7:11457.

57. Cohen S*, et al.* (2009) Simultaneous analysis of eight nucleoside triphosphates in cell lines by liquid chromatography coupled with tandem mass spectrometry. *J Chromatogr B Analyt Technol Biomed Life Sci* 877(30):3831-3840.

CHAPTER 3

Identification of therapeutically actionable metabolic alterations induced by inhibition of mutant KRAS signaling in pancreatic cancer

ABSTRACT

Pancreatic ductal adenocarcinoma (PDAC) is an aggressive malignancy with an overall median survival of 12 months and five-year survival of less than 10%(1). Gradually increasing in incidence, it is now the third leading cause of cancer-related mortality in the United States and is expected to become second by 2020(2). Current systemic therapies only modestly benefit most patients. Meanwhile, clinical trials have consistently failed or only incrementally improved survival, underscoring an incomplete understanding of PDAC biology.

The most striking feature within the genetics of PDAC is a nearly universal (90-95%) gain-of-function mutation in KRAS(3, 4). Arising from an early stage of PDAC development, oncogenic KRAS mutations govern the biology of PDAC throughout the development and progression of the malignancy(5). Mutant KRAS orchestrates signaling and metabolic pathway alterations in PDAC to support its survival and growth, making it a very promising target for the treatment of mutant KRAS-driven cancers(6).

While a tremendous amount of effort has been spent towards pharmacologically blocking mutant KRAS, such efforts have been unsuccessful and as a result, oncogenic KRAS has been considered to be undruggable(7). However, recent development of KRAS G12C mutant-specific inhibitors has provided proof that mutant KRAS can indeed be directly targeted(8, 9).

In this chapter, using multiple models, we show that direct pharmacological targeting of KRAS G12C in PDAC cells gives rise to adaptive signaling mechanisms mediated by growth factor receptor signaling. Such adaptive processes lead to compensatory activation of oncogenic KRAS signaling. We also show that maximal and prolonged inhibition of oncogenic KRAS signaling is achieved by mutant KRAS-targeted combination therapy consisting of inhibitors of oncogenic KRAS G12C and growth factor receptor.

By implementing a comprehensive and integrated analytic platform that incorporates alterations in signaling pathways at phosphoproteome levels and in various metabolic pathways triggered by oncogenic KRAS-targeted combination therapy, we reveal that the treatment induces metabolic alterations that lead to oxidative stress and DNA damage. Such changes result in activation of the DNA damage response (DDR) signaling pathway. These findings are further leveraged by targeting the pathways that enable PDAC cells to deal with the metabolic and signaling stress triggered by combinatorial inhibition of oncogenic KRAS and growth factor receptor.

INTRODUCTION

Pancreatic ductal adenocarcinoma (PDAC) is genetically complex, with individual tumors harboring combinations of four high-frequency driver mutations (KRAS, CDKN2A, TP53 and SMAD4) and significantly greater numbers of heterogeneous mutations occurring at lower frequency(3). Most PDACs (90-95%) harbor oncogenic KRAS gain-of-function mutations, leading to hyper-activation of KRAS at all stages of disease progression(6). Mutant KRAS, the principal oncogenic driver in PDAC, plays critical roles in PDAC tumor initiation, growth and maintenance(10, 11). It has also been shown to mediate extensive signaling and metabolic adaptations which enable tumor cell survival and proliferation(10, 12, 13). Such addiction to mutant KRAS makes it a promising target for cancer therapy.

Since oncogenic KRAS significantly alters cancer cell metabolism, inhibiting metabolism using pharmacological approaches was proposed as an attractive way to target oncogenic KRAS-driven cancers(7). To suggest a new conceptual framework, we propose to call such chemical entities “modulators” of cancer metabolism rather than inhibitors, as the latter does not fully account for the various effects of pharmacological perturbation of cancer metabolism.

As an enzyme, KRAS is a GTPase that is involved in multiple signaling pathways, such as MAPK/ERK and PI3K/AKT pathways, as an upstream player. The conversion of KRAS from the inactive, GDP-bound form to its active, GTP-bound form is mediated by guanine nucleotide exchange factors (GEFs). The reverse reaction, the hydrolysis of KRAS-bound GTP, can occur in two ways, one mediated by GTPase-activating proteins (GAPs) and the other by intrinsic hydrolysis of GTP. In wild-type KRAS, GAP-mediated hydrolysis dominates the intrinsic hydrolysis. However, when oncogenic mutations are introduced, the GAP-mediated hydrolysis is severely impaired, resulting in hyperactivation of KRAS and its downstream oncogenic signaling pathways(14).

As a result of hyperactivation in KRAS signaling, mutant KRAS orchestrates multiple metabolic adaptations critical for PDAC growth and survival. Such alterations include changes in glucose, amino acid, lipid and energy metabolism to fulfill the increased anabolic demands of cancer cells(12, 13) and re-programming of cancer microenvironment to support tumors(15–18), although dependency on KRAS may vary under different molecular and cellular contexts(6, 19, 20). In further response to metabolic stress, KRAS-dependent PDAC growth and survival is also dependent upon recycling and scavenging of substrates through autophagy and macropinocytosis(21, 22).

A nearly universal gain-of-function oncogenic KRAS in PDAC, along with the aforementioned orchestration of PDAC metabolism induced by it, makes oncogenic KRAS an attractive therapeutic target for metabolic modulation in cancers. While intensive efforts to pharmacologically block mutant KRAS have been unsuccessful, recent groundbreaking work with allele-specific KRAS G12C inhibitors has reinvigorated hope for its direct and specific targeting(8, 9). Compared with other oncogenic KRAS mutants, G12C mutant retains higher intrinsic hydrolysis activity(14). Switch 2 pocket inhibitors such as ARS-1620 (Wellspring Biosciences) take advantage of this intrinsic hydrolysis by covalently engaging the GDP-bound state of KRAS G12C and irreversibly locking it in its inactive conformation(8).

ARS-1620 is well-tolerated in mice and is effective against human tumor xenografts harboring KRAS G12C(8). Ideally, ARS-1620 and drugs with similar specificity recently developed by Amgen (AMG 510), which has already entered phase 1 clinical trial, and Mirati Therapeutics (MRTX849), will prove to be clinically well-tolerated and effective against KRAS G12C-driven cancers. This would include 3% of PDAC, corresponding to over 1,000 new cases of PDAC/ year in the US alone for which currently there are no robust targeted therapies(7). Moreover, these compounds provide unique pharmacological tools to study the biology of mutant KRAS and identify targetable adaptive resistance mechanisms. This is critically important given that

previous work targeting MAPK pathway, the downstream effector of oncogenic KRAS, demonstrated that pharmacological inhibition of MAPK signaling results in alleviation of feedback inhibition and increased signaling from receptor tyrosine kinases (RTKs) such as growth factor receptors(23). If such feedback also occurs with direct inhibition of oncogenic KRAS, combination therapy will be necessary to enable maximal inhibition of the activity of KRAS signaling.

The development of inhibitors of oncogenic KRAS G12C, coupled with highly refined and precise methods and tools to measure and target cancer metabolism, provides an unprecedented opportunity to explore the interrelationships between metabolic and signaling alterations mediated by oncogenic KRAS. Given the critical roles of oncogenic KRAS signaling pathway in rewiring PDAC metabolism(24), it is highly likely that the direct inhibition of both oncogenic KRAS and the adaptive resistance mechanisms would have dramatic impacts on PDAC metabolism, which can be further leveraged. However, such impacts have not been precisely mapped. Therefore, it is largely unknown how such metabolic consequences could be further leveraged to better treat PDAC by rationally designing combinatorial therapeutic approaches.

In this chapter, using a pharmacological inhibitor of mutant KRAS and clinically relevant models of PDAC with KRAS G12C mutation, we employ a new approach to identify adaptive resistance mechanisms to direct inhibition of mutant KRAS that are predicted to occur based on our current understanding of this signaling pathway. This is then followed by comprehensive metabolic and phosphoproteomic analyses to reveal actionable metabolic vulnerabilities induced by direct targeting of mutant KRAS and adaptive resistance mechanisms. The work presented in this chapter provide a novel insight into the actionable metabolic alterations that are induced by the mutant KRAS-targeted combination therapy.

MATERIALS AND METHODS

Tissue culture

All tissue cultures were performed using DMEM (Corning, 10-017) supplemented with 10% fetal bovine serum (Omega scientific) unless otherwise noted. For three-dimensional, anchorage-independent tissue cultures, regular tissue culture dishes were coated with poly-HEMA (Sigma-Aldrich, P3932). Briefly, Poly-HEMA was dissolved at 20 mg/mL concentration in 95% Ethanol and then added to the plate to fully cover the growth area. Then the coating solution was dried overnight in tissue culture hood. The next day, the plates were sterilized by UV irradiation for two hours.

Generation of KRAS G12C PDAC cell culture models

MIAPACA2 cells were acquired from American Type Culture Collection (ATCC). XWR200 cell culture was derived from PDAC tumor samples that were surgically dissected by Dr. Timothy Donahue (UCLA). To identify PDAC tumors with G12C mutation in KRAS, PCR approach was employed. Briefly, Following pair PCR primers that is specific to G12C mutant was designed.

FWD: 5’ - GTAAGGCCTGCTGAAAATGACTG - 3’

REV: 5’ - ATGGTTCCCTAACACCCAGTT - 3’

Following the optimization of PCR condition, genomic DNA samples that were extracted from 60 human PDX specimens were screened for the presence of G12C mutant. After the identification of the presence of G12C KRAS by PCR, fibroblasts were removed by the combination of brief trypsinization (1 min) and 1 hr incubation on gelatin-coated surface. Following the derivation of pure PDAC tumor cultures of XWR200, whole-exome sequencing was performed to profile the mutational landscape of the tumor, by UCLA Technology Center for Genomics & Bioinformatics (UCLA TCGB).

To generate KP4662-G12C cells, KP4662 cells that were derived from a KP mouse (LSL-*Kras* G12D/+ ;LSL-*Trp53* R172H/+ ;*Pdx-1*-Cre) on a C57BL/6 background, were acquired (a gift from Dr. Robert Vonderheide, University of Pennsylvania). We inactivated endogenous *Kras* G12D in

these cells by transient transfection of lentiCRISPR.sgKras (Addgene 91894), while simultaneously introducing a murine *Kras* G12C transgene by lentiviral transduction. Following single cell dilution, the knockout of endogenous *Kras* G12D was screened by Sanger sequencing of PCR product of Kras G12D region followed by the sequencing data analysis using TIDE software (https://tide.nki.nl/). The inactivation was further confirmed by western blotting using Ras G12D-specific antibody (Cell Signaling Technology, 14429). The presence of *Kras* G12C was confirmed by western blotting using KRAS antibody (Santa Cruz Biotechnology, sc-30).

High-throughput screening of protein kinase inhibitor library

For the screening of a library of 430 kinase inhibitors, KRAS G12C PDAC cells were treated with seven-dose titration of kinase inhibitors in media containing vehicle or 1 μM ARS-1620. For MIAPACA2 cells, the screen was performed in monolayer culture for 72 hours. For XWR200 cells, the screen was performed in anchorage-independent culture for 120 hours. KP4662-G12C cells were cultured in anchorage-independent manner and were treated for 72 hour for the screening. Synergy scores for library compounds were calculated as the sum of Bliss additivity scores in combination with ARS-1620 across a 7-point concentration range and were added up to rank the compounds.

Western blotting

Western blotting was performed as previously described(25). Briefly, cells were harvested, washed and lysed in RIPA buffer containing 1x protease inhibitor cocktail and phosphatase inhibitor cocktail. Following the protein quantification using BCA assay (Thermo Scientific, 23225), equal amount of protein was prepared in the presence of 1x Lameli SDS-sample reducing buffer (Boston BioProducts, BP-110R) and was boiled. Following SDS-PAGE using NuPAGE™ 4-12% Bis-Tris Protein Gels (Invitrogen, NP0336), protein was transferred to nitrocellulose membrane (Thermo Scientific, 88018), blocked with blocking buffer containing 5%

skim milk and the incubated with the following primary antibodies, at 1:1000 dilution unless noted otherwise, overnight at 4 ºC.

•pERK (T202/Y204): Cell Signaling Technology, 4370

•ERK: Cell Signaling Technology, 4695

•pAKT (S473): Cell Signaling Technology, 4060

•AKT: Cell Signaling Technology, 9272

•Actin: Sigma-Aldrich, A2228

•Vinculin: Cell Signaling Technology, 13901

•pH2AX (S139): Cell Signaling Technology, 9718

•Cleaved PARP: Cell Signaling Technology, 5625

•pATM (S1981): Cell Signaling Technology, 5883

•pCHEK2 (T68): Cell Signaling Technology, 2197

•CHEK2: Cell Signaling Technology, 3440

HRP-conjugated anti-mouse (Cell Signaling Technology, 7076) and anti-rabbit (Cell Signaling Technology, 7074) secondary antibodies were used for the detection.

Non-targeted LC-MS metabolic measurements and analyses

For metabolic measurements, cells were treated starting at 400,000 cells/mL density. After perturbation, 1 - 1.5 x 10^6 cells were collected. Cells were then washed with room temperature 150 mM ammonium acetate twice before adding 1 mL of ice-cold 80% methanol containing ^{15}N-labeled internal standards. After vigorous vortexing, samples were centrifuged at 21000 g for 10 min at 4ºC. The supernatant was transferred to a 1.5 mL Eppendorf tube and the metabolites were dried under vacuum. Protein pellets were stored at -80ºC for protein quantification for data normalization. Following vacuum drying, metabolites were resuspended in Milli-Q™ LC-MS grade ultra pure water to achieve a 5µL injection of 200,000 cells and 5 µL of this solution is injected for the mass spectrometer-based analysis. The analysis was performed on a LTQ Orbitrap XL (Thermo Scientific) in both positive and negative modes with positive voltage 4.0 kV

and negative voltage 4.0 kV. The mass spectrometer was coupled to an Agilent 1260 Infinity Quaternary LC (Agilent) HPLC system. Mobile phase A was 20 mM ammonium hydroxide (NH_4OH), 20mM Ammonium Bicarbonate (NH_5CO_3) pH 9.0, mobile phase B was acetonitrile and the separation achieved on an Acquity UPLC BEH Amide 1.7µm column (150 × 3.0 mm, Waters). The flow was 300 µL/min, and the gradient ran from 15% A to 80% A in 15 min, followed by a 1 min gradient from 85% A to 15% A and an isocratic re-equilibration for 7 min. Metabolites were detected and quantified as area under the curve based on retention time and accurate mass (≤ 3 p.p.m.) using El Maven peak selection software (Elucidata). Relative amounts of metabolites between various conditions, as well as percentage of [$^{13}C_6$]glucose labelling, were calculated and corrected for naturally occurring ^{13}C abundance. The LC-MS data are analyzed by El-Maven, in collaboration with Elucidata (New Dehli, India and Cambridge, Massachusetts).

nLC-MS/MS proteomic and phosphoproteomic measurements and data analyses

This procedure is described in following six sections (A - F).

A. Protein extraction, digestion, labeling and pooling

Anchorage-independent PDAC cells were washed twice with 10 ml ice cold PBS and lysed in fresh lysis buffer (50 mM triethylammonium bicarbonate, pH 8.5, 0.5% sodium deoxycholate, 12 mM sodium lauroyl sarcosine, protease inhibitor cocktail (Sigma) and phosphatase inhibitor cocktail containing 10 mM sodium pyrophosphate, 50 mM sodium fluoride, 1 mM sodium orthovanadate, and 50 mM beta-glycerophosphate). Protein lysates were sonicated for 10 min, 30 s on 30 s off, at 4°C using Bioruptor Pico (Diagenode) followed by heating at 95°C for 5 min. The protein concentration of lysates were quantified by the BCA protein assay (Thermo Fisher Scientific) and 1 mg total protein from each sample was carried through the rest of the sample preparation. Protein disulfides were reduced with 5 mM dithiolthreitol (final concentration) for 30 min at 37°C followed by alkylation with 10 mM chloroacetamide (final concentration) for 30 min

at room temperature in the dark. Excess alkylating agent was quenched by adding the same amount of dithioltheritol as the previous step and incubating for 5 min at room temperature. Each sample was then diluted 1:5 using 50 mM triethylammonium bicarbonate, pH 8.5, containing 10 µg trypsin (Promega) and digested at 37◦C for 4 h. A second aliquot of 10 µg trypsin (Promega) was spiked into the samples and digested overnight at 37◦C. The reaction was quenched and detergents extracted with 1:1 (v:v) ethyl acetate containing 1% trifluoroacetic acid. The samples were vortexed vigorously and centrifuged at 16,000x*g* for 5 min. The lower aqueous phase was transferred to new microcentrifuge tubes and dried by speedvac. The samples were reconstituted in 2% acetonitrile with 0.1% trifluoroacetic acid, desalted on Oasis HLB 10 mg cartridges (Waters), and dried by speedvac. Samples were resuspended in 200 mM EPPS, pH 8.5, and peptide concentration was obtained using Pierce Quantitative Colorimetric Peptide Assay. 400 µg of peptides were labeled with 11-plex TMT reagents at 1:2 reagent:peptide concentration following the manufacturer's instruction, and dried by speedvac. Samples were reconstituted in 2% acetonitrile with 0.1% trifluoroacetic acid and 1 µg of total peptides from each sample were pooled and desalted using SDB StageTips as previously described (Rappsilber et al., 2007). 1 µg of total peptide from this pooled test sample was acquired via nanoLC-MS/MS on a QExactive Plus (Thermo) using a 3h gradient as later discussed. The raw data was processed using Proteome Discoverer v2.2 (Thermo) as later discussed. Each sample was normalized to the protein median fold change compared to the 126 m/z TMT channel and ~300 µg of each sample was pooled accordingly. The pooled peptide sample was desalted on an Oasis HLB 200 mg cartridge (Waters) and dried by speedvac.

B. Phosphopeptide enrichment by immobilized metal affinity chromatography

Phosphopeptide enrichment was performed using Fe-IMAC as previously described (Swaney and Villen, 2016). Briefly, 3.3 mg of dried peptides were solubilized in 900 µl of phosphopeptide binding solution (80% acetonitrile and 0.1% TFA). 150 µL peptide aliquots were mixed with 165

µL of Fe-IMAC and incubated at room temperature for 30 min with shaking. The supernatant and all washes were collected, dried by speedvac, and desalted on an Oasis HLB 200 mg cartridge (Waters) to be later used for peptide fractionation and total protein quantification via nanoLC-MS/MS. The phosphopeptides were quickly eluted from beads with 100 µL of phosphopeptide elution solution (70% acetonitrile and 1% ammonium hydroxide), passed through C8 StageTip and acidified with 30 µL of 10% formic acid. The phosphopeptide eluents were dried by speedvac and desalted using SDB StageTips.

C. Offline basic pH reverse phase liquid chromatography

The total phosphopeptide-enriched sample and 70 µg of the non-phosphopeptide sample were each solubilized in 3 µL of buffer A (10 mM ammonium bicarbonate, pH 10, and 2% acetonitrile) and separated on a Zorbax 300Extend-C18 column (3.5 µm particle size, 0.3 mm × 150 mm, Agilent) using an Agilent 1260 capillary pump and µWPS autosampler equipped with an 8 µL sample loop. 96 fractions were collected with a 60 min gradient from 5% to 60% buffer B (90% acetonitrile, 10 mM ammonium bicarbonate, pH 10, flow rate of 6 µl/min) into pre-deposited 20 µL of 5% formic acid. The samples were concatenated with an interval of 24 to form 24 final fractions (e.g. fractions 1, 25, 49, and 73 combined, fractions 2, 26, 50 and 74 combined, and so on). The concatenated fractions were desalted using SDB StageTips and dried by speedvac.

D. Acidic pH reverse phase liquid chromatography coupled with tandem MS

The dried peptide fractions for whole proteome analysis were reconstituted in 11 µL of 2% acetonitrile and 0.15% formic acid. For phosphopeptide analysis, the dried peptide fractions were reconstituted in 6 uL of 2% acetonitrile and 0.15% formic acid. 5 µL of sample was loaded on a laser-pulled reverse phase column (150 μm × 20 cm, 1.8 µm C18 resin with 0.5 cm of 5 µm C4 resin at the laser-pulled end (Acutech Scientific (San Diego, CA))) interfaced with an

Eksigent 2D nanoLC, Phoenix S&T dual column source, and QExactive Plus MS (Thermo). Peptides were eluted using 5-40% buffer B gradient in 3h (buffer A: 2% acetonitrile, 0.15% formic acid; buffer B: 98% acetonitrile, 0.15% formic acid, flow rate of 0.5 µl/min). The column was heated at 60°C by a butterfly portfolio heater (Phoenix S&T) to reduce backpressure. The mass spectrometer was operated in data-dependent mode with a survey scan from 350-1500 m/z (70,000 resolution, 3×10^6 AGC target and 100 ms maximal ion time) and 10 MS/MS scans with starting fixed m/z of 100 (35,000 resolution, 2×10^5 AGC target, 120 ms maximal ion time, 32 normalized collision energy, 1.2 m/z isolation window, and 30 s dynamic exclusion).

E. Identification and quantitation of peptides using Proteome Discoverer v 2.2

The acquired MS/MS raw files were searched by the Sequest algorithm against a forward and reverse target/decoy database to estimate FDR. The target protein database was downloaded from the Uniprot human database (reference and additional sequences, 93,320 protein entries; downloaded in March 2018) and the decoy protein database was generated by reversing all target protein sequences. A contaminate protein database was included in the searches (244 protein entries; downloaded from MaxQuant 1.6.0.16). Spectra were searched with ± 10 ppm for precursor ion and ± 0.02 Da product ion mass tolerance, fully tryptic restriction, static mass shift for TMT-tagged N-terminus and lysine (+229.16293), carbamidomethylation to cysteine (+57.021), dynamic mass shift for oxidation of methionine (+15.995), deamidation of asparagine and glutamine (+0.984), acetylation of protein N-terminus (+42.011), phosphorylation of serine, threonine and tyrosine (+79.96633, only for phosphopeptide-enriched fractions), two maximal missed cleavages, three maximal modification sites, and the assignment of b and y ions. Putative peptide spectra matches were filtered by Percolator using 1% FDR. Post-translational modifications were site localized using ptmRS. TMT reporter ions were quantified using the most confident centroid with reporter ion mass tolerance at 20 ppm.

F. Differential expression analysis of proteome and phosphoproteome

Differential expression events were defined by identifying proteins/phosphopeptides with between-treatment variance significantly larger than within-replicate variance using one-way ANOVA (analysis of variance). Significantly altered proteins/phosphopeptides were filtered using Benjamini-Hochberg (BH) procedure at 1% FDR. All statistical analysis, principle component analysis, and unsupervised hierarchical clustering was performed using Python. Kinase-substrate enrichment analysis (KSEA) was performed using the web tool (https://casecpb.shinyapps.io/ksea/). Briefly, the significantly-altered phosphopeptides were submitted and respective kinases were assigned using the PhosphositePlus database and NetworKin. Kinases were filtered with 5% FDR.

Measurement of glucose consumption, lactate production and glutamine consumption

Media metabolite measurement was performed as previously described(26). Briefly, 1 mL media was collected before and after the treatment. Collected media was once again centrifuged at 4ºC to remove debris. The medium was analyzed for glucose, lactate, and glutamine concentrations using a Biomedical Bioprofile Analyzer (Nova Biomedical). Medium that was not incubated with the cells was used as a blank control. Values were normalized to cell count and the length of the perturbation.

Flow cytometry measurement of PD-L1 expression

To measure the expression of PD-L1, KP4662-G12C C547BL/6 syngeneic PDAC cells were plated at 0.2 x 10^6 cells/mL density. Following 48 hour incubation of indicated perturbations, cells were collected and centrifuged (450 g, 4 minutes, 4 ºC). Cells were then washed twice with FACS buffer (PBS with 1 % FBS). For the staining of PD-L1, cells were resuspended in FACS buffer containing 1:200 dilution of PD-L1 antibody (BioLegend, 124037) and were incubated a for 20 minutes at at room temperature in dark. The data was acquired using LSR II cytometer (BD Biosciences) and was analyzed by FlowJo software (Tree Star).

RESULTS

Clinically relevant models of KRAS G12C PDAC

To identify adaptive resistance mechanisms to direct inhibition of oncogenic G12C KRAS in PDAC and to map the metabolic alterations induced by the inhibition of oncogenic KRAS and its adaptive resistance mechanisms, we have employed a panel of seven human and murine KRAS G12C PDAC models (**Fig. 3.1A**). Our panel includes a PDAC cell line (MIAPACA2), two patient-derived xenograft (PDX) models (E25Y90 and J29M573) obtained from the NCI Patient-Derived Models Repository (PDMR), and a new PDX model (XWR200) identified by KRAS mutational profiling of 60 PDAC surgically resected by Dr. Timothy Donahue at UCLA. XWR200 is derived from a 58-year-old male with poorly differentiated PDAC (pT3, pN1, pM0). Whole exome sequencing of our primary human KRAS G12C models confirms they are representative of the genetic diversity of KRAS G12C PDAC samples in the TCGA database 12 (**Fig. 3.1B**). XWR200, E25Y90 and J29M573 can be propagated in NSG mice (**Fig. 3.1C and data not shown**).

In addition to cell line and PDX models, to enable pharmacological inhibition of mutant KRAS in immunocompetent models, we have generated a KRAS G12C murine model. To do this, we used KP4662 cells that are derived from a KP mouse (LSL-*Kras* G12D/+ ;LSL-*Trp53* R172H/+ ;*Pdx-1*-Cre) on a C57BL/6 background, a generous gift from Dr. Robert Vonderheide (University of Pennsylvania). We then inactivated endogenous *Kras* G12D in these cells by CRISPR/Cas9 and simultaneously introduced a murine *Kras* G12C transgene (**Fig. 3.1D**). The new Kras G12C KP cells were rendered sensitive to ARS-1620 (**Fig. 3.1E**).

Identification of adaptive resistance mechanisms to direct inhibition of oncogenic KRAS G12C

Prior studies using drugs to target the MAPK pathway suggest that direct mutant KRAS inhibition may relieve upstream feedback and increase signaling from growth factor receptors(27, 28). If such resistance mechanisms occur, combination therapies will be

necessary to study how the impact of mutant KRAS inhibition on pyrimidine metabolism. We therefore performed a high-throughput (HT) chemical genomics screen in which a library of 430 kinase inhibitors was tested in combination with ARS-1620 in the three G12C KRAS PDAC models. The models include MIAPACA2, a PDAC cell line with mesenchymal background(29), XWR200, a human PDAC PDX model with epithelial background (data not shown) and KP4662-G12C, a C57BL/6 syngeneic murine PDAC with epithelial background (data not shown). Interactions between ARS-1620 and library compounds were quantified by calculating the sum of Bliss excess over additivity scores across the dose response range for each compound (**Fig. 3.2A**). Radar plot was employed to display the impact of combination of each kinase inhibitor with ARS-1620 (**Fig. 3.2B**). In all three models, receptor tyrosine kinase (RTK) inhibitors comprised most of the compounds that potentiated the antiproliferative effects of ARS-1620 (**Fig. 3.2C**). This finding is consistent with previous reports in KRAS mutant lung cancer cells showing EGFR inhibition increased the engagement with KRAS G12C of ARS-853, an earlier version of ARS-1620 15, 49 . Notably, FGFR mediated the adaptive resistance in the mesenchymal model (MIAPACA2) and while it was mediated by EGFR in epithelial models (XWR200 and KP4662-G12C), which is consistent with findings from KRAS mutant lung cancers(30). Collectively, our data support a role for RTK-mediated guanine nucleotide exchange factor (GEF) activity in KRAS G12C activation(9, 31, 32). In our subsequent studies in MIAPACA2, we focused on AZD4547, an FGFR inhibitor currently in clinical trials, which showed one of the highest synergies in our screen (**Fig. 3.2C**). Erlotinib, an EGFR inhibitor that is FDA-approved for PDAC treatment, was used for XWR200 and KP4662-G12C. Combination of ARS-1620 and AZD4547 or Erlotinib resulted in a more pronounced inhibition of MAPK signaling pathway, as evidenced by phosphorylation status of ERK (**Fig. 3.3**),

Metabolomic analyses reveal the alterations underlying the responses of PDAC cells to the inhibition KRAS G12C and the adaptive resistance mechanisms

After establishing the growth factor receptors mediate adaptive resistance to the direct inhibition of oncogenic KRAS G12C, we set out to profile the alterations in the PDAC metabolism in order to understand the mechanistic basis of the phenotypic alterations in KRAS G12C PDAC. We observed a dynamic alterations in mutant KRAS signaling following 0 to 120 hours of 1 μM ARS-1620 and 0.3 μM Erlotinib treatment in XWR200 cells (**Fig. 3.4A**), suggesting the PDAC metabolism will dynamically modulated by by signaling alterations. To address this, we have performed a time-course LC-MS metabolomics experiment using XWR200 cells. Briefly, XWR200 cells were treated with ARS-1620 and Erlotinib. Cells were collected 0, 6, 24, 72 and 120 hours after the treatment for metabolomic analyses (**Fig. 3.4B**).

One of the most striking metabolic changes was observed in the glutathione (GSH) biosynthesis pathway (**Fig. 3.4C**). Intriguingly, we have observed an increase in the level of S-adenosyl-methionine (SAM) while the downstream metabolite, S-adenosyl-homocysteine (SAH), was depleted starting from 24 h following the treatment. This data indicates that a metabolic block is induced at this step by the inhibition of oncogenic KRAS and the adaptive resistance mechanism (**Fig. 3.4C**). In addition to the generation of SAH, the metabolic outcome of this reaction, which is mediated by various methyl transferase enzymes, is the generation of methyl group that can are involved in multiple biological process including chromatin remodeling for DNA damage repair and pyrimidine and purine nucleotide biosynthesis(33, 34). Furthermore, the block in SAM to SAH conversion resulted in depletion of downstream metabolites in GSH biosynthesis pathway including GSH itself, an important cellular antioxidant (**Fig. 3.4C**).

Induction of DNA damage response pathway following the inhibition of KRAS G12C and the adaptive resistance mechanisms in KRAS G12C PDAC models

We hypothesized that the depletion of methyl group donor that is required for chromatin remodeling to during DNA repair would make the cells less capable of repairing DNA damage. We further hypothesized that the depletion of GSH would render cells more vulnerable to ROS-

induced DNA damage. Therefore, we have performed the immunoblot analysis in KRAS G12C models treated ± ARS-1620 ± the inhibitor of adaptive resistance mechanism to monitor the status of DNA damage response pathway activation. Interestingly, in all three models of KRAS G12C, an increased level of pH2AX (S139), a marker of DNA double strand break (DSB), was observed following combined inhibition of KRAS G12C and FGFR (MIAPACA2, **Fig. 3.5A**) or EGFR (XWR200 and KP4662-G12C, **Fig. 3.5B and C, respectively**). Accordingly, phosphorylation of ATM at S1981, and of CHEK2 at T68, both of which are the marker of DNA damage response (DDR) pathway activation, were increased in MIAPACA2 and XWR200 cells (**Fig. 3.5A and B**). These proteins are not detected in KP4662-G12C, likely due to species specificity of the antibodies (**Fig. 3.5C**). Finally, in concordance with the increase in DNA damage, a higher level of apoptosis was observed following the combination (**Fig. 3.5A and B**).

The activation of DDR pathway was further confirmed in an unbiased way by monitoring the activities of protein kinases at the phosphoproteome level. The Kinase Substrate Enrichment Analysis (KSEA) following 24 hours of 1 μM ARS-1620 and 1 μM AZD4547 treatment in MIAPACA2 cells demonstrates that ATM and CHEK2 are among the kinase that are most upregulated following the treatment (**Fig. 3.5D**). To summarize, combined inhibition of KRAS G12C and growth factor receptor, which is responsible for the adaptive resistance, leads to 1) impaired chromatin remodeling and 2) imparted nucleotide biosynthesis due to the depletion in methyl donor, and to 3) impaired GSH biosynthesis. The metabolic output of these alterations is the decreased capacity to mitigate DNA damage. As a result, DNA damage response is activated (**Fig. 3.6**).

DISCUSSION

In this chapter, using multiple PDAC models that harbor G12C mutation in KRAS, we show that the resistance to the direct inhibition of oncogenic KRAS signaling is mediated by growth factor receptor signaling. This is consistent with previous findings using the downstream inhibitors of KRAS signaling pathway(27, 28). The findings demonstrate that combinatorial approaches would be required to maximize the therapeutic potential of G12C mutant-specific direct inhibitor of KRAS.

By profiling metabolic alterations induced by mutant KRAS-targeted combination therapy, we reveal a surprising connection between oncogenic KRAS signaling and SAM metabolism. Such connections have not previously been made to the best of our knowledge. A metabolic block in the conversion from SAM to SAH is induced by the mutant KRAS-targeted combination therapy, resulting in a series of metabolic alterations, all of which have connections to DNA damage. Accordingly, our findings from targeted and non-targeted profiling of the signaling alterations show that DNA damage response pathway is highly upregulated.

Future directions include leveraging the vulnerabilities revealed by metabolic alterations following the inhibition of oncogenic KRAS and growth factor receptor signaling. We hypothesize that the induction of oxidative stress and DNA damage by mutant KRAS-targeted therapy would sensitize PDAC cells to oxidative stress inducers and sensitizers. Considering the block in methyltransferase activities, it would be fascinating to explore potential epigenetic alterations, due to impaired DNA and/or histone methylation, induced by mutant KRAS targeted therapy.

Further studies would concern the crosstalk between multiple cell types that consist of PDAC microenvironment. One of the striking features of PDAC is the presence of dense stroma(17, 35, 36). Growing evidence indicates that stromal cells impact the metabolism of cancer cells by

secreting metabolites and cytokines which in turn affect the metabolism of tumor cells(17, 37, 38). The impacts of stromal cells, more specifically, cancer-associated fibroblasts (CAFs), on the impact of mutant KRAS-targeted therapy will be further investigated.

The ongoing studies also include the validation of the combination of ARS-1620 and growth factor receptor inhibitors *in vivo* using both immunodeficient and immunocompetent mouse models. The studies in immunocompetent C57BL/6 mice will be conducted using KRAS G12C C57BL/6 syngeneic model that we have developed (**Fig. 3.1D and E**). The syngeneic model will be further utilized to test the combination of oncogenic KRAS-targeted therapy and immunotherapy. Recent findings indicate that, in PDAC, immunosuppressive myeloid cells in the microenvironment has to be suppressed, to make activation of tumor infiltrating CD8 lymphocytes (TILs) by anti-PD-1 antibodies more efficacioius(39). Reports of durable responses in a subset of heavily pretreated PDAC patients in a multi-center Phase Ia/Ib trial (NCT02526017) of Cabiralizumab (anti-CSF1R) combined with Nivolumab (anti-PD1) performed by a group at UCLA led by Dr. Zev Wainberg, provide an unprecedented opportunity to treat PDAC with parallel targeting of cancer signaling, metabolism and microenvironment (**Fig. 3.7**). Our preliminary data also indicate that the consumption of glucose and glutamine, two critical metabolites that cancer cells and TILs compete with, significantly decrease following co-inhibition of mutant KRAS and RTK (**Fig. 3.8**). Given that KRAS G12C-specific inhibitors, unlike the inhibitors of downstream MAPK effectors, would specifically target PDAC cells, it is highly possible that the metabolic microenvironment would be more favorable to TILs.

FIGURES

A

KRAS G12C PDAC

ID	Type
MIAPACA2	Cell line
E52Y90	Primary
J29M573	Primary
XWR200	Primary
G12C KP	GEMM

B

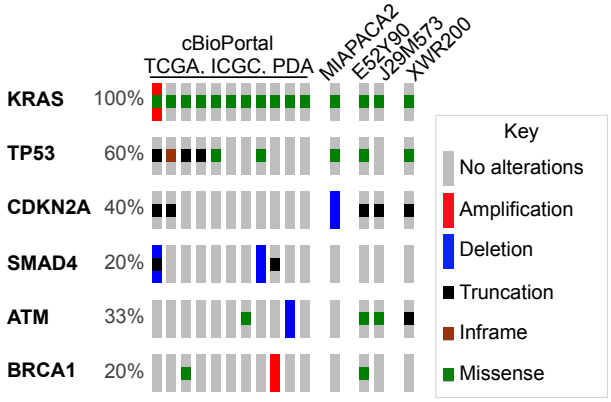

C

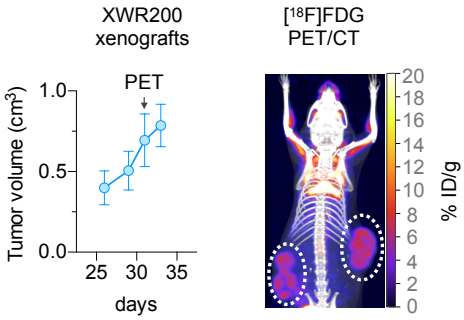

D

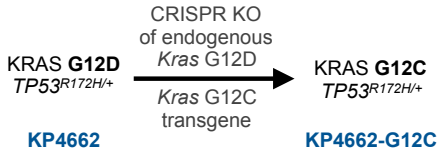

E

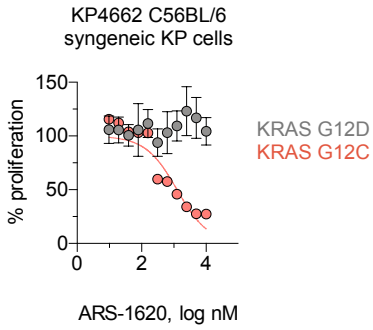

Fig. 3.1. KRAS G12C PDAC models. (**A**) Panel of KRAS G12C PDAC models consisting of an established cell line (MIAPACA2), three patient-derived primary samples (E52Y90 and J29M573, obtained from the NCI, and XWR200, derived at UCLA) and three KP (*LSL-Kras$^{G12D/+}$;LSL-Trp53$^{R172H/+}$;Pdx-1- Cre)* murine lines redirected genetically to express KRAS G12C instead of G12D. (**B**) Mutational profile of 11 PDAC KRAS G12C patient samples (TCGA, cBioPortal) and our human models. (**C**) Growth of the UCLA derived KRAS G12C XWR200 PDX model 25 days post-tumor challenge (*left*, mean ± SD, n = 4) and [^{18}F]FDG PET/CT scans at day 33 (*right*). (**D**) Generation of C57BL/6 syngeneic KP4662 cells that harbor G12C mutant KRAS (KP4662-G12C). (**E**) ARS-1620 selectively inhibits the proliferation of KP4662-G12C cells engineered to express KRAS G12C in anchorage-independent cultures (mean ± SD, n = 3, 72 hrs Cell-Titer-Glo assay).

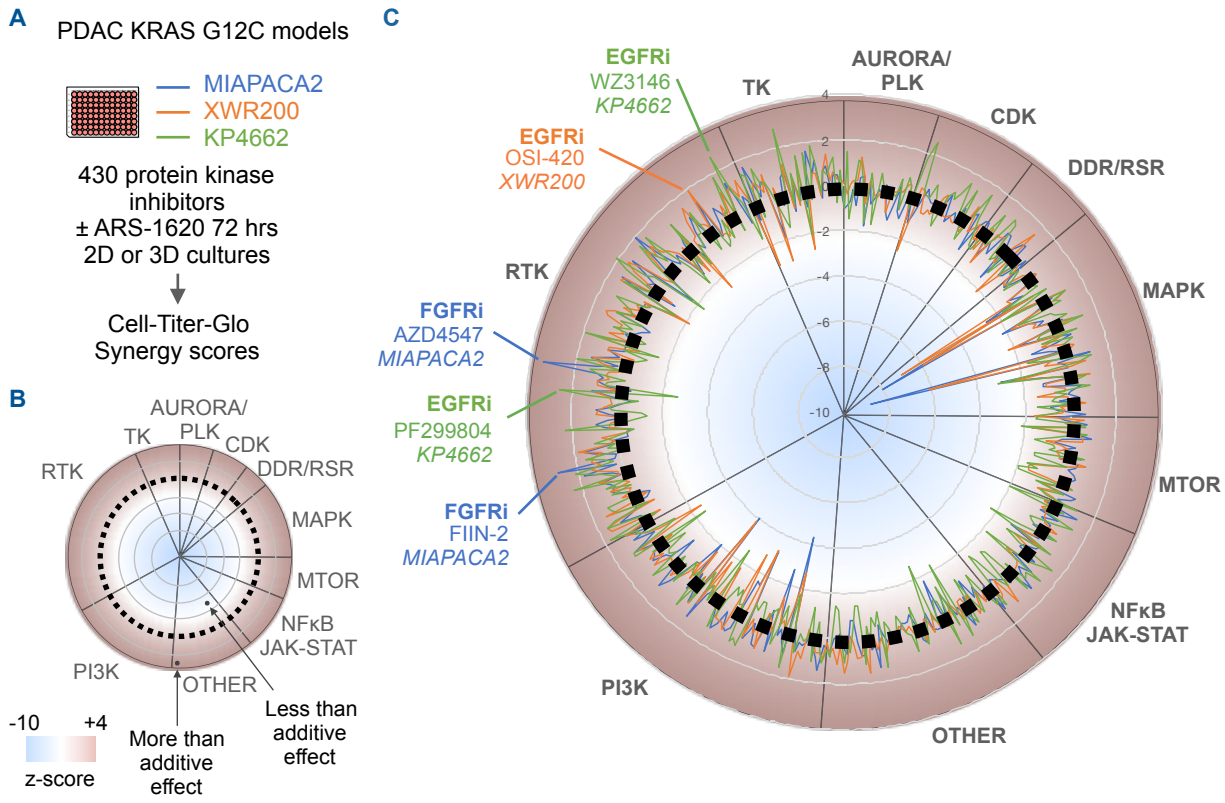
A
PDAC KRAS G12C models
MIAPACA2
XWR200
KP4662
430 protein kinase inhibitors
± ARS-1620 72 hrs
2D or 3D cultures
Cell-Titer-Glo
Synergy scores
B
AURORA/ PLK
TK
CDK
DDR/RSR
MAPK
MTOR
NFκB JAK-STAT
OTHER
PI3K
RTK
-10
+4
z-score
More than additive effect
Less than additive effect
C
EGFRi WZ3146 KP4662
EGFRi OSI-420 XWR200
FGFRi AZD4547 MIAPACA2
EGFRi PF299804 KP4662
FGFRi FIIN-2 MIAPACA2
AURORA/ PLK
TK
CDK
DDR/RSR
MAPK
MTOR
NFκB JAK-STAT
OTHER
PI3K
RTK
4
2
-2
-4
-6
-8
-10

Fig. 3.2. Identification of adaptive resistance mechanisms to direct inhibition of mutant KRAS. (**A**) Flow chart of the high throughput chemical genomics screen to identify synthetic lethal interactions with ARS-1620 in KRAS G12C MIAPACA2 cells. Dose titration of cells cultured in media containing vehicle or 1 μM ARS-1620 with 430 protein kinase inhibitors for 72 (MIAPACA2 and KP4662-G12C) or 120 (XWR200) hours in anchorage-dependent (MIAPACA2) or anchorage-independent (XWR200 and KP4662-G12C) cultures. Synergy scores for library compounds were calculated as the sum of Bliss additivity scores in combination with ARS-1620 across a 7-point concentration range. (**B**) Radar plot to display synergy or antagonism between kinase inhibitors and ARS-1620. Kinases in the library are grouped based on the type of target and Z-score is calculated from the synergy score for each inhibitor. Black-dotted circle indicates a completely additive effect. When a kinase inhibitor exhibit more than additive effect, the z-score will be plotted outside the black-dotted circle while it will be plotted inside the circle when less than additive effect is observed. (**C**) The radar that shows a synergistic inhibition of KRAS G12C PDAC cell proliferation between AZD-1620 and inhibitors of FGFR (MIAPACA2) and EGFR (XWR200 and KP4662-G12C).

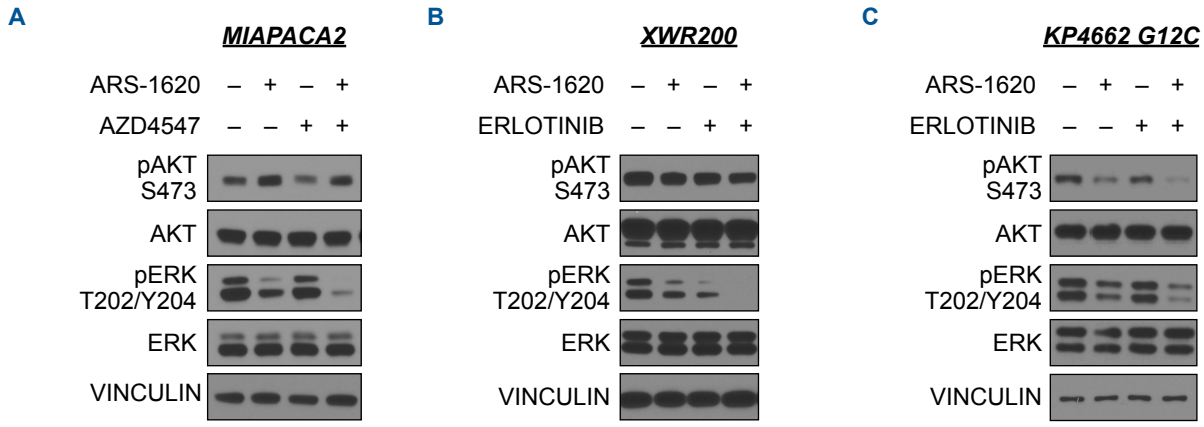

Fig. 3.3. Downregulation of oncogenic KRAS signaling pathway by combination of ARS-1620 and growth factor receptor inhibitors in KRAS G12C PDAC models. Synergistic inhibition of MAPK pathway activity as indicated by phosphorylation of ERK in MIAPACA2 (**A**), XWR200 (**B**) and KP4662-G12C (**C**) following 24 hours of treatment with 1 μM ARS-1620 and 1 μM AZD4547 (MIAPACA2) or 0.3 μM Erlotinib (XWR200 and KP4662-G12C) in anchorage-independent cultures.

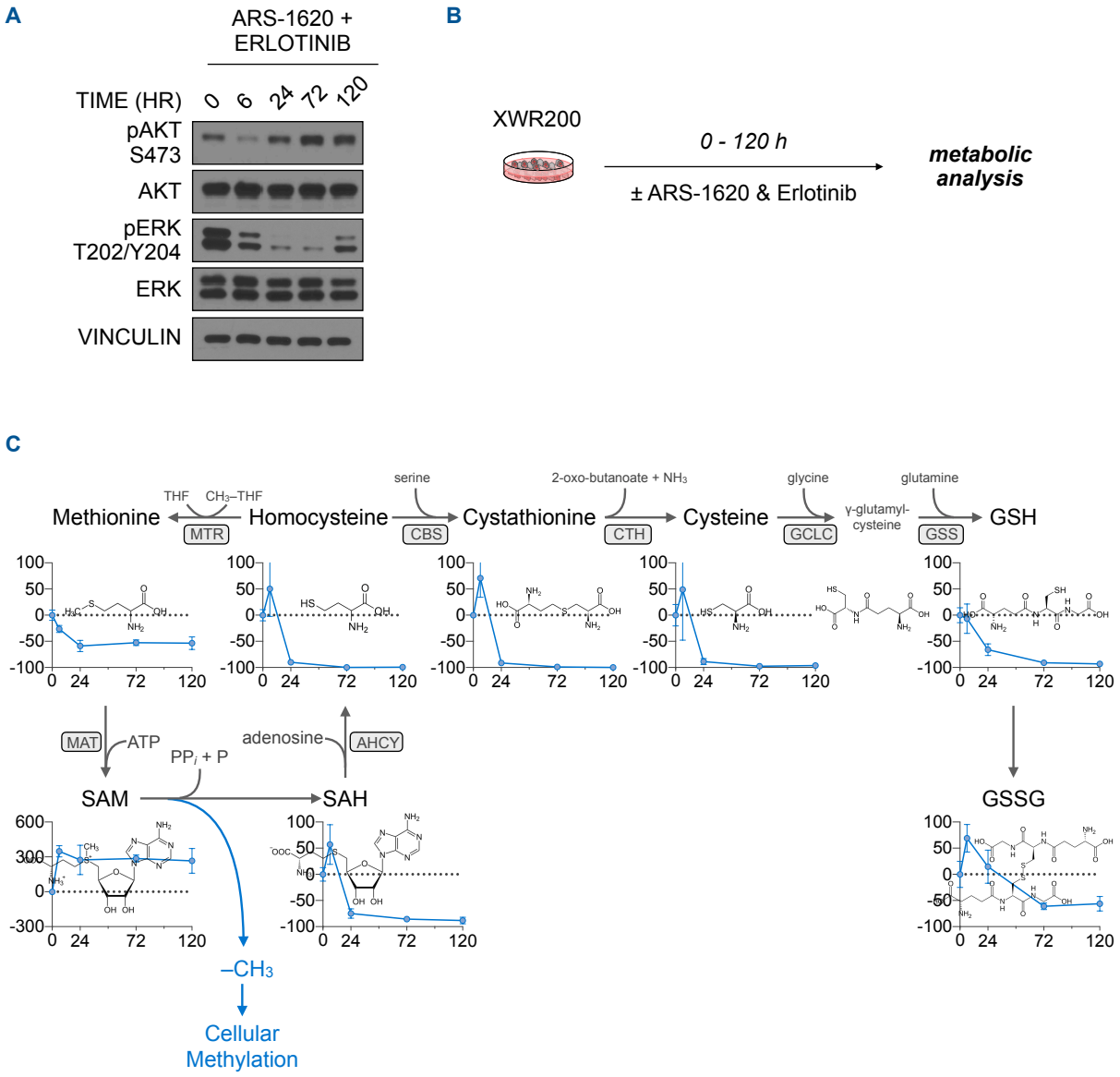
A
ARS-1620 + ERLOTINIB
TIME (HR) 0 6 24 72 120
pAKT S473
AKT
pERK T202/Y204
ERK
VINCULIN
B
XWR200
0 - 120 h
± ARS-1620 & Erlotinib
metabolic analysis
C
Methionine
THF
CH3–THF
MTR
Homocysteine
serine
CBS
Cystathionine
2-oxo-butanoate + NH3
CTH
Cysteine
glycine
GCLC
γ-glutamyl-cysteine
glutamine
GSS
GSH
MAT
ATP
PPi + P
adenosine
AHCY
SAM
SAH
GSSG
–CH3
Cellular Methylation

Fig. 3.4. Dynamic alterations in metabolism induced by inhibiting mutant KRAS and EGFR in XWR200 cells. (**A**) Immunoblot analysis probing the activity of PI3K (pAKT at S472 and total AKT), MAPK (pERK at T202/Y204 and total ERK) and DNA damage response (pH2AX at S139) pathways following 0 to 120 hours of treatment with 1 μM ARS-1620 and 0.3 μM Erlotinib in anchorage-independent cultures of XWR200 cells. Schematic representation to incorporate metabolic and signaling alterations induced by mutant KRAS-targeted therapy. (**B**) Experimental workflow to integrate LC-MS metabolomics. Cells were exposed to 1 μM ARS-1620 and 0.3 μM Erlotinib for 0 to 120 hours before sample collection for metabolomic and analysis by LC-MS. (**C**) A biochemical map of GSH biosynthesis pathway with the levels of intermediate metabolites following 0 to 120 hours of treatment with 1 μM ARS-1620 and 0.3 μM Erlotinib in XWR200 cells (n = 6).

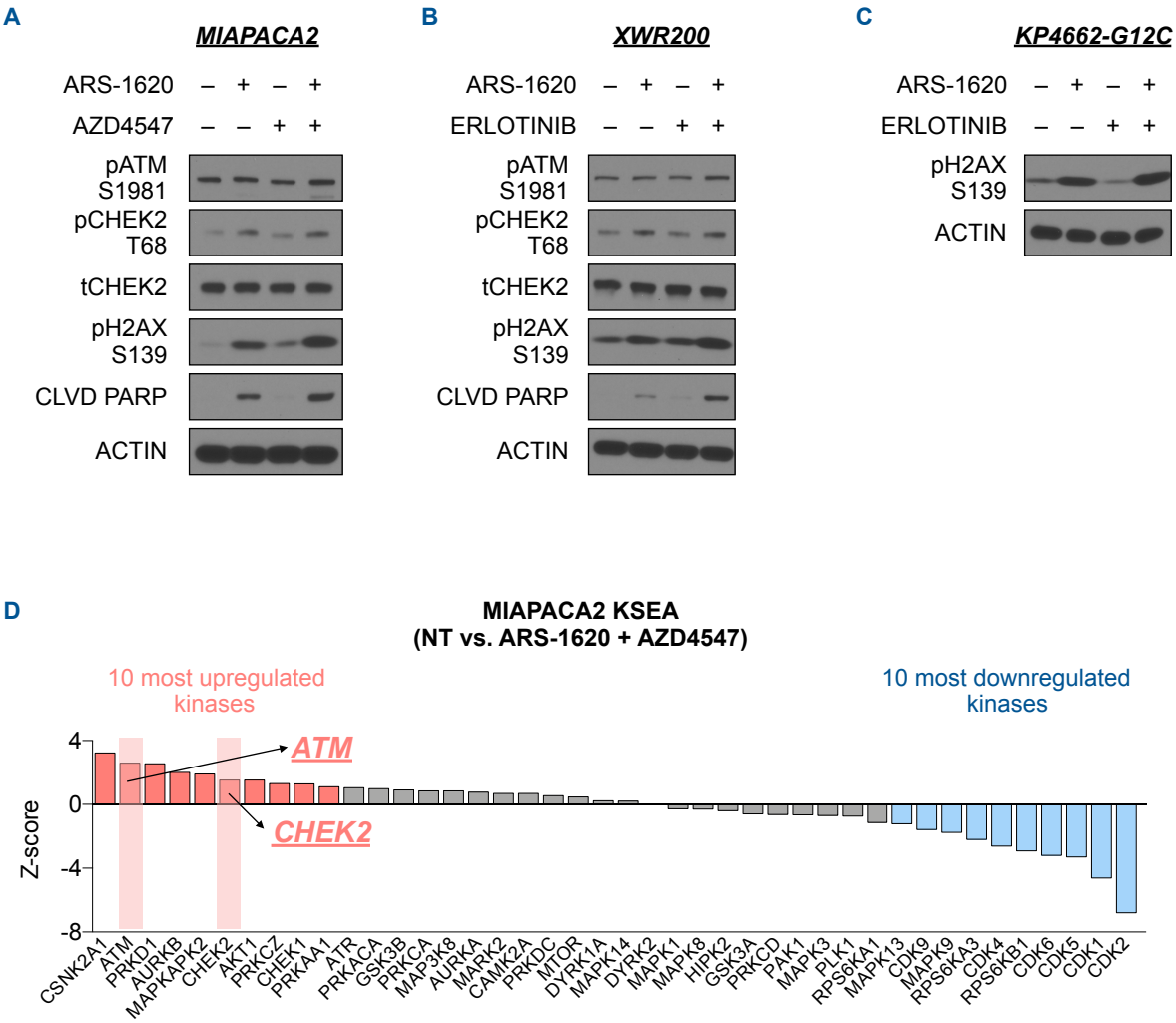
A
MIAPACA2
ARS-1620 – + – +
AZD4547 – – + +
pATM S1981
pCHEK2 T68
tCHEK2
pH2AX S139
CLVD PARP
ACTIN
B
XWR200
ARS-1620 – + – +
ERLOTINIB – – + +
pATM S1981
pCHEK2 T68
tCHEK2
pH2AX S139
CLVD PARP
ACTIN
C
KP4662-G12C
ARS-1620 – + – +
ERLOTINIB – – + +
pH2AX S139
ACTIN

D
MIAPACA2 KSEA
(NT vs. ARS-1620 + AZD4547)
10 most upregulated kinases
10 most downregulated kinases
ATM
CHEK2
Z-score
4
0
-4
-8
CSNK2A1 ATM PRKD1 AURKB MAPKAPK2 CHEK2 AKT1 PRKCZ CHEK1 PRKAA1 ATR PRKACA GSK3B PRKCA MAP3K8 AURKA MARK2 CAMK2A PRKDC MTOR DYRK1A MAPK14 DYRK2 MAPK1 MAPK8 HIPK2 GSK3A PRKCD PAK1 MAPK3 PLK1 RPS6KA1 MAPK13 CDK9 MAPK9 RPS6KA3 CDK4 RPS6KB1 CDK6 CDK5 CDK1 CDK2

Fig. 3.5. DNA damage response pathway is activated following combined inhibition of KRAS G12C and the adaptive resistance mechanism. (**A-C**) Immunoblot analysis probing the activity of DNA damage response pathway activity, as indicated by phosphorylation of ATM at S1981, CHEK2 at T68 and H2AX at S139 following 24 hours of treatment with 1 μM ARS-1620 and 1 μM AZD4547 in MIAPACA2 cells (**A**), 1 μM ARS-1620 and 0.3 μM Erlotinib in XWR200 cells (**B**) and KP4662-G12C cells (**C**). (**D**) Kinases exhibiting significantly alternated activity were identified by performing Kinase Substrate Enrichment Analysis (KSEA) on mutant KRAS targeted combination-altered phosphopeptides in MIAPACA2 cells treated with 1 μM ARS-1620 and 1 μM AZD4547 for 24 hours.

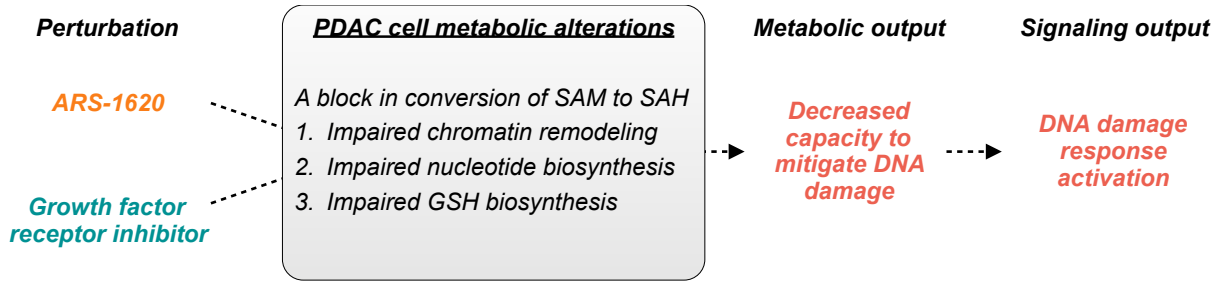

Fig. 3.6. A model summarizing metabolic and signaling alterations induced by mutant KRAS-targeted combination therapy.

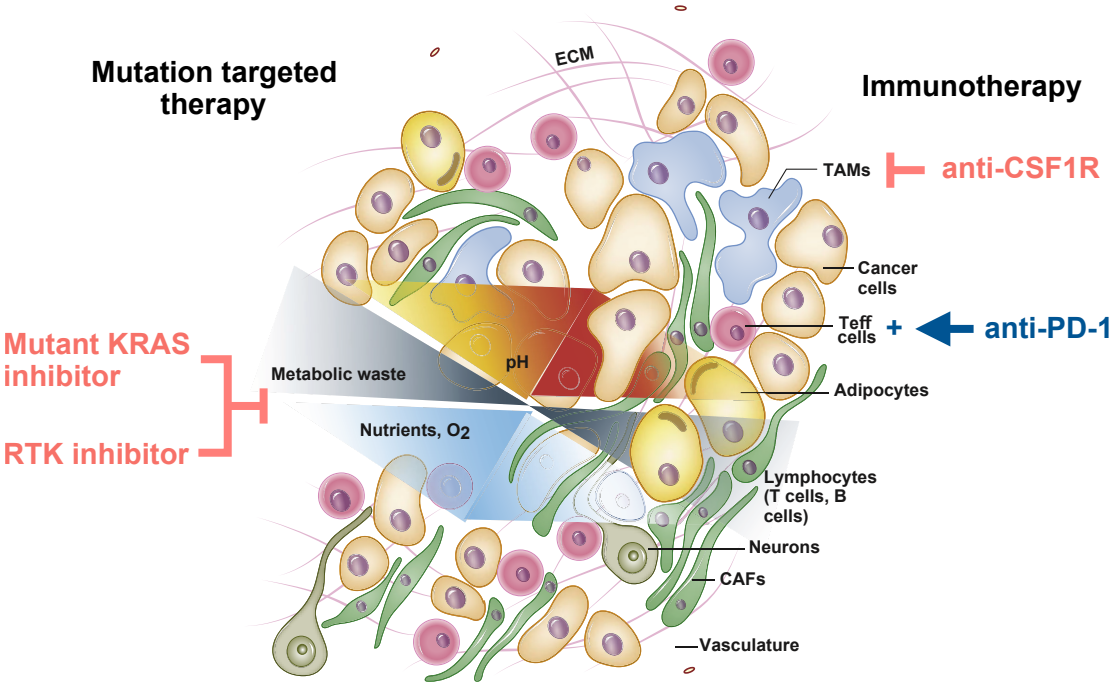

Fig. 3.7. Combination of KRAS mutation targeted therapy and immunotherapy in pancreatic cancers (Modified from Trends Cell Biol. 2017 Nov;27(11):863-875).

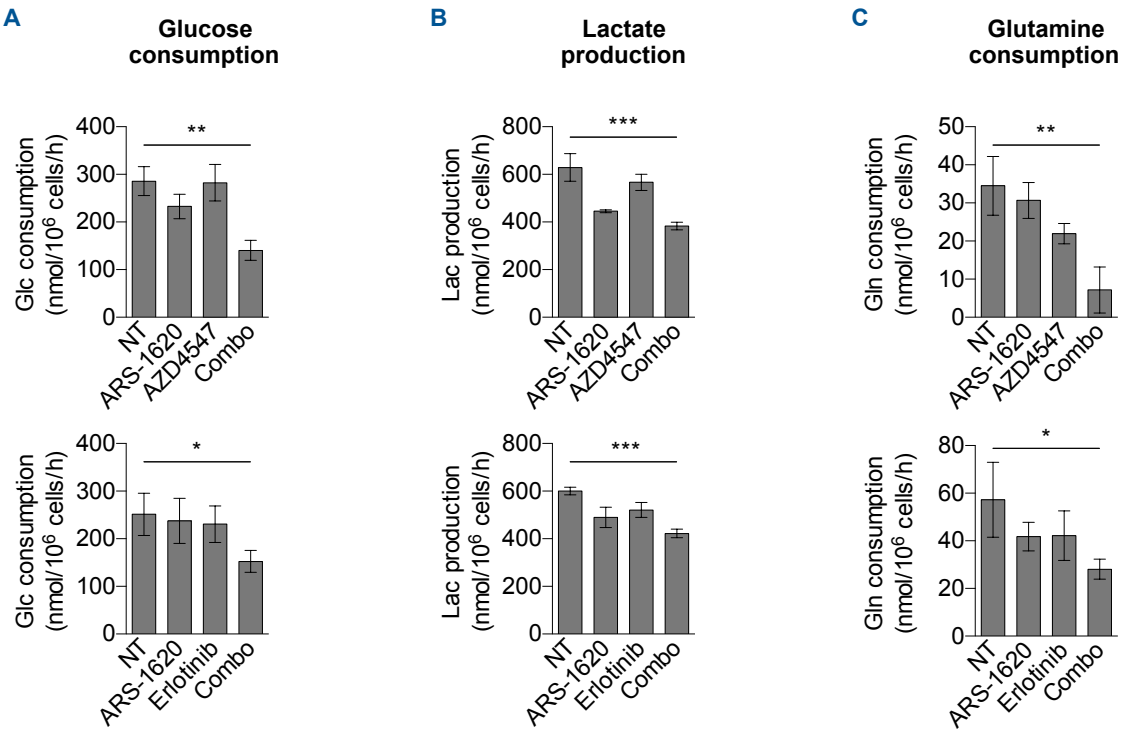

Fig. 3.8. Effects of KRAS mutation targeted therapy on the consumption and production of key metabolites. Rate of glucose consumption (**A**), lactate production (**B**) and glutamine consumption (**C**) in MIAPACA2 (upper panels) and XWR200 (bottom panels) (mean ± SD, n = 3, one-way ANOVA corrected for multiple comparisons by Bonferroni adjustment, *P < 0.05; **P < 0.01; ***P < 0.001).

REFERENCES

1. Le N, Sund M, Vinci A, GEMS CGOP (2016) Prognostic and predictive markers in pancreatic adenocarcinoma. *Dig Liver Dis* 48(3):223–230.
2. Rahib L *et al.* (2014) Projecting cancer incidence and deaths to 2030: the unexpected burden of thyroid, liver, and pancreas cancers in the United States. *Cancer Res* 74(11): 2913–2921.
3. Cancer GARNEAA, Cancer GARN (2017) Integrated Genomic Characterization of Pancreatic Ductal Adenocarcinoma. *Cancer Cell* 32(2):185–203.e13.
4. Papke B, Der CJ (2017) Drugging RAS: Know the enemy. *Science* 355(6330):1158–1163.
5. Iacobuzio-Donahue CA, Velculescu VE, Wolfgang CL, Hruban RH (2012) Genetic basis of pancreas cancer development and progression: insights from whole-exome and whole-genome sequencing. *Clin Cancer Res* 18(16):4257–4265.
6. Donahue TR, Dawson DW (2016) Leveraging Mechanisms Governing Pancreatic Tumorigenesis To Reduce Pancreatic Cancer Mortality. *Trends Endocrinol Metab* 27(11): 770–781.
7. Cox AD, Fesik SW, Kimmelman AC, Luo J, Der CJ (2014) Drugging the undruggable RAS: Mission possible. *Nat Rev Drug Discov* 13(11):828–851.
8. Janes MR *et al.* (2018) Targeting KRAS Mutant Cancers with a Covalent G12C-Specific Inhibitor. *Cell* 172(3):578–589.e17.
9. Lito P, Solomon M, Li LS, Hansen R, Rosen N (2016) Allele-specific inhibitors inactivate mutant KRAS G12C by a trapping mechanism. *Science* 351(6273):604–608.
10. Eser S, Schnieke A, Schneider G, Saur D (2014) Oncogenic KRAS signalling in pancreatic cancer. *Br J Cancer* 111(5):817–822.
11. di Magliano MP, Logsdon CD (2013) Roles for KRAS in pancreatic tumor development and progression. *Gastroenterology* 144(6):1220–1229.
12. Bardeesy N, DePinho RA (2002) Pancreatic cancer biology and genetics. *Nat Rev Cancer* 2(12):897–909.

13. Kimmelman AC, White E (2017) Autophagy and Tumor Metabolism. *Cell Metab* 25(5): 1037–1043.
14. Hunter JC *et al.* (2015) Biochemical and Structural Analysis of Common Cancer-Associated KRAS Mutations. *Mol Cancer Res* 13(9):1325–1335.
15. Pylayeva-Gupta Y, Grabocka E, Bar-Sagi D (2011) RAS oncogenes: weaving a tumorigenic web. *Nat Rev Cancer* 11:761–774.
16. Tape CJ *et al.* (2016) Oncogenic KRAS Regulates Tumor Cell Signaling via Stromal Reciprocation. *Cell* 165(4):910–920.
17. Lyssiotis CA, Kimmelman AC (2017) Metabolic Interactions in the Tumor Microenvironment. *Trends Cell Biol* 27(11):863–875.
18. Dias Carvalho P *et al.* (2018) KRAS Oncogenic Signaling Extends beyond Cancer Cells to Orchestrate the Microenvironment. *Cancer Res* 78(1):7–14.
19. Singh A *et al.* (2009) A gene expression signature associated with “K-Ras addiction” reveals regulators of EMT and tumor cell survival. *Cancer Cell* 15(6):489–500.
20. Singh A *et al.* (2012) TAK1 inhibition promotes apoptosis in KRAS-dependent colon cancers. *Cell* 148(4):639–650.
21. Bryant KL, Mancias JD, Kimmelman AC, Der CJ (2014) KRAS: feeding pancreatic cancer proliferation. *Trends Biochem Sci* 39(2):91–100.
22. Lyssiotis CA, Son J, Cantley LC, Kimmelman AC (2013) Pancreatic cancers rely on a novel glutamine metabolism pathway to maintain redox balance. *Cell Cycle* 12(13):1987–1988.
23. Simanshu DK, Nissley DV, McCormick F (2017) RAS Proteins and Their Regulators in Human Disease. *Cell* 170(1):17–33.
24. Ying H *et al.* (2012) Oncogenic Kras maintains pancreatic tumors through regulation of anabolic glucose metabolism. *Cell* 149(3):656–670.
25. Kim W *et al.* (2016) [18F]CFA as a clinically translatable probe for PET imaging of deoxycytidine kinase activity. *Proc Natl Acad Sci U S A* 113(15):4027–4032.

26. Xu S *et al.* (2018) A precision therapeutic strategy for hexokinase 1-null, hexokinase 2-positive cancers. *Cancer Metab* 6:7.
27. Manchado E *et al.* (2016) A combinatorial strategy for treating KRAS-mutant lung cancer. *Nature* 534(7609):647–651.
28. Lito P *et al.* (2012) Relief of profound feedback inhibition of mitogenic signaling by RAF inhibitors attenuates their activity in BRAFV600E melanomas. *Cancer Cell* 22(5):668–682.
29. Daemen A *et al.* (2015) Metabolite profiling stratifies pancreatic ductal adenocarcinomas into subtypes with distinct sensitivities to metabolic inhibitors. *Proc Natl Acad Sci U S A* 112(32):E4410–7.
30. Kitai H *et al.* (2016) Epithelial-to-Mesenchymal Transition Defines Feedback Activation of Receptor Tyrosine Kinase Signaling Induced by MEK Inhibition in KRAS-Mutant Lung Cancer. *Cancer Discov* 6(7):754–769.
31. Patricelli MP *et al.* (2016) Selective Inhibition of Oncogenic KRAS Output with Small Molecules Targeting the Inactive State. *Cancer Discov* 6(3):316–329.
32. Hobbs GA, Wittinghofer A, Der CJ (2016) Selective Targeting of the KRAS G12C Mutant: Kicking KRAS When It's Down. *Cancer Cell* 29(3):251–253.
33. Turgeon MO, Perry NJS, Poulogiannis G (2018) DNA Damage, Repair, and Cancer Metabolism. *Front Oncol* 8:15.
34. Newman AC, Maddocks ODK (2017) One-carbon metabolism in cancer. *Br J Cancer* 116(12):1499–1504.
35. Neesse A *et al.* (2011) Stromal biology and therapy in pancreatic cancer. *Gut* 60(6):861–868.
36. Waghray M, Yalamanchili M, di Magliano MP, Simeone DM (2013) Deciphering the role of stroma in pancreatic cancer. *Curr Opin Gastroenterol* 29(5):537–543.
37. Gupta S, Roy A, Dwarakanath BS (2017) Metabolic Cooperation and Competition in the Tumor Microenvironment: Implications for Therapy. *Front Oncol* 7:68.

38. Morandi A, Giannoni E, Chiarugi P (2016) Nutrient Exploitation within the Tumor-Stroma Metabolic Crosstalk. *Trends Cancer* 2(12):736–746.

39. Wang W *et al.* (2018) RIP1 Kinase Drives Macrophage-Mediated Adaptive Immune Tolerance in Pancreatic Cancer. *Cancer Cell* 34(5):757–774.e7.

CHAPTER 4

Ongoing study: To determine the metabolic and phenotypic consequences of reprogramming pyrimidine nucleotide biosynthesis in PDAC

Pyrimidine nucleotide metabolism in cancers

Pyrimidine nucleotides play critical roles in major biological processes including nucleic acid synthesis, phospholipid biosynthesis and protein glycosylation(1). Pyrimidine nucleotide metabolism is a highly complex and regulated system with multiple pathways contributing to its plasticity and robustness. Pyrimidine nucleotides are produced via the *de novo* pathway (DNP), which utilizes glucose, aspartic acid and glutamine as building blocks(2), and through a nucleoside scavenging pathway (NSP) in which preformed extracellular pyrimidines are translocated across the plasma membrane and then phosphorylated by uridine cytidine kinases (UCKs)(3) (**Fig. 4.1**).

The *de novo* pathway (DNP) converts glucose, aspartic acid and glutamine into UMP, the common precursor of uridine and cytidine nucleotides(2) (**Fig. 4.1**). The first three steps of the DNP are catalyzed in the cytosol by the trifunctional enzyme carbamoyl-phosphate synthetase 2, aspartate transcarbamylase, and dihydroorotase (CAD) (**Fig. 4.1**). The fourth step, carried out by dihydroorotate dehydrogenase (DHODH), which is located on the outer surface of the inner mitochondrial membrane, involves ubiquinone-mediated oxidation of dihydroorotate to orotate, which in parallel contributes electrons to the mitochondrial electron transport chain (ETC)(2) (**Fig. 4.1**). Uridine monophosphate synthase (UMPS) catalyzes the final two steps of the DNP to generate UMP in the cytosol. Further integrating pyrimidine metabolism with the ETC, the DNP substrate aspartate is limited in cells with constitutive or therapy-induced defects in the ETC(4).

The dependence on pyrimidine nucleotide biosynthesis is commonly increased in cancers due to increased metabolic demands, caused by the activation of oncogenes(5–9). Among multiple players involved in pyrimidine nucleotide biosynthesis, the mitochondrial ETC complex 1 and

the essential DNP enzyme DHODH are two major points of pharmacological modulation and can be targeted for the treatment of multiple cancers, including PDAC(4, 9–17).

Mitochondrial ETC complex 1 is the major source of aspartate biosynthesis that supports *de novo* nucleotide biosynthesis

In these recent studies on ETC complex 1 inhibition in cancers, the role of the complex was shown to go beyond the transport of electrons to CoQ(4, 10). Instead, the anti-tumor effects of ETC complex 1 inhibitors were attributed to its role in aspartate biosynthesis(11, 12). A decrease in aspartate biosynthesis, induced by ETC complex 1 inhibition, in turn causes limitation in *de novo* biosynthesis of nucleotides(11, 12). Further supporting this, the growth-inhibitory effects of ETC complex 1 inhibitors were rescued by supplementing media with nucleosides(11, 12).

ETC1-independent ways of generating aspartate

However, such a model cannot be generalized since there are other biological processes by which aspartate can be supplied in PDAC cells. Such processes include recycling and scavenging of nutrients through lysosome-dependent autophagy and macropinocytosis, well-documented features of PDAC cells(18). In addition, scavenging of extracellular aspartate provides another way to supply PDAC cells with this critical amino acid(12).

Aspartate-independent ways of generating pyrimidine nucleotides

Adding to the complexity of aspartate biology in PDAC is the presence of aspartate-independent pathway for supply of pyrimidine nucleotides, the aforementioned nucleoside scavenging pathway (NSP), which is mediated by uridine cytidine kinase (UCK) isoenzymes(3, 19) (**Fig. 4.1**). Taken together, it is not only the flux through mitochondrial ETC complex 1 that determines the availability of aspartate and nucleotides in PDAC cells.

Additional metabolic fates of aspartate

In addition to nucleotide biosynthesis, aspartate can be shunted to the urea cycle (**Fig. 4.1**). The enzyme that mediates this entry is argininosuccinate synthase 1 (ASS1). Interestingly, this enzyme is downregulated in some cancers, which leads to an increased flux of aspartate towards *de novo* pyrimidine nucleotide biosynthesis(20). However, PDAC cells express high levels of ASS1 (http://gepia.cancer-pku.cn/), indicating that ASS1-mediated aspartate shunting to the urea cycle is active. A major function of the urea cycle is the disposal of nitrogen by converting it to urea by arginase(21), a process that is shown to be involved in PDAC(22). It is possible that the urea cycle, and thus arginase, is used for the disposal of aspartate when a surplus amount of the amino acid is present. However, it is unknown whether such conversion of aspartate is occurring, and what the metabolic consequences of such a conversion would be in PDAC.

Aspartate metabolism and pyrimidine nucleotide metabolism: Bi-directional crosstalk?

Collectively, the data from literature reveal gap in knowledge and raise several related questions.

Q1: Is pyrimidine nucleotide insufficiency the main mechanism by which inhibition of mitochondrial ETC Complex I limits the growth of PDAC cells?

Q2: What are the metabolic differences and similarities between inhibiting *de novo* pyrimidine biosynthesis by limiting aspartate availability versus inhibiting DHODH, a rate-limiting enzyme in *de novo* pyrimidine biosynthesis?

Q3: Related to Q2, how does inhibition of *de novo* pyrimidine biosynthesis impact aspartate utilization in PDAC cells?

If the answer to Q1 is yes, as suggested by recent reports(11, 12), growth inhibition induced by ETC complex I inhibitors across a panel of PDAC models should correlate with growth inhibition induced by a direct inhibitor of *de novo* pyrimidine biosynthesis at the level of DHODH.

Therefore, Q1 can be answered by comparing the inhibitory effects of Piericidin (a specific Complex I inhibitor)(23) with those of NITD-982 (a specific DHODH inhibitor)(24).

However, if there are bidirectional crosswalks between aspartate and pyrimidine nucleotide metabolism, PDAC cells may respond differently to the two perturbations, which would result in the identification of a hitherto unidentified non-canonical function of pyrimidine DNP. In this case, Q2 and Q3 can be answered by profiling global metabolic changes induced by Complex I inhibition *vs*. DHODH inhibition.

In this context, we measured if PDAC cells respond similarly to the inhibition of mitochondrial ETC complex 1 and DHODH. Briefly a panel of 33 PDAC models were treated with 12 point titration of NITD-982 (a DHODH inhibitor) and Piericidin (an ETC complex 1 inhibitor). The dose-response curves were generated from each of the models (**Fig 4.2B and C**). Our data indicate that the greatest level of variation is observed across the panel following treatment with 1 μM NITD-982 treatment (**Fig 4.2B**) and 10 nM Piericidin (**Fig 4.2C**). To enable the comparison of multiple models with varying proliferation rate, we have calculated normalized proliferation rate (PR) values, which corrects the varying rates of proliferation (25), in the cells treated with 10 nM Piericidin or 1 μM NITD-982. Interestingly, our data show that there's no significant correlation between the sensitivity to the inhibition of ETC complex 1 and DHODH, suggesting the presence of bi-directional crosstalk between aspartate metabolism and pyrimidine nucleotide metabolism (**Fig 4.2D**).

Ongoing studies

To answer Q2 and Q3, we are profiling global metabolic changes induced by the inhibition of ETC1 and DHODH. Our preliminary findings indeed indicate that the pyrimidine nucleotide metabolism is a determinant of the fate of aspartate. In detail, our data demonstrate that a significant proportion of aspartate is utilized for *de novo* pyrimidine biosynthesis, and that

inhibition of pyrimidine DNP by small molecule inhibitors of DHODH results in the re-routing of aspartate towards the ASS1-argininosuccinate shunt which eventually leads to generation of nitric oxide by endothelial nitric oxide synthase. From these findings, we are further testing the hypothesis that a bidirectional crosstalk between aspartate and pyrimidine nucleotide biosynthetic pathways and may reveal actionable metabolic alterations.

MATERIALS AND METHODS

Measurement of cell viability

Cells were cultured as described in the Results section. Following various perturbations, cell viability was measured by Cell-Titer-Glo (Promega) following manufacturer's protocol using Flex Station II (Molecular Devices) or Synergy H1 (BioTek) plate reader.

Profiling sensitivity of PDAC models to NITD-982 and Piericidin

To profile sensitivity of various PDAC models to the inhibition of DHODH or ETC complex 1, each model was treated with twelve-dose titration of NITD-982 (31.6 pM - 10 μM). Cell viability was measured by Cell-Titer-Glo (Promega) following manufacturer's protocol before and after the treatment. To enable the comparison of sensitivity of multiple models with varying doubling time, one concentration, which exhibits greatest variation in the responses across the PDAC models, was selected for the calculation of PR values, which correct for the confounders across the models, were calculated as previously described{27135972}.

FIGURES

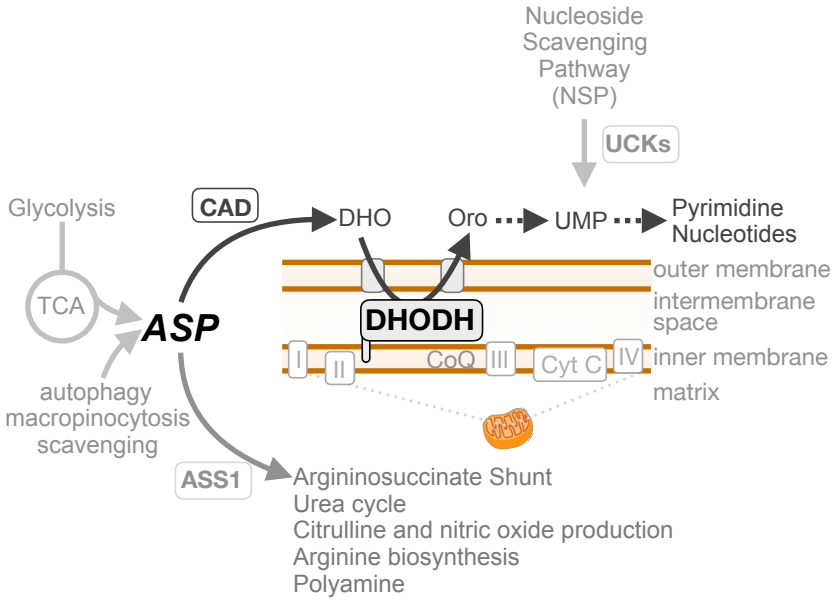

Fig. 4.1. Schematic representation of aspartate metabolism and pyrimidine nucleotide metabolism. CAD, carbamoyl-phosphate synthetase 2, aspartate transcarbamylase, and dihydroorotase; DHO, dihydroorotate; Oro, orotate; UMP, uridine monophosphate; UCK, uridine-cytidine kinase; DHODH, dihydroorotate dehydrogenase; ASP, aspartate; I - IV, ETC complex I - IV; Cyt C, cytochrome C; ASS1, argininosuccinate synthase.

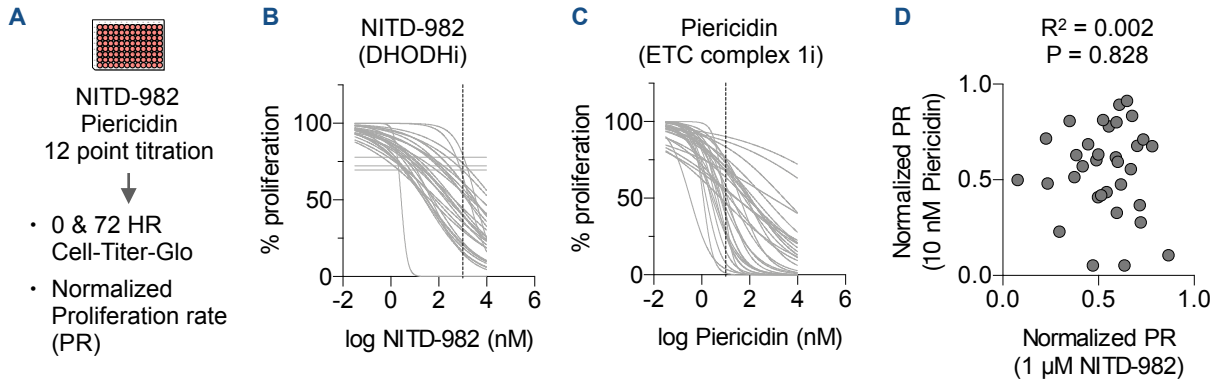

Fig. 4.2. Sensitivity of a panel of PDAC models to the inhibition of mitochondrial ETC complex 1 and DHODH. (**A**) Experimental workflow to measure the sensitivity of various PDAC models to the inhibition of dihydroorotate dehydrogenase (DHODH) by NITD-982 or mitochondrial electron transport chain (ETC) complex 1 by Piericidin. Cells were treated with 12 dose-titration (31.6 pM to 10 µM) of NITD-982 and Piericidin. cultured in media containing vehicle or 1 µM ARS-1620 with 430 protein kinase inhibitors for 72 hours. Cell proliferation was calculated by running Cell-Titer-Glo assay at 0 and 72 hours of treatment. (**B and C**) Dose-response curve of PDAC models to NITD-982 (**B**) and Piericidin (**C**). To enable the comparison of sensitivity of multiple models with varying doubling time, 1 µM NITD-982 and 10 nM Piericidin (dotted line), which exhibits greatest variation in the responses across the PDAC models, were selected for the calculation of PR values that correct for the confounders across the models. (**D**) Correlation between the normalized proliferation rates (PR) in response to 1 µM NITD-982 (x-axis) and 10 nM Piericidin (y-axis) across a panel of PDAC models.

REFERENCES

1. Lane AN, Fan TW (2015) Regulation of mammalian nucleotide metabolism and biosynthesis. *Nucleic Acids Res* 43(4):2466–2485.
2. Jones ME (1980) Pyrimidine nucleotide biosynthesis in animals: genes, enzymes, and regulation of UMP biosynthesis. *Annu Rev Biochem* 49:253–279.
3. Van Rompay AR, Norda A, Lindén K, Johansson M, Karlsson A (2001) Phosphorylation of uridine and cytidine nucleoside analogs by two human uridine-cytidine kinases. *Mol Pharmacol* 59(5):1181–1186.
4. Birsoy K *et al.* (2015) An Essential Role of the Mitochondrial Electron Transport Chain in Cell Proliferation Is to Enable Aspartate Synthesis. *Cell* 162(3):540–551.
5. Mannava S *et al.* (2008) Direct role of nucleotide metabolism in C-MYC-dependent proliferation of melanoma cells. *Cell Cycle* 7(15):2392–2400.
6. Liu YC *et al.* (2008) Global regulation of nucleotide biosynthetic genes by c-Myc. *PLoS One* 3(7):e2722.
7. Cunningham JT, Moreno MV, Lodi A, Ronen SM, Ruggero D (2014) Protein and nucleotide biosynthesis are coupled by a single rate-limiting enzyme, PRPS2, to drive cancer. *Cell* 157(5):1088–1103.
8. Levine AJ, Puzio-Kuter AM (2010) The control of the metabolic switch in cancers by oncogenes and tumor suppressor genes. *Science* 330(6009):1340–1344.
9. Koundinya M *et al.* (2018) Dependence on the Pyrimidine Biosynthetic Enzyme DHODH Is a Synthetic Lethal Vulnerability in Mutant KRAS-Driven Cancers. *Cell Chem Biol* 25(6): 705–717.e11.
10. Sullivan LB *et al.* (2015) Supporting Aspartate Biosynthesis Is an Essential Function of Respiration in Proliferating Cells. *Cell* 162(3):552–563.
11. Sullivan LB *et al.* (2018) Aspartate is an endogenous metabolic limitation for tumour growth. *Nat Cell Biol* 20(7):782–788.

12. Garcia-Bermudez J *et al.* (2018) Aspartate is a limiting metabolite for cancer cell proliferation under hypoxia and in tumours. *Nat Cell Biol* 20(7):775–781.
13. White RM *et al.* (2011) DHODH modulates transcriptional elongation in the neural crest and melanoma. *Nature* 471(7339):518–522.
14. Tan JL *et al.* (2016) Stress from Nucleotide Depletion Activates the Transcriptional Regulator HEXIM1 to Suppress Melanoma. *Mol Cell* 62(1):34–46.
15. Sykes DB *et al.* (2016) Inhibition of Dihydroorotate Dehydrogenase Overcomes Differentiation Blockade in Acute Myeloid Leukemia. *Cell* 167(1):171–186.e15.
16. Brown KK, Spinelli JB, Asara JM, Toker A (2017) Adaptive Reprogramming of. *Cancer Discov* 7(4):391–399.
17. Mathur D *et al.* (2017) PTEN Regulates Glutamine Flux to Pyrimidine Synthesis and Sensitivity to Dihydroorotate Dehydrogenase Inhibition. *Cancer Discov* 7(4):380–390.
18. Guo JY *et al.* (2016) Autophagy provides metabolic substrates to maintain energy charge and nucleotide pools in Ras-driven lung cancer cells. *Genes Dev* 30(15):1704–1717.
19. Qian Y *et al.* (2014) Phosphorylation of uridine and cytidine by uridine-cytidine kinase. *J Biotechnol* 188:81–87.
20. Rabinovich S *et al.* (2015) Diversion of aspartate in ASS1-deficient tumours fosters de novo pyrimidine synthesis. *Nature* 527(7578):379–383.
21. Wu G, Morris SM (1998) Arginine metabolism: nitric oxide and beyond. *Biochem J* 336 (Pt 1):1–17.
22. Zaytouni T *et al.* (2017) Critical role for arginase 2 in obesity-associated pancreatic cancer. *Nat Commun* 8(1):242.
23. Darrouzet E, Issartel JP, Lunardi J, Dupuis A (1998) The 49-kDa subunit of NADH-ubiquinone oxidoreductase (Complex I) is involved in the binding of piericidin and rotenone, two quinone-related inhibitors. *FEBS Lett* 431(1):34–38.
24. Wang QY *et al.* (2011) Inhibition of dengue virus through suppression of host pyrimidine biosynthesis. *J Virol* 85(13):6548–6556.

25. Hafner M, Niepel M, Chung M, Sorger PK (2016) Growth rate inhibition metrics correct for confounders in measuring sensitivity to cancer drugs. *Nat Methods* 13(6):521–527.